

Flame spray pyrolysis for synthesizing functional nanoparticles: Fundamental investigations on single and double droplet combustion

Vom Fachbereich Produktionstechnik

der

UNIVERSITÄT BREMEN

zur Erlangung des Grades

Doktor-Ingenieur

genehmigte

Dissertation

von

M. Sc. Haipeng Li

Gutacht: Prof. Dr.-Ing. habil. Lutz Mädler (Universität Bremen)

Prof. Dr.-Ing. Stefan Will (Friedrich-Alexander-Universität Erlangen-Nürnberg)

Tag der mündlichen Prüfung: 12. November 2021

Berichte aus der Verfahrenstechnik

Haipeng Li

Flame spray pyrolysis for synthesizing functional nanoparticles: Fundamental investigations on single and double droplet combustion

(Dissertation: Universität Bremen)

Bremen 2021

Acknowledgements

The present work was performed during my stay as a PhD student and a researcher assistant in the Faculty of Production Engineering at the University of Bremen, and Leibniz Institute for Materials Engineering IWT, Germany.

First and foremost, I would like to express my highest gratitude and appreciation to my supervisor, Prof. Dr.-Ing. habil. Lutz Mädler, for his excellent mentoring, kind help and continuous encouragement during my PhD study. Prof. Mädler gave me a fast and positive response, when I expressed my desire to do my PhD in his excellent research group in August, 2013. I am very grateful to him for offering me this precious opportunity. During my PhD study, Prof. Mädler has kindly provided me supportive environments, advanced platforms and freedom to do excellent research work. He offered me timely and effective help when I was in trouble, enabling my research process to run smoothly and successfully. He generously provided financial support on buying new setups and components, which highly helped me to obtain better experimental results and more scientific achievements. I could always gain perfect ideas and effective solutions from the fruitful discussions and communications with him. With the excellent supervision of Prof. Mädler, I have developed my independent research ability, highly improved myself and obtained many outstanding scientific achievements during my PhD study. I am very lucky to have such a great scientist and a research genius as my PhD supervisor. His attitude and enthusiasm for fantastic research and genius new ideas have made one example of an excellent scientist, which inspires me to follow his step to become a brilliant researcher in the future. In addition, Prof. Mädler has generously offered additional financial supports to me by providing a position of research assistant. Thus, I could afford to invite my son to stay with me in Germany. Finally, I am also really appreciated and grateful for his strong recommendation when I was looking for a post-doctoral position to continue my research career during the Corona crisis.

Acknowledgements

I would like to acknowledge Prof. Dr.-Ing. Stefan Will from Friedrich-Alexander-Universität Erlangen-Nürnberg for his commitment as my second reviewer.

I would like to thank the other members of the examination board: Prof. Dr.-Ing. Kurosch Rezwan, Dr. Kerstin Avila, Arne Witte, and Riham Suleiman. Special thanks to Jan Groeneveld, Thomas Varelmann, and Arne Witte for the IT support of the oral defense.

During my thesis submission and the application for admission to the colloquium, Mrs Susanne Baass from Doctoral Dissertation Committee FB4 and Dr. Sangita Swapnasrita have kindly provided me professional advises and numerous helps. I would like to give my sincere thanks to them.

I would like to acknowledge Georgios Sotiriou, Padryk Merkl, Jill Ziesmer, Felix Geissel, Jens Karlsson, Yael Suárez, Anandi Narayana Moorthy, Maria Carlson, and Genevieve Garriss from the Department of Microbiology, Tumor and Cell Biology at Karolinska Institutet for attending the rehearsal of my oral defense and for giving my valuable suggestions.

I would like to give my sincere thanks to The Swedish Migration Agency. The people working there are so nice, and they have provided me great favors to speed up the application of my work permit extension. Thus, I could get my residence permission in time to enter Germany for my PhD oral defense.

I would like to thank Dipl.-Ing Horst Woyczehowski and his family, Krishan Sandmann, Adithya Balakrishnan, Stefan Endres, Apostolos Kyrloglou, Thomas Varelmann, Jana Schneider, Jakob Stahl, Malte Stodt, and XiuRan Yin for their strong supports and warm helps.

I gratefully thank Dr.-Ing Thomas Wriedt from University of Bremen and Leibniz Institute for Materials Engineering IWT for his great favors to read my thesis. His professional comments and fantastic advices have highly improved the quality of my thesis, especially the abstract in German and the chapter on holography. Special thanks to Dr.-Ing Norbert Riefler from University of

Bremen and Leibniz Institute for Materials Engineering IWT for his generous help by proof reading of the German abstract.

Most of the experimental work have been done in single droplet laboratory and spray laboratory in the reactive spray group. First, I am especially thankful to Dr. Christopher Rosebrock who introduced me to the field of single droplet combustion. He has taught me single droplet combustion experiments using the high-speed camera recording and Rainbow Refractometry techniques. I am really grateful to him for his well training and tremendous favors to my research. Secondly, I would like to express my sincere gratitude and thanks to Dr. habil. Suman Prokhrel who introduced me to the field of nanoparticle synthesis. He provided me the precious opportunities to do flame spray pyrolysis experiments as well as helped me on XRD and TEM measurements. Dr. Suman Prokhrel has always good ideas and promotes at all times the cooperation with other researchers to do excellent work. I really admire his opening research attitude and have the luck to collaborate with such a brilliant researcher. In addition, this work would not have been completed without the great contributions from Dipl.-Ing Horst Woyczehowski, who have done so many favors to me for the experimental setup, single droplet generator, and double droplet generator. I am really appreciated that I could have such a nice and warm friend.

During my research, Dr.-Ing Thomas Wriedt and Dr.-Ing Norbert Riefler have provided me numerous kind favors and friendly help. They have transferred me their knowledge on droplet generation and optical measurements, which speeded up my research process and improved the work quality. Dr.-Ing Thomas Wriedt and Dr.-Ing Norbert Riefler also have given me good suggestions, shared valuable books and papers, and provided codes for simulation. Thus, I would like to give my sincere thanks to them.

I would like to express my sincere gratitude to Dr. Lydia Achelis for her great help and kindness during my PhD study. Dr. Lydia Achelis has taught me a lot of knowledge on daily life in Germany,

Acknowledgements

file processing, ordering new setups, preparing payment documents, and job applications. I am also very grateful to the activities (e.g., Seminarfahrt nach Hirschegg, Freimarkt and Weihnachtsmarkt) that she has organized, where I had many pleasures. In addition, Dr. Lydia Achelis' weekly Freitagsgrüße gave me tremendous moral supports and motivated me to work and live at home during the Corona crisis.

I would like to thank Claudia Sobich, Kristina Hauschild, Andrea Wachner and Mirja Kahrs in the secretary team at Leibniz Institute for Materials Engineering IWT. I am really appreciated with their invaluable assistance and kind helps in my daily life.

I would like to express my appreciation to my former colleagues, Gevork Babajan, Dr. Henrike Großmann, Dr. Valentin Baric, M.Sc. Florian Meierhofer, Dr. Sven Schopf, and current colleagues, M.Sc. Hendrik Naatz, Sangita Swapnasrita, Adithya Balakrishnan, Stefan Endres, Jakob Stahl, Thomas Varelmann, Maurice Frost, Jan Groeneveld in the reactive spray group. I am grateful to be in such a united and great group, where the members help each other.

Special thanks to Krischan Sandmann for his generous help. Mr. Sandmann has a great personality, and always provides help to people who are in trouble. It is my luck to share one office with such a nice, reliable and friendly person.

I gratefully thank the technician team at Leibniz Institute for Materials Engineering IWT. Gevork Babajan has helped me on many things, and he is a nice person and a warm friend. Thomas Varelmann has helped me a lot on flame spray pyrolysis and general issues. Rainer Lehmann has helped me on computer, gas bottle and IT issues. Stefan Evers has helped me to improve the droplet generation setup. Maurice Frost has provided me helps on chemical safety issues. Frank Peschel helped me to order new gases for single droplet combustion experiments. I would like to acknowledge their generous support, which ensure the smooth running of my research and official work.

Acknowledgements

Special thanks to my student assistant, Muhammad Shoaib Sikander, who has done so many excellent works. I also would like to thank Marco Schowalter and Thorsten Mehrtens from the Institute of Solid State Physics (University of Bremen) for providing helps with TEM measurements, Tina Kühn from Institute of Advanced Ceramics (University of Bremen) for providing helps with TGA measurements, as well as Dr. Michael Wendschuh and Dr. Johannes Birkenstock from Central Laboratory for Crystallography and Applied Materials (University of Bremen) for providing helps with XRD measurements.

Special thanks to Prof. Johannes Kiefer, who are not only one excellent scientist but also one nice and warm person. The communications and discussions with Prof. Kiefer always make me feeling like talking with an old friend. It is so nice and pleased that I could have collaborative work with him. I would like to thank Prof. Yang Zhang from the University of Sheffield, and Prof. Jun Huang from the University of Sydney. I am very grateful for the international collaboration with such great scientists. I would like to acknowledge Collins Erinmwingbovo and Prof. Fabio La Mantia from Institute of Solid State Physics, University of Bremen. The nice cooperation with them makes me acquire new knowledge on Li-Ion battery. I would like to give my sincere thanks to Dr. Yingchun Wu from Zhejiang University for his valuable helps on digital in-line holography.

I would like to acknowledge the financial support from China Scholarship Council (CSC) and German Research Foundation (DFG) within the priority program SPP 1980 SPRAYSYN. During the excellent SPP 1980 project, I have received friendly helps and a lot of valuable knowledge and experience from other excellent and genius researchers. Special thanks to Steffi Nickol for her generous helps.

Finally, I would like to give the greatest thanks to my beloved wife Ai-Cang. With her accompany and support, I could insist to finish my PhD study. Special thanks to my sweet son Dou-Dou, who brings me joy and happiness each day.

Abstract

In this thesis “Flame spray pyrolysis for synthesizing functional nanoparticles: Fundamental investigations on single and double droplet combustion”, experimental studies on droplet combustion and explosions to fundamentally understand the particle formation from liquid droplets and droplet interactions in the nanofabrication process of flame spray pyrolysis (FSP) are shown.

FSP is one promising and versatile flame aerosol technique for fast synthesis of functional and engineering nanomaterials. This gas-phase synthesis nanomaterial process is famous and attractive for its reproducibility and scalability, and thus has potential applications for commercial scale-up production in industry. Gas-to-particle conversion and droplet-to-particle conversion are two particle formation routes in FSP, which decide the quality of produced particles. The particle formation mechanism is associated with the mass transfer of the precursor from liquid droplet to gas phase. Therefore, it is necessary and important to investigate droplet combustion behavior of precursor solutions, for providing fundamental insights into the mechanisms of droplet combustion and particle formation in FSP. The focus of this work is divided into three parts.

Single droplet combustion and FSP synthesis of iron oxide nanoparticles using low- and high-volatility precursors were done, aiming to investigate the mechanism and occurrence condition of droplet micro-explosions, nanoparticle formations in single droplet combustion and FSP, as well as the promotion of homogeneous nanoparticle synthesis from low-volatility precursors. The influences of precursor choices, precursor concentrations and solvent compositions on droplet combustion behaviors, rainbow signals and the synthesis of iron oxide particles were experimentally investigated. The mechanism and occurrence conditions of droplet micro-explosions were discussed and summarized, which could be used to trigger explosions of droplets containing metal nitrates. The synthesized particles were characterized using Brunauer-Emmett-Teller (BET), X-ray diffraction (XRD), as well as low- and high-resolution transmission electron microscopy (TEM and HRTEM) techniques. The similarity of nanoparticles prepared from single

droplet combustion and FSP was explained. It is found that the secondary-atomization of droplets induced by micro-explosions efficiently promotes the production of homogeneous nanoparticles.

Three-dimensional measurements of double droplet combustion of the pure solvent and the precursor solution were conducted, targeting to study the influence of a neighboring droplet on combustion behaviors (droplet interactions), and the occurrence of double droplet explosions. The developed three-dimensional measurement technique using two highly time-synchronized high-speed cameras could provide highly time-resolved information including droplet diameters, flame diameters, droplet 3D trajectories, droplet 3D velocities, and the center distances between the two burning droplets. Droplet interactions in the pure oxygen atmosphere as well as in the mixture of oxygen and nitrogen atmosphere were investigated. Droplet micro-explosions were first observed during double droplet combustion experiments of precursor solutions. The occurrence of double droplet explosions is affected by droplet interactions.

Digital in-line holography measurements of single droplet combustion were performed, and the focus is to detect the size of non-burning droplets and to estimate the refractive index gradient surrounding the burning droplet. The constructed experimental setup and the developed imaging processing method are able to obtain clear hologram signals. The developed methods for hologram formation and numerical reconstruction have shown their abilities to detect droplet size. The influence of the surrounding flame on hologram signals are experimentally identified, which is proposed to estimate the refractive index gradient surrounding burning droplets.

This thesis shows the capability of using droplet combustion experiments to provide fundamental information of droplet combustion, explosion and interaction for FSP. These investigations could be used to explore low-cost precursor-solvent systems for producing homogeneous nanoparticles, to figure out the interaction between burning droplets, as well as to understand the droplet flame.

Zusammenfassung

In dieser Arbeit „Flame spray pyrolysis for synthesizing functional nanoparticles: Fundamental investigations on single and double droplet combustion“ werden die experimentellen Untersuchungen zur Tropfenverbrennung und -explosionen zum grundlegenden Verständnis der Partikelbildung aus brennenden Flüssigkeitstropfen samt der Tropfenwechselwirkungen in der Flammensprühyrolyse (FSP) dargestellt.

Flammensprühyrolyse ist eine vielversprechende und vielseitige Flammen-Aerosol-Technik für die schnelle Synthese von funktionalen Nanomaterialien. Dieses Gasphasensyntheseverfahren für Nanomaterialien ist besonders attraktiv wegen seiner Reproduzierbarkeit und Skalierbarkeit und bietet daher großes Anwendungspotential für die kommerzielle Produktion in der Industrie. Gas-zu-Partikel-Umwandlung und Tröpfchen-zu-Partikel-Umwandlung sind zwei Partikelbildungswege in der FSP, die über die Qualität der produzierten Partikeln entscheiden. Der Mechanismus der Partikelbildung ist mit dem Massentransfer des Precursors von der flüssigen Tröpfchen- in die Gasphase verbunden. Daher ist es notwendig und wichtig, das Tropfenverbrennungsverhalten von Precursorlösungen zu untersuchen, um grundlegende Einblicke in die Mechanismen der Tropfenverbrennung und Partikelbildung in der FSP zu erhalten. Der Schwerpunkt dieser Arbeit gliedert sich in drei Teile.

Es wurden Untersuchungen an der Einzeltropfenverbrennung und der FSP-Synthese von Eisenoxid-Nanopartikeln unter Verwendung von niedrig- und hochflüchtigen Precursoren durchgeführt. Ziel war es, die Mechanismen und die Bedingungen für das Auftreten von Tröpfchen-Mikroexplosionen, die Bildung von Nanopartikeln bei Einzeltropfenverbrennung und FSP sowie die Förderung der homogenen Nanopartikelsynthese aus niedrigflüchtigen Precursoren zu ermitteln. Die Einflüsse der Wahl des Precursors, der Precursorkonzentration und der Lösungsmittelzusammensetzung auf das Verhalten der Tröpfchenverbrennung sowie die Regenbogensignale und die Synthese von Eisenoxidpartikeln wurden experimentell untersucht.

Der Mechanismus und die Bedingungen für das Auftreten von Tröpfchen-Mikroexplosionen werden diskutiert und zusammengefasst, was zu einem besseren Verständnis der Auslösung von Explosionen von Tröpfchen, die Metallnitate enthalten, führt. Die synthetisierten Partikel wurden mittels Brunauer-Emmett-Teller (BET), Röntgenbeugung (XRD) sowie niedrig- und hochauflösender Transmissionselektronenmikroskopie (TEM und HRTEM) charakterisiert, womit die Ähnlichkeit von Nanopartikeln, die einerseits durch Einzeltropfenverbrennung und andererseits mittels der FSP hergestellt wurden, gezeigt wird. Damit lässt sich feststellen, dass die durch Mikroexplosionen induzierte Sekundär-Atomisierung von Tröpfchen die Entstehung von homogenen Nanopartikeln wesentlich fördert.

Anhand dreidimensionaler Messungen zur Doppeltropfenverbrennung des reinen Lösungsmittels und der Vorläuferlösung wird der Einfluss eines benachbarten Tropfens auf das Verbrennungsverhalten (Tropfeninteraktionen) und das Auftreten von Doppeltropfenexplosionen untersucht. Die dazu entwickelte dreidimensionale Messtechnik mit zwei zeitsynchronisierten Hochgeschwindigkeitskameras liefert zeitlich hochaufgelöste Informationen, womit der lokale Tropfendurchmesser, Flammendurchmesser sowie Tropfen-3D-Trajektorien, Tropfen-3D-Geschwindigkeiten und die mittleren Abstände zwischen den beiden brennenden Tropfen ermittelt wird. Damit lassen sich Tröpfcheninteraktionen in der reinen Sauerstoffatmosphäre sowie in einer Mischung aus Sauerstoff- und Stickstoffatmosphäre quantifizieren. Tröpfchen-Mikroexplosionen konnten so erstmalig bei Doppeltropfen-Verbrennungsexperimenten von Precursor-Lösungen beobachtet werden. Dabei zeigt sich, dass Doppeltropfenexplosionen durch Tropfenwechselwirkungen stark beeinflusst werden.

Mittels digitaler Inline-Hologramm-Messungen wird die Verbrennung von Einzeltropfen untersucht. Der Schwerpunkt liegt auf der Erkennung der Größe von nicht brennenden Tropfen und der Abschätzung des Brechungsindexgradienten, der den brennenden Tropfen umgibt. Der konstruierte Versuchsaufbau und die entwickelte Bildverarbeitungsmethode liefern klare

Hologrammsignale, und mit den entwickelten Methoden zur Hologrammbildung und numerische Rekonstruktion lässt sich die Tropfengröße bestimmen. Der Einfluss der umgebenden Flamme auf die Hologrammsignale wird experimentell nachgewiesen, was zur Abschätzung des Brechungsindexgradienten in der Umgebung brennender Tröpfchen eingesetzt werden kann.

Diese Arbeit weist damit nach, dass mit Hilfe von Tropfenverbrennungsexperimenten grundlegende Informationen über Tropfenverbrennung, Explosion und Wechselwirkung für FSP gewonnen werden können. Weiterhin lassen sich diese Untersuchungen dazu nutzen, kostengünstige Precursor-Lösungsmittel-Systeme zur Herstellung homogener Nanopartikel zu erforschen, die Wechselwirkung zwischen brennenden Tröpfchen herauszufinden sowie die Tröpfchenflamme zu verstehen.

Table of Contents

Acknowledgements.....	I
Abstract.....	VII
Zusammenfassung	IX
Preface	XVII
List of Figures	XIX
List of Tables	XXVII
1 Introduction.....	1
1.1 Flame spray pyrolysis for synthesizing nanoparticles	1
1.2 Droplet evaporation and combustion during FSP.....	5
1.3 Single droplet combustion	6
1.4 Thesis objective and outline	9
2 Single droplet combustion and FSP synthesis of iron oxide nanoparticles	13
2.1 State of art.....	13
2.2 Investigation methods.....	16
2.2.1 Precursor solution preparation and analysis.....	16
2.2.2 Particle synthesis	18
2.2.3 Particle characterizations	20
2.2.4 Rainbow refractometry	21
2.3 Results and discussion.....	22
2.3.1 Metal organic precursor: Iron (II) naphthenate.....	23

Table of Contents

2.3.1.1 Single droplet combustion.....	23
2.3.1.2 Micro-explosions during single droplet combustion.....	28
2.3.2 Metal inorganic precursor: Iron (III) nitrate nonahydrate.....	31
2.3.3 Rainbow refractometry measurements of single droplet combustion.....	35
2.3.4 TEM measurements and nanoparticle comparison.....	40
2.4 Summary and conclusions.....	48
2.4.1 Summary.....	48
2.4.2 Conclusions.....	48
3 Three-dimensional measurements of double droplet combustion.....	51
3.1 State of art.....	51
3.2 Experimental setup and procedure.....	54
3.2.1 Setup construction.....	54
3.2.2 Imaging processing.....	58
3.2.3 Definitions of droplet spacing and flame spacing.....	60
3.3 Results and discussion.....	61
3.3.1 Single droplet combustion of p-Xylene in pure oxygen atmosphere.....	62
3.3.2 Double droplet combustion of p-Xylene in pure oxygen atmosphere.....	66
3.3.3 Double droplet combustion of p-Xylene in the mixture of oxygen and nitrogen.....	78
3.3.4 Double droplet combustion of precursor solutions in pure oxygen atmosphere.....	79
3.4 Summary and conclusions.....	86
3.4.1 Summary.....	86

Table of Contents

3.4.2 Conclusions	86
4 Digital in-line holography measurements of single droplet combustion	89
4.1 State of art.....	89
4.2 Theory	91
4.2.1 The wave nature of light and the scalar diffraction theory.....	91
4.2.2 Hologram formation and numerical reconstruction	94
4.2.3 Numerical reconstruction method.....	96
4.3 Experimental setup and procedure	99
4.3.1 Setup construction	99
4.3.2 Effective detector at the focal plane of the objective.....	100
4.3.3 Image processing.....	101
4.4 Results and discussion.....	102
4.4.1 The hologram formation and reconstruction of non-burning droplets.....	103
4.4.2 The preliminary holographic measurements of burning droplets	112
4.5 Summary and conclusions.....	119
4.5.1 Summary	119
4.5.2 Conclusions	120
5 Outlook	121
5.1 Single droplet combustion and FSP synthesis of iron oxide nanoparticles.....	121
5.2 Three-dimensional measurements of double droplet combustion	121
5.3 Digital in-line holography of single droplet combustion	122

Table of Contents

5.3.1 The proposed method to estimate the surrounding refractive index gradient.....	122
Appendix.....	127
A.1 Precursor-solvent combinations used in single droplet combustion experiments.....	127
A.2 BET and XRD measurements of FSP synthesized iron oxide particles.....	130
A.3 Matlab scripts to pre-process hologram images.....	132
A.4 Blur percentage calculation	142
References	145
List of Publications by Haipeng Li.....	159
Co-supervised student work.....	163
Statement by the doctoral candidate	165

Preface

The results presented in this dissertation were mainly obtained during my time as a research assistant from October 2017 to September 2020, with the support of the German Research Foundation (DFG) within the priority program SPP 1980 SPRAYSYN (“Nanoparticle synthesis in spray flames”, website: www.uni-due.de/spp1980/index_en.php). This 3 years’ PhD project is titled as: “Precursor release in nanoparticle producing spray flames: Single droplet investigation of multicomponent mass transfer”. During this time, I was supervised by Prof.-Dr.-Ing. habil. Lutz Mädler.

The results are partially published in the following manuscripts:

[1] Haipeng Li, Norbert Riefler, Thomas Wriedt, Lutz Mädler. Reference data set for three-dimensional measurements of double droplet combustion of p-xylene. Proceedings of the Combustion Institute. 2020. DOI: <https://doi.org/10.1016/j.proci.2020.06.297>.

[2] Haipeng Li, Suman Pokhrel, Marco Schowalter, Andreas Rosenauer, Johannes Kiefer, Lutz Mädler. The gas-phase formation of tin dioxide nanoparticles in single droplet combustion and flame spray pyrolysis. Combustion and Flame. 2020, 215, 389-400. DOI: <https://doi.org/10.1016/j.combustflame.2020.02.004>

[3] Haipeng Li, Christopher D. Rosebrock, Yingchun Wu, Thomas Wriedt, Lutz Mädler. Single droplet combustion of precursor/solvent solutions for nanoparticle production: Optical diagnostics on single isolated burning droplets with microexplosions. Proceedings of the Combustion Institute. 2019, 37, 1203-1211. DOI: <https://doi.org/10.1016/j.proci.2018.06.133>

List of Figures

Figure 1.1: Three classifications of flame aerosol synthesis: vapor-fed aerosol flame synthesis (VAFS), flame spray pyrolysis (FSP), and flame-assisted spray pyrolysis (FASP).	2
Figure 1.2: Sketch of the experimental setup for flame spray pyrolysis (FSP).	3
Figure 1.3: Photographs of the spray flames in FSP experiments to synthesize various nanoparticles: from left to right, Tin oxide (SnO_2), Copper oxide (CuO), Iron oxide ($\text{Fe}_2\text{O}_3+\text{Fe}_3\text{O}_4$), the mixture of Silicon dioxide (SiO_2) and Aluminum oxide (Al_2O_3), Lithium manganese oxide (LiMn_2O_4), and the mixture of Aluminum phosphate (AlPO_4) and LiMn_2O_4	3
Figure 1.4: Schematic diagram of two particle formation mechanisms during FSP (a) and (b), and represented TEM images of iron oxide particles (c) and (d)	6
Figure 1.5: Photographs of the spray flame (a) and the single droplet flame (b).....	8
Figure 1.6: Optical techniques applied on single droplet combustion: shadowgraphy (high-speed camera imaging and backlight), rainbow refractometry, interferometric particle imaging, and digital in-line holography.....	9
Figure 1.7: Hypotheses of this thesis: I. Single droplet combustion experiments to predict nanoparticle quality for FSP, and droplet micro-explosions to promote the production of homogeneous nanoparticles. II. Double droplet combustion experiments to study the occurrence of micro-explosions of two burning droplets, as well as to investigate the influence of droplet interactions on droplet combustion and explosions. III. Digital in-line holography measurements of single droplet combustion experiments to investigate the influence of the surrounding flame.	10
Figure 2.1: Photographs of the spray flames in FSP experiments of FeNAP/p-Xylene solutions with molar concentrations of 0, 0.1, 0.25, and 0.5 mol/L, EtOH, EtOH+EHA, 0.1 mol/L FeNT/EtOH, and 0.1 mol/L FeNT/EtOH+EHA. EtOH+EHA means the mixture of ethanol and 2-ethylhexanoic acid with a volume ratio of 1:1	19
Figure 2.2: Sketch of the experimental setup for single droplet combustion.	20

Figure 2.3: Sketch of the experimental setup for rainbow refractometry.22

Figure 2.4: Merged image sequences of isolated burning droplets of FeNAP/p-Xylene solutions with molar concentrations of 0, 0.1, 0.25 and 0.5 mol/L.....24

Figure 2.5: The high-speed camera recording image sequences of single droplet combustion of 0.25 mol/L FeNAP/p-Xylene.....25

Figure 2.6: Droplet diameter changes of ten burning droplets for single droplet combustion of FeNAP/p-Xylene solutions with molar concentrations of 0, 0.1, 0.25 and 0.5 mol/L27

Figure 2.7: Changes of the normalized squared droplet diameter (top) and burning constant (bottom) for FeNAP/p-Xylene droplets28

Figure 2.8: Thermogravimetric analysis (TGA) and differential thermal analysis (DTA) in the temperature range from 25 to 575°C for p-Xylene (black), FeNAP (red), and 0.1 mol/L FeNAP/p-Xylene.....29

Figure 2.9: Surface micro-explosion mechanism of burning precursor/solvent droplet (top row), and the recorded images of the combustion process of 0.1 mol/L FeNAP/p-Xylene droplet *via* the high-speed camera recording (bottom row).....30

Figure 2.10: Merged image sequences of isolated burning droplets of (a) EtOH, (b) EtOH+EHA, (c) 0.1 mol/L FeNT/EtOH, and (d) 0.1 mol/L FeNT/EtOH+EHA32

Figure 2.11: Changes of the normalized squared droplet diameter of EtOH (black square), EtOH+EHA (green triangle), 0.1 mol/L FeNT/EtOH (blue diamond) and 0.1 mol/L FeNT/EtOH+EHA (red circle).....33

Figure 2.12: Thermogravimetric analysis (TGA) and differential thermal analysis (DTA) in the temperature range from 25 to 575°C for EtOH (black), FeNT (red), EHA (violet), EtOH+EHA (magenta), 0.1 mol/L FeNT/EtOH (olive), and 0.1 mol/L FeNT/EtOH+EHA (blue).....34

Figure 2.13: The recorded rainbow scattering patterns of single droplet combustion of p-Xylene (a), 0.1 (b), 0.25 (c) and 0.5 (d) mol/L FeNAP/p-Xylene36

Figure 2.14: Rainbow signals of burning droplets of xylene (a) and 0.5 mol/L Tin (II) 2-ethylhexanoate dissolved in xylene (b). Simulated temperature gradients from the droplet core to surface (c) and (d).....	37
Figure 2.15: Rainbow signals of 0.1 mol/L FeNAP/p-Xylene droplet (b). The schematic of light rays to explain (a) the first period and (c) the second period of increase and decrease.....	38
Figure 2.16: The recorded rainbow scattering patterns of single droplet combustion of (a) EtOH, (b) EtOH+EHA, (c) 0.1 mol/L FeNT/EtOH, and (d) 0.1 mol/L FeNT/EtOH+EHA.....	39
Figure 2.17: TEM images (first row), high resolution TEM (HRTEM) images (second row), and selected area electron diffractions (third row) of iron oxide particles obtained from FSP and single droplet combustion.....	41
Figure 2.18: Particle size distributions of iron oxide particles obtained from FSP and single droplet combustion	42
Figure 2.19: TEM images (first row), high resolution TEM (HRTEM) images (second row), and selected area electron diffractions (third row) of iron oxide particles obtained from FSP and single droplet combustion.....	44
Figure 2.20: Particle size distributions of iron oxide particles obtained from FSP and single droplet combustion	45
Figure 2.21: (a) Simulated temperature (black line), residence time (blue line) and primary particle diameter (red line) profiles along the centerline of the spray flame.....	47
Figure 3.1: Sketch of the experimental setup for double-droplet combustion.....	55
Figure 3.2: Photographs of the piezoelectric droplet-on-demand generator (a) and the nozzle plate (b). The sketches of nozzle plates for single-droplet generation (c) and double-droplet generation (d)	56
Figure 3.3: Photos of the two three-dimensional adjustment stages for (a) one high-speed camera (Phantom VEO 710L) with an objective (Mitutoyo 375-039) and (b) one high-speed camera	

(Phantom VEO 710L) with a microscopy objective (Olympus SZ1145). (c) Sketch showing the working distance and depth of field of objective.58

Figure 3.4: Image analysis of droplets (a) and flames (b) of a large and a small burning p-Xylene droplets using a Matlab script based on Canny edge detector. The pixel size of the recorded images was measured by taking an image of a glass ruler at the focus plane of the combinations of objective and high-speed camera, as shown in the image (c).59

Figure 3.5: The schematics showing how to measure 3D locations (middle column), droplet diameters (middle column), and flame diameters (right column): (a) using droplet frame in the x-y plane, and (b) using flame frame in the x-z plane60

Figure 3.6: The schematics showing definitions of droplet spacing (top) and flame spacing (bottom)61

Figure 3.7: High-speed camera recorded (a) droplet frames in the x-y plane and (b) flame frames in the x-z plane of single droplet combustion of p-Xylene in pure oxygen atmosphere63

Figure 3.8: The visualized 3D image of the single burning p-Xylene droplet in Figure 3.7 at $t=2.55$ ms.....64

Figure 3.9: Measured data from five single isolated burning p-Xylene droplets: (a) droplet diameter, (b) flame diameter, (c) the mean droplet diameter (black curve) and the mean flame diameter (red curve), and their polynomial fitting curves (dotted lines), (d) the poly-fitting curves, (e) the normalized squared droplet diameter, and (f) the burning constant.....65

Figure 3.10: High-speed cameras recorded (a) droplet frames in the x-y plane and (b) flame frames in the x-z plane of the weak interaction case of double droplet combustion in pure oxygen atmosphere67

Figure 3.11: Measured data from the weak interaction case of double droplet combustion: (a) droplet diameter changes (solid circles) and flame diameter changes (empty circles), and their polynomial fitting curves (dotted lines), (b) polynomial fitting curves, (c) the comparison of droplet

diameters and flame diameters with single droplet combustion, and (d) droplet spacing and flame spacing68

Figure 3.12: The visualized 3D image of the weak interaction case in Figure 3.10 at $t=2.5$ ms.69

Figure 3.13: The two time-synchronized high-speed cameras recorded (a) droplet frames in the x-y plane and (b) flame frames in the x-z plane of the strong interaction case of double droplet combustion in pure oxygen atmosphere.....70

Figure 3.14: Measured data from the strong interaction case of double droplet combustion: (a) droplet diameter changes (solid circles) and flame diameter changes (empty circles), and their polynomial fitting curves (dotted lines), (b) polynomial fitting curves, (c) the comparison of droplet diameters and flame diameters with single droplet combustion, and (d) droplet spacing and flame spacing71

Figure 3.15: (a) Comparison of the flame standoff ratio, (b) the captured droplet and flame frames at the minimum flame spacing of the strong interaction case [dashed vertical red line in (a)], (c) the captured droplet and flame frames at the minimum flame spacing of the weak interaction case [dashed vertical purple line in (a)]73

Figure 3.16: Comparison of single droplet combustion with the strong interaction case of double droplet combustion: (a) normalized squared droplet diameter, (b) burning constant. Comparison of single droplet combustion with the strong interaction case of double droplet combustion: (c) normalized squared droplet diameter, (d) burning constant.....76

Figure 3.17: The two time-synchronized high-speed cameras recorded (a) droplet frames in the x-y plane and (b) flame frames in the x-z plane of double droplet combustion of p-xylene in the mixed gases (200 mL/min oxygen and 200 mL/min nitrogen).....79

Figure 3.18: High-speed cameras recorded [(a), (c)] droplet frames in the x-y plane and [(b), (d)] flame frames in the x-z plane of single droplet combustion of 0.5 mol FeNAP/p-Xylene in pure oxygen atmosphere80

Figure 3.19: High-speed cameras recorded [(a), (c)] droplet frames in the x-y plane and [(b), (d)] flame frames in the x-z plane of double droplet combustion of 0.5 mol FeNAP/p-Xylene in pure oxygen atmosphere	82
Figure 3.20: High-speed cameras recorded [(a), (c)] droplet frames in the x-y plane and [(b), (d)] flame frames in the x-z plane of double droplet combustion of 0.5 mol FeNAP/p-Xylene in pure oxygen atmosphere	83
Figure 3.21: Comparison of single droplet combustion with the weak interaction case (a) and strong interaction case (b) of double droplet combustion of 0.5 mol FeNAP/p-Xylene: normalized droplet explosion time (left axis, solid lines, solid points), and normalized times between two successive explosions (right axis, hollow points, dashed lines)	85
Figure 4.1: Sketch of the scalar diffraction theory.....	94
Figure 4.2: Sketch of the hologram formation.....	95
Figure 4.3: Sketch of the hologram numerical reconstruction.....	96
Figure 4.4: The conversion from the Cartesian coordinate x_i, y_i, z_i to the spherical coordinate (r, θ, ϕ)	97
Figure 4.5: Sketch (a) and photos (b) of the experimental setup for digital in-line holography. It consists of a laser, optical filters, a beam expansion and collimating lens system, and the recording system. The holograms of burning droplet (c) and non-burning droplet (d) are recorded via the recording system (e).....	100
Figure 4.6: Sketch of the influence of the objective on the recording system.....	101
Figure 4.7: Processing of hologram images: (a) raw hologram, (b) hologram after removed background, (c) selected area of interest, and (d) extracted data	102
Figure 4.8: Digital in-line holography: diffraction dominated scattering	103
Figure 4.9: The simulation of a particle with a diameter of 120 μm at various recording distances from 5, 10, 20, 30, to 50 mm. (a) hologram formation, (b) numerical reconstruction, (c) density	

distribution horizontal through the center of the hologram, and (d) density distribution horizontal through the center of the reconstructed object 105

Figure 4.10: The simulation of particles with various diameters from 70, 120, 170, 220, to 270 μm at a fixed recording distance of 30 mm. (a) hologram formation, (b) numerical reconstruction, (c) density distribution horizontal through the center of the hologram, and (d) density distribution horizontal through the center of the reconstructed object 108

Figure 4.11: Numerical reconstruction of one particle with the diameter of 240 μm and the recording distance of 30 mm 109

Figure 4.12: Hologram images from experiment (a) and simulation (b), and their intensity distribution comparison (c). 111

Figure 4.13: Reconstructed images from experiment (a) and simulation (b), and their intensity distribution comparison (c). 111

Figure 4.14: Reconstructed images (left column) and threshold images (middle column) from experiment (a) and simulation (b), as well as the droplet image captured by a high-resolution CCD camera (c)..... 112

Figure 4.15: Schematic illustration of the two nanoparticle formation paths during single droplet combustion of Tin 2-EHA/Xylene: steady combustion (left) and droplet surface μ -explosion (right) 113

Figure 4.16: Comparisons between single droplet combustion of xylene and 0.5 mol/L Tin 2-EHA/Xylene: (a) flame standoff ratio, (b) flame diameter and (c) droplet diameter 115

Figure 4.17: Frames of droplet (top arrow), flame (middle arrow), and hologram (bottom arrow) of the selected four instances during single droplet combustion of xylene..... 117

Figure 4.18: Frames of droplet (top arrow), flame (middle arrow), and hologram (bottom arrow) of the selected four instances during single droplet combustion of 0.5 mol/L Tin 2-EHA/Xylene. 117

Figure 4.19: Hologram signals of the selected four instances during single droplet combustion of xylene (green solid curve) and 0.5 mol/L Tin 2-EHA/Xylene (red dash curve): (a) ignition, (b) largest flame, (c) shrinkage, and (d) just before the first explosion. 118

Figure 5.1: Sketch of the refractive index gradient surrounding the burning droplet 124

Figure 5.2: Sketch of the multilayered sphere model..... 125

Figure A.1: BET specific surface area of FSP synthesized particles using (a) iron (II) naphthenate diluted with p-Xylene with a metal concentration of 0.1, 0.25, and 0.5 mol/L, and (b) 0.1 mol/L iron(III) nitrate nonahydrate diluted with ethanol and the mixture of ethanol and 2-ethyhexanoate acid 130

Figure A.2: XRD patterns of iron oxide particles prepared by FSP using iron (II) naphthenate diluted with p-Xylene with a metal concentration of 0.1, 0.25, and 0.5 mol/L, and (b) 0.1 mol/L iron(III) nitrate nonahydrate diluted with ethanol and the mixture of ethanol and 2-ethyhexanoate acid 131

Figure A.3: Diagram of the algorithm to calculate blur percentage 143

List of Tables

Table 2.1: Properties of precursors and solvent used in the present work.	17
Table 2.2: Dissolution tests of precursor-solvent combinations.....	18
Table 3.1: The two synchronized high-speed-camera recording systems used in the present work.	57
Table 3.2: Information of the weak interaction case [$Min(SF) = 1.7$] and the strong interaction case [$Min(SF) = 1.2$] of double droplet combustion, at the moment of their corresponding minimum flame spacing.	74
Table 3.3: Accuracies of the measured information. The accuracy of time resolution is calculated according to the recording speed rate of the used high-speed camera. The other accuracies of others are calculated according to the pixel sizes of the used high-speed camera and objectives.	77
Table 4.1: Two sets of simulations on hologram formation and numerical reconstruction of nonburning droplets.	104
Table 4.2: The spatial frequency of fringes in hologram images in the two sets of simulations on hologram formation and numerical reconstruction of nonburning droplets.....	107
Table 4.3: Particle diameters obtained from numerical reconstruction and their deviation compared to input particle diameter.	110
Table 4.4: Droplet diameter, flame diameter and flame standoff ratio of the selected four instances during single droplet combustion of xylene and 0.5 mol/L Tin 2-EHA/Xylene.	116
Table A.1: The precursor-solvent combinations during whose single droplet combustion experiments μ -explosions were observed.	127
Table A.2: The precursor-solvent combinations during whose single droplet combustion experiments μ -explosions were not observed.	128
Table A.3: Properties of precursors and solvents used in single droplet combustion.....	129

1 Introduction

The history of flame aerosol synthesis of particles can date back to prehistoric period where the soot from fires was used to paint scenes on cave walls, and also to ancient China where carbon black was manufactured from flame generated aerosol for the application of pigment [1]. Today, flame aerosol synthesis has been widely used in industry to synthesize nanostructured materials at a production rate of millions of tons, valued at more than 15 billion \$ per year [2].

1.1 Flame spray pyrolysis for synthesizing nanoparticles

Depending on the precursor state fed to the flame and the combustion energy source, flame aerosol synthesis (also called flame aerosol technology) is classified into three general categories (**Figure 1.1**): vapor-fed aerosol flame synthesis (VAFS), flame spray pyrolysis (FSP), and flame-assisted spray pyrolysis (FASP) [3-5]. As the youngest one, FSP has important technological elements including self-sustaining flame, usage of liquid feeds and less volatile precursors, proven scalability, high temperature flames, and large temperature gradients [6-8]. This versatile and promising technique has proved its ability to do fast and scalable synthesis of a wide variety of single- and multi-component nanoparticles in one-step. The synthesis of composite materials can be fulfilled by mixing different precursor solutions [5], and the synthesis of pure-phase and homogeneous particles can be achieved through controlling the precursor-solvent composition [6, 8]. Until now, the FSP synthesized particles have been widely used in the functional applications including, such as but not limited, catalysis, sensors, phosphors, electroceramics, membranes, super-hydrophilic coatings, biomaterials, electrode fabrication, nanoparticle film fabrication, and batteries. More details about the history, development, application, challenge, and perspective of FSP technology were described in the reviews of Refs. [3-5, 9, 10].

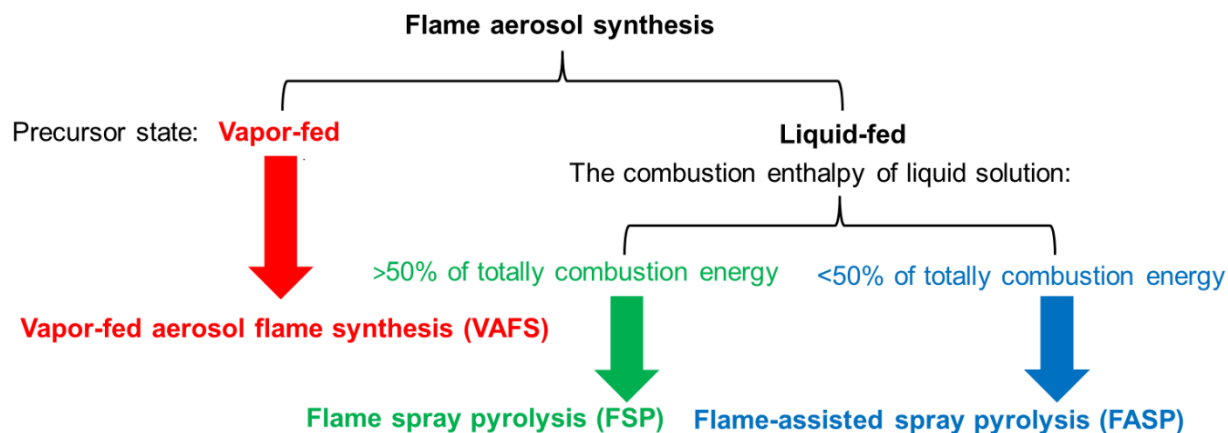


Figure 1.1: Three classes of flame aerosol synthesis: vapor-fed aerosol flame synthesis (VAFS), flame spray pyrolysis (FSP), and flame-assisted spray pyrolysis (FASP). The classification is based on the precursor state fed to the flame and the combustion energy source.

FSP experiments were conducted by different kinds of nozzles. Here, the spray process using the classical two-fluid nozzle designed by Mädler et al. [11, 12] will be briefly introduced. **Figure 1.2** shows the sketch of the experimental setup for FSP. During FSP synthesis, the liquid-phase and/or solid-phase precursors are totally dissolved in combustible organic solvents with the help of an ultrasonic vibrator or under reflex at a high temperature [13, 14]. The solution is fed to a two-fluid nozzle with a syringe pump at a liquid flow rate, and then atomized into small droplets by the dispersed oxygen to accelerate vaporization and subsequently reaction. A concentric supporting flamelet ring (6 mm in radius) of premixed methane/oxygen is implemented to ignite the atomized droplets in order to maintain the spray flame. A glass microfiber filter is fixed above the downstream of the nozzle, where particles are deposited with the aid of a vacuum pump. **Figure 1.3** shows the photographs of the spray flames in FSP experiments to synthesize different kinds of nanoparticles. Two types of nanoparticles were mixed at nanoscale using double-flame spray (**Figure 1.3** right photo) in order to improve the functional performance [15].

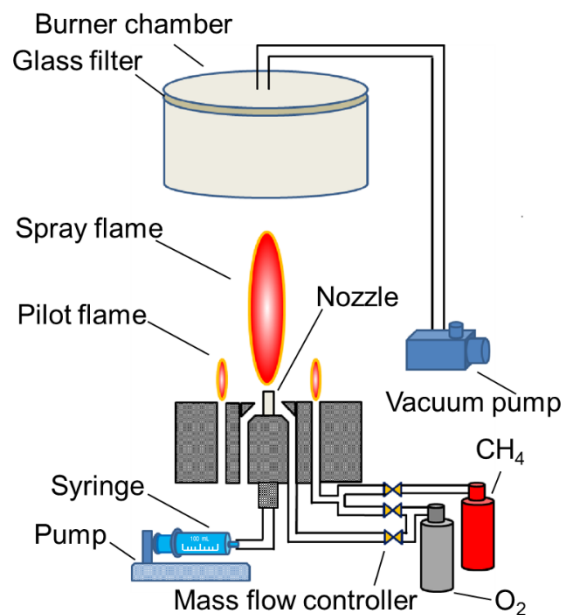


Figure 1.2: Sketch of the experimental setup for flame spray pyrolysis (FSP).

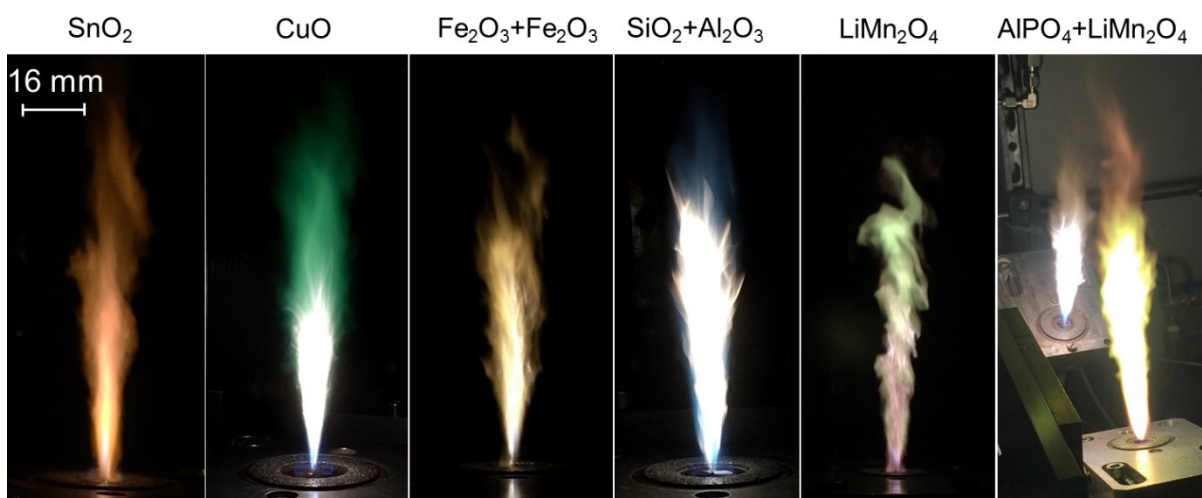


Figure 1.3: Photographs of the spray flames in FSP experiments to synthesize various nanoparticles: from left to right, Tin oxide (SnO₂), Copper oxide (CuO), Iron oxide (Fe₂O₃+Fe₃O₄), the mixture of Silicon dioxide (SiO₂) and Aluminum oxide (Al₂O₃), Lithium manganese oxide (LiMn₂O₄), and the mixture of Aluminum phosphate (AlPO₄) and LiMn₂O₄. These photographs were taken with reduced light intensity in the background.

FSP synthesis of nanomaterials is famous and attractive for its reproducibility and scalability, and therefore this technique has great potential applications in industry for commercial scale-up production. The transfer of FSP nanoparticle synthesis from gram-level lab-scale to pilot reactors has been successfully demonstrated by several examples, *e.g.*, bismuth oxide (Bi_2O_3) and zirconium oxide (ZrO_2) nanoparticles, with production rates of up to a few kilograms per hour [16]. A prototype industrial FSP production line has been designed and constructed to produce ZrO_2 nanoparticles to 5 kg/h, and prices found in competitors demonstrate that FSP technology can reduce at least 50 % of commercial prices (Advance-FSP, http://cordis.europa.eu/result/rcn/141570_en.html). FSP pilot plants have been installed and used at ETH Zurich, ARCI (Hyderabad, India), Tecan (Los Arco, Spain), and Johnson Matthey Technology Center (UK) [16]. For the purpose of widening industrial applications of FSP synthesized nanomaterials, fundamental understanding of the flame chemistry and the liquid-vapor-flame-particle process chain is a prerequisite and essential [9, 17].

Since 2017, with the support of the German Research Foundation (DFG) within the priority program SPP1980 (“Nanoparticle Synthesis in Spray Flames”), one standardized spray-flame burner (SpraySyn) was developed at University of Duisburg-Essen and subsequently installed in more than twelve laboratories in Germany for the purpose of fundamental investigations of spray-flame synthesis [9, 17, 18]. The usages of the standardized spray-flame burner, the common experimental configuration, and the predefined materials systems guarantee the reproducible standardized experiments in each laboratory. The investigation of the standardized spray flames with different kinds of complementary techniques aims to provide comprehensive data to develop and compare various theoretical calculations and simulation approaches [9]. More detailed information about the priority program SPP1980 including *in-situ* diagnostics, theory and simulation, and process can be found at www.spraysyn.org.

1.2 Droplet evaporation and combustion during FSP

During FSP synthesis, pure oxygen disperses precursor solutions into small droplets. These sprayed droplets are ignited by a pilot flame to form a large spray flame, where particle formation takes place *via* precursor evaporation/decomposition, particle nucleation, growth by coalescence and sintering, aggregation, as well as agglomeration [5]. Two particle formation routes are proposed to explain the particle formation mechanism during FSP [4, 8, 19], as shown in **Figure 1.4**. One is gas-to-particle conversion (green marked in **Figure 1.4 b and d**), which is characterized by the entire transfer of the liquid-phase precursor into gas-phase, and the synthesis of homogeneous particles with well-controlled properties [8, 19, 20]. This route is similar to reactions that happen in vapor-fed aerosol flame synthesis (VAFS) and soot formation [21]. The other is droplet-to-particle conversion (red marked in **Figure 1.4 a and c**), where the incomplete vaporization of the precursor resulting in precipitation and conversion within spray droplets. As a result, large, dense and/or hollow particles are formed [8, 22]. While the latter route is suitable for the production of ceramic powders and films [22], the former route has attracted more attentions of laboratory studies and industrial scale-up productions due to the wide applicability of homogeneous nanoparticles. The mass transfer of the precursor from liquid-droplet to gas-phase decides the particle quality, and thus fundamental investigations on droplet evaporation and combustion of the FSP precursor solutions are required. While various optical diagnostics have been used to *in-situ* analyze the gas-phase flame and nanoparticle synthesis [23], the measurements on droplet evaporation and combustion in the spray flame are still challenging. It is because of the interactions between the spray droplets [24], the high flame temperature (could be more than 2000 K [11]), the steep temperature gradients around flame axis [25], the turbulence caused by the high-speed dispersion [26], and the short time scales (around a few milliseconds [27]). As an alternative, single droplet combustion have shown to be helpful to provide fundamental insights into the mechanisms of droplet combustion in spray flames [6, 28-34].

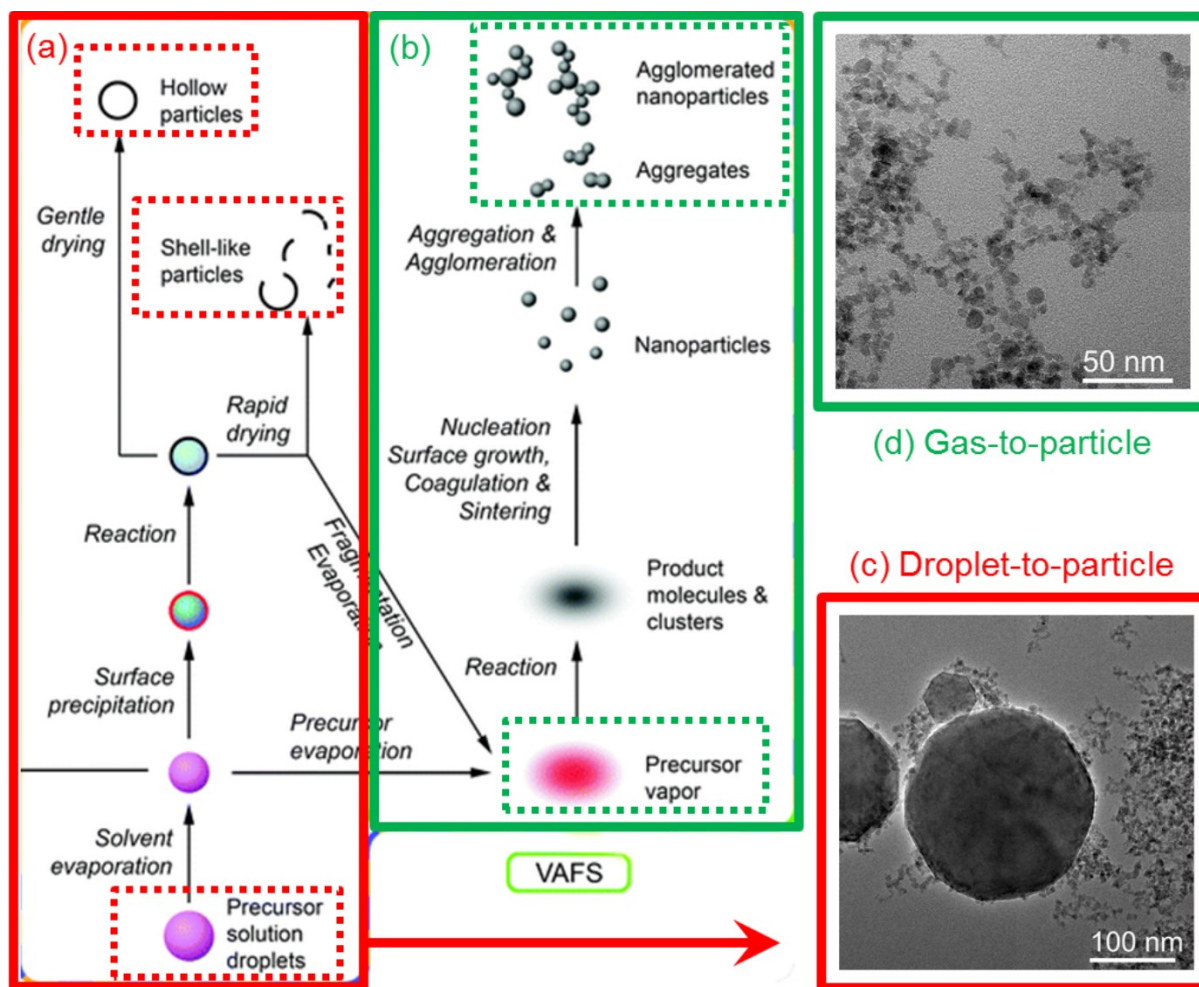


Figure 1.4: Schematic diagram of two particle formation mechanisms during FSP (a) and (b), and represented TEM images of iron oxide particles (c) and (d). Schematic diagram is adapted and reprinted with the permission from Ref. [4]. The TEM images shows the inhomogeneous (c) and homogeneous (d) iron oxide particles synthesized from droplet-to-particle conversion (a) and gas-to-particle conversion (b), respectively.

1.3 Single droplet combustion

The liquid spray flames are composed of groups of individual droplets. Understanding single droplet combustion is expected to promote a better understanding of spray flame combustion [35]. Furthermore, spray combustion in practical applications is significantly controlled by the combustion of each of the droplets, and thus the understanding of droplet combustion behaviors

is of great significance [36]. Single droplet combustion experiments have been proved to be able to provide fundamental information for FSP, including understanding of the formation process from droplet to particle [6, 28, 31, 33], comparing the nanoparticles produced from single droplet combustion and FSP [6, 31, 33], exploring low-volatility and low-cost precursors [6, 33], investigating the influence of ambience [37], and providing experimental data for FSP simulation [21, 34]. Rosebrock *et al.* first used the FSP precursor solutions in single droplet combustion experiments, and observed the micro-explosion behaviors (disruptive combustion) of these droplets *via* the high-speed camera imaging technique [31]. Similarly, μ -explosion behaviors were observed by Li *et al.* during the single droplet combustion of highly reactive precursor solutions, where titanium tetraisopropoxide (TTIP) was selected as the precursor [28]. The droplet μ -explosion mechanism based on shell formation and subsequent heterogeneous vapor nucleation was proposed by Rosebrock *et al.* [31, 33]. The thermal decomposition of the metal-organic precursor occurs within the burning droplets, which leads to a viscous shell that inhibits vaporization, initiating internal vapor phase nucleation that finally causes droplet micro-explosions [28, 31]. One example to show droplet μ -explosion is the single droplet combustion of 0.25 mol/L Iron(II) naphthenate dissolved in p-Xylene (**Figure 1.5 b**, photograph was taken by a normal CCD camera). To the best of my knowledge, μ -explosions have been observed *via* high-speed camera imaging technique during single droplet combustion experiments of many FSP precursor solutions. Detailed descriptions are shown in **Appendix A.1**.

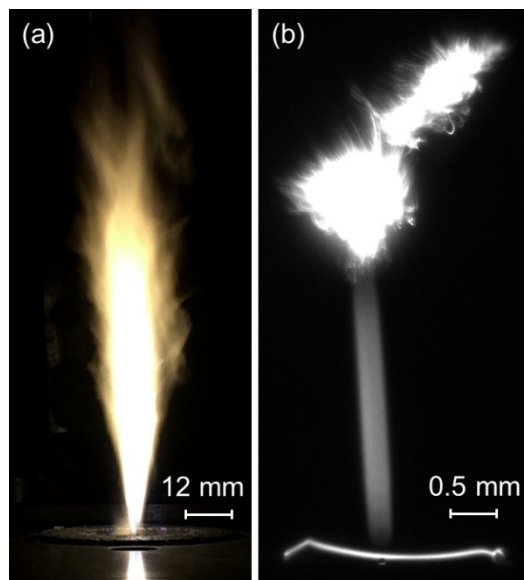


Figure 1.5: Photographs of the spray flame (a) and the single droplet flame (b). The length of the spray flame and the single droplet flame are around 116 mm and 3 mm, respectively. The precursor solution is 0.25 mol/L Iron(II) naphthenate dissolved in p-Xylene.

To study single droplet combustion of precursor solutions, various optical techniques (**Figure 1.6**) have been used including:

- (1) Shadowgraphy (high-speed camera imaging and backlight) to detect droplet size and velocity, flame size, and droplet micro-explosion behaviors [6, 28, 31, 33, 37-39].
- (2) Rainbow refractometry to measure droplet temperature changes and composition changes [29, 30, 32].
- (3) Interferometric particle imaging to determine droplet size changes [29, 30, 32].
- (4) Digital in-line holography to detect droplet size, 3D location, velocity, and the refractive index surrounding the burning droplet.

In addition, transmission electron microscopy (TEM) measurements were performed to characterize size distribution and morphology of particles prepared by single droplet combustion [6, 28, 33, 38].

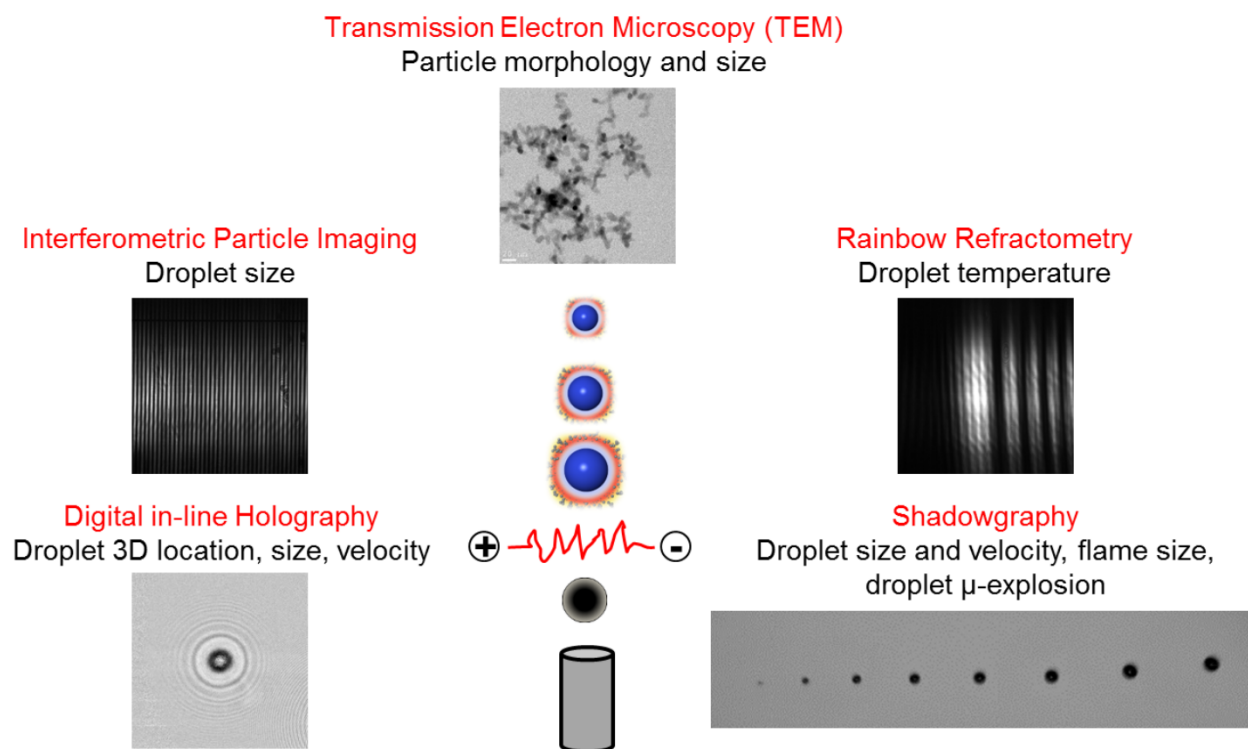


Figure 1.6: Optical techniques applied on single droplet combustion: shadowgraphy (high-speed camera imaging and backlight), rainbow refractometry, interferometric particle imaging, and digital in-line holography. Transmission electron microscopy (TEM) was used to characterize particles prepared by single droplet combustion.

1.4 Thesis objective and outline

The main objective of this thesis is to provide fundamental information for droplet combustion and particle formation in the FSP technique, using single and double droplet combustion experiments. To achieve this objective, the following three hypotheses will be experimentally investigated (**Figure 1.7**):

- I. Single droplet combustion experiments are able to predict nanoparticle quality for FSP, and droplet micro-explosions promote the production of homogeneous nanoparticles.

- II. Droplet micro-explosions occur not only in single droplet combustion experiments but also in double droplet combustion experiments. Droplet interactions affect the occurrence of micro-explosions.
- III. The heat and mass transfer between the burning droplet and its surrounding flame contribute to the occurrence of droplet micro-explosions.

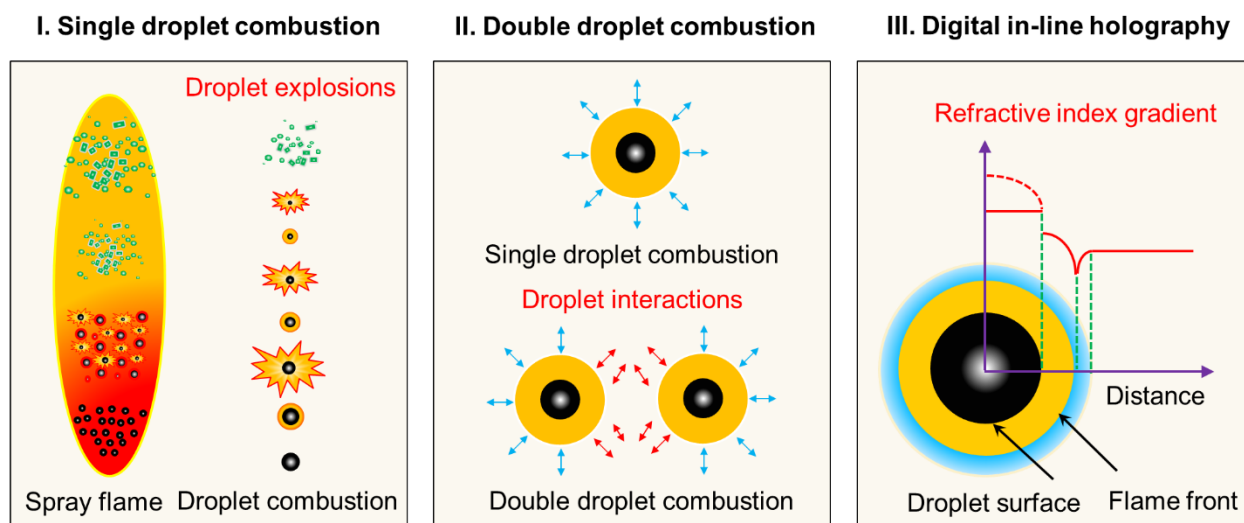


Figure 1.7: Hypotheses of this thesis: I. Single droplet combustion experiments to predict nanoparticle quality for FSP, and droplet micro-explosions to promote the production of homogeneous nanoparticles. II. Double droplet combustion experiments to study the occurrence of micro-explosions of two burning droplets, as well as to investigate the influence of droplet interactions on droplet combustion and explosions. III. Digital in-line holography measurements of single droplet combustion experiments to investigate the influence of the surrounding flame.

To study these three hypotheses, the following research methods are proposed:

- (1) Single droplet combustion experiments using low- and high-volatility precursors aim to investigate the mechanism and occurrence conditions of droplet micro-explosions, nanoparticle formations in single droplet combustion and FSP, and the promotion of the production of homogeneous nanoparticles using low-volatility precursors.

- (2) Double droplet combustion experiments using the pure solvent and the precursor solution target to study the influence of neighboring droplet on combustion behaviors, especially the occurrence of double droplet explosions.
- (3) Digital in-line holography technique is developed and further performed to detect the sizes of non-burning droplets, and to estimate the influence of the surrounding flame on the burning droplet.

According to the proposed hypotheses and the proposed research methods, the outline of this thesis is divided into three parts:

- I. Single droplet combustion and FSP synthesis of iron oxide nanoparticles (**Chapter 2**).
- II. Three-dimensional measurements of double droplet combustion (**Chapter 3**).
- III. Digital in-line holography measurements of single droplet combustion (**Chapter 4**).

The outlook for these investigated topics are listed in **Chapter 5**, and the supporting information are shown in **Appendix**.

2 Single droplet combustion and FSP synthesis of iron oxide nanoparticles¹

2.1 State of art

Iron oxide nanoparticles have attracted significant attentions due to their unique properties at nanoscale and their potential functional applications, such as ferrofluids, catalysts, and biotechnology [40-42]. According to the Fe oxidation state (Fe^{2+} or Fe^{3+}), iron oxide particles normally exhibit in one of the four main crystal structures including: wustite (FeO), magnetite (Fe_3O_4), maghemite ($\gamma\text{-Fe}_2\text{O}_3$), and hematite ($\alpha\text{-Fe}_2\text{O}_3$) [43, 44]. While hematite possesses promising catalytic properties, maghemite and magnetite show exceptional magnetic properties [45]. Compared to bulk, particles at nanoscale could have distinctively different properties. For example, iron oxide nanoparticles (maghemite and magnetite) tends to be superparamagnetic when its size is below 20 nm [46].

The fast synthesis of iron oxide nanoparticles in one-step *via* FSP has been successfully demonstrated by many researchers [5]. Li *et al.* first applied FSP to produce superparamagnetic bare and silica-coated maghemite nanoparticles, and demonstrated the feasibility of the prepared particles for protein adsorption and desorption [47, 48]. For the first time, Strobel and Pratsinis utilized FSP to directly prepare magnetic iron oxide nanoparticles in the form of magnetite and wustite under controlled atmosphere [49]. Li *et al.* controlled particle residence time in the flame and flame atmosphere in FSP to synthesize core-shell structured nanoparticles, consisting of metallic iron core (30-80 nm in diameter) and magnetite shell (4-6 nm in thickness) [50]. Harra *et al.* used FSP-synthesized maghemite nanoparticles to generate encapsulated iron oxide-titanium dioxide ($\gamma\text{-Fe}_2\text{O}_3\text{-TiO}_2$) composite nanoparticles, which can be used as magnetically separable photocatalyst for water treatment applications [51]. Tepluchin *et al.* utilized double FSP to prepare

¹ The results presented in this chapter are partially published in the following manuscripts:

H. Li, S. Pokhrel, M. Schowalter, A. Rosenauer, J. Kiefer, L. Mädler. The gas-phase formation of tin dioxide nanoparticles in single droplet combustion and flame spray pyrolysis. *Combustion and flame*. 2020, 215, 389-400.

H. Li, C.D. Rosebrock, Y. Wu, T. Wriedt, L. Mädler. Single droplet combustion of precursor/solvent solutions for nanoparticle production: Optical diagnostics on single isolated burning droplets with microexplosions. *Proceedings of the Combustion Institute*. 2019, 37, 1203-1211.

$\text{FeO}_x/\text{Al}_2\text{O}_3$ samples to minimize the formation of composite phases [52]. Improvements of the catalytic performance can be gained especially for low Fe-based samples. Rajput *et al.* used FSP to prepare superparamagnetic maghemite nanoparticles, which can successfully remediate Pb^{2+} and Cu^{2+} from water [53].

In the previous studies, organic iron precursors with high combustion enthalpies were used because homogeneous nanoparticles were formed *via* the gas-to-particle conversion. However, organic precursors are expensive, which is a large cost factor for industrial scale-up [16]. Therefore, exploring low-cost inorganic precursors are more attractive to diminish the production cost in industry. However, inorganic precursors, *i.g.*, nitrates, have lower combustion enthalpies than organic precursors, reducing the whole combustion enthalpy of precursor solutions. As a result, inhomogeneous particles are synthesized *via* the droplet-to-particle conversion, which contain hollow and shell-like particles even at micro-size. Thus, a lot of work has been conducted to investigate the nanoparticle formation process in spray flames, aiming to promote the formation of homogeneous particles *via* the gas-to-particle conversion using low-cost metal nitrate precursors. Strobel and Pratsinis studied the effect of solvent composition on nanoparticle formation during FSP synthesis using different metal nitrates [$\text{Al}(\text{NO}_3)_3 \cdot 9\text{H}_2\text{O}$, $\text{Co}(\text{NO}_3)_2 \cdot 6\text{H}_2\text{O}$, $\text{Fe}(\text{NO}_3)_3 \cdot 9\text{H}_2\text{O}$, $\text{Mg}(\text{NO}_3)_2 \cdot 6\text{H}_2\text{O}$, and $\text{Mn}(\text{NO}_3)_2 \cdot 6\text{H}_2\text{O}$]. They indicated that the usage of 2-ethylhexanoic acid (2-EHA) promotes the conversion of metal nitrates to volatile metal carboxylates, enhancing the formation of homogeneous nanoparticles *via* gas-to-particle route [8]. Rudin *et al.* decoupled the flame enthalpy content from the precursor solution chemistry with a second assisted flame, and prepared homogeneous bismuth nanoparticles using $\text{Bi}(\text{NO}_3)_3 \cdot 5\text{H}_2\text{O}$ as the precursor [54]. Harra *et al.* studied the effect of the EHA concentration on particle formation in liquid flame spray (LFS) using aluminum nitrate precursor dissolved in ethanol and EHA. They found that the residual particles dominate the mass size distribution when using pure ethanol as solvent [19]. However, adding only 5% (volume) of EHA can shift the mass practically entirely to

the nanoparticle mode. Wei *et al.* investigated the role of solvent formulations in temperature-controlled liquid-fed aerosol flame synthesis of YAG-based nanoparticles. They demonstrated that adding EHA into ethanol in a volume ratio of 1:1 dramatically converts hollow inhomogeneous particles to homogeneous nanoparticles, which is caused by the formation of 2-ethyhexanates due to the ligand exchange of metal nitrates [55]. Angel *et al.* synthesized La(Fe, Co)O₃ nanoperovskites in a spray flame using metal nitrates. They indicated that experiments with ethanol as the solvent lead to a broad particle-size distribution and the formation of undesired phases, but the addition of EHA gives the formation of single-phase and high surface area nanoparticles with a narrow size distribution [56]. Abram *et al.* have done flame synthesis of nanophosphors using a novel micro-jet atomization technique, and found that reducing the spray droplet size and increasing the flame temperature promote the gas-to-particle route for metal nitrate precursors [57]. Sorvali *et al.* studied the effect of solvent composition and gas flow rates on the crystallographic phase composition and the quality of the synthesized iron oxide nanoparticles in a liquid flame spray process from iron nitrate [45]. Zhang *et al.* employed flame aerosol synthesis method and the precursor solution of dissolving iron(III) nitrate nonahydrate in water to prepare iron oxide nanoparticles, which were further converted into ultra-fine iron powders combining with a post-reduction heat treatment process [58]. Carvajal investigated the effect of spray parameters in a spray flame reactor during iron oxide nanoparticle synthesis. Their results showed that using propionic acid as solvent results in the formation of homogeneous nanoparticles from iron nitrate precursor [59]. Reviewing the previous work, synthesis of homogeneous nanoparticle from metal nitrate precursors using FSP or other liquid spray flame ways are achieved through four paths: (1) converting metal nitrates to volatile metal carboxylates using organic acids, (2) reducing size of dispersed droplets, (3) increasing temperature (enthalpy content) of the spray flame, and (4) applying post-treatment. Considering the cost-effectiveness and operational requirements, the first path is the most promising.

Single droplet combustion has been used to study the synthesis of homogeneous nanoparticles from metal nitrate precursors. Rosebrock *et al.* have done single droplet combustion and FSP experiments using metal nitrate precursors $[\text{Al}(\text{NO}_3)_3 \cdot 9\text{H}_2\text{O}$ and $\text{Fe}(\text{NO}_3)_3 \cdot 9\text{H}_2\text{O}]$. They found that adjusting the solvents could induce droplet explosions of low-volatile precursors during single droplet combustion, promoting the synthesis of homogeneous nanoparticles from both single droplet combustion and FSP [33]. Similar phenomena were found by Meierhofer *et al.* during screening various precursor solutions for $\text{Li}_4\text{Ti}_5\text{O}_{12}$ energy storage materials using FSP. They indicated that using 2-ethylhexanoic acid (EHA) instead of ethanol as the solvent induces droplet explosions and promoted the complete droplet combustion, resulting in homogenous nanoparticle synthesis [6]. While promising conclusions are obtained from these previous works, related in-depth investigations are still lacking, *e.g.*, the mechanism and occurrence conditions of droplet micro-explosion, triggering explosions of droplets containing metal nitrates, and explaining the similarity of nanoparticles prepared from single droplet combustion and FSP. Therefore, the detailed knowledge is yet to be acquired. In this chapter, the effects of precursor choice, precursor concentration and solvent composition on the synthesis of iron particles are experimentally investigated using single droplet combustion and FSP.

2.2 Investigation methods

2.2.1 Precursor solution preparation and analysis

Iron (II) naphthenate (80% in mineral spirits, Alfa-Aesar) and Iron (III) nitrate nonahydrate (>98%, Alfa-Aesar) were used as iron precursors. P-Xylene (analysis EMSURE® ISO, Sigma-Aldrich), ethanol (assay 100%, VWR), and 2-ethylhexanoic acid (99%, Sigma-Aldrich) were selected as solvents. **Table 2.1** lists properties of these precursors and solvents. The organic iron precursor of Iron (II) naphthenate has a price (€/mol) of three times higher than the inorganic precursor of Iron (III) nitrate nonahydrate.

Table 2.1: Properties of precursors and solvent used in the present work.

Precursor/solvent	Iron (III) nitrate nonahydrate	Iron (II) naphthenate	p-Xylene	Ethanol	2-ethylhexanoic acid	Water
Abbreviation	FeNT	FeNAP	/	EtOH	EHA	H ₂ O
Linear formula	Fe(NO ₃) ₃ *9H ₂ O	Fe(C ₁₁ H ₇ O ₂) ₂	C ₆ H ₄ (CH ₃) ₂	CH ₃ CH ₂ OH	CH ₃ (CH ₂) ₃ CH(C ₂ H ₅)CO ₂ H	H ₂ O
Physical form	Solid	Liquid	Liquid	Liquid	Liquid	Liquid
Density, g/mL	1.684	1.050	0.860	0.790	0.903	0.997
Viscosity, mPa*s at 25°C	/	/	1.197	1.074	7.5 at 20°C	0.890
Flash point, °C	/	> 38	24	12	> 63	/
Melting point, °C	47	/	13.3	-117.0	-59.0	0.0
Boiling point (T _b), °C	Thermally decompose	Thermally decompose	138.4	78.3	228.1	100.0
Adiabatic flame temperature ^[60] , °C	/	/	2865	2716	2867	/
Heat of evaporation ^[61] , kJ/mol, at 25°C	/	/	42.4	42.32	75.6	43.98
Heat of evaporation ^[61] , kJ/mol, at T _b	/	/	35.7	38.56	~ 67 ^[62]	40.65
Heat of formation ^[63] , kJ/mol, at 25°C	/	/	- 25.4	-277.6	- 635.1	- 57.8
Heat of combustion, kJ/mol, at 25°C	/	/	- 4551.8	-1366.9	- 4799.6 ^[64]	/
Price, €/mol	9.2	30.3	10.8	2.3	13.7	/

Heat of combustion is calculated as the differences between the heat of formation of the products and reactants according to the Ref. [63]. The values are taken at one atmosphere pressure. The symbol / represents no available information.

The dissolution tests were first conducted for different precursor-solvent combinations to identify their chemical stabilities at room temperature (**Table 2.2**). The precursor-solvent combinations of

2 Single droplet combustion and FSP synthesis of iron oxide nanoparticles

0.1, 0.25 and 0.5 mol/L FeNAP/p-Xylene, 0.1 mol/L FeNT/EtOH, and 0.1 mol/L FeNT/EtOH+EHA were selected for both single droplet combustion and FSP experiments.

Table 2.2: Dissolution tests of precursor-solvent combinations.

Precursor-solvent combination	Molar concentration, mol/L	Just after mixture	After 1 hour sonic wave vibration	Store at room temperature after 19 hours
FeNAP/p-Xylene	0.10	++	++	++
	0.25	++	++	++
	0.50	++	++	++
FeNT/EtOH	0.10	--	++	++
	0.25	--	--	--
	0.50	--	--	--
FeNT/EtOH+EHA	0.10	++	++	++

--: Not dissolved totally, solids exist. ++: Dissolved totally. EtOH+EHA means the mixture of ethanol and 2-ethylhexanoic acid with a volume ratio of 1:1.

Thermogravimetric analysis and differential thermal analysis (TGA-DTA, Netzsch STA 449 Jupiter) were employed to measure vaporization behaviors of the investigated precursors, solvents and precursor-solvent combinations. The liquid solution with a mass of ~50 mg was placed in an Al₂O₃ crucible (OD=6 mm, Height=7.5 mm, Waters GmbH, 864305.003). The measurements were carried out from 25 °C to 575 °C at an increased temperature rate of 7.5 °C/min as well as under the synthetic air at a flow rate of 50 mL/min.

2.2.2 Particle synthesis

Iron oxide particles were synthesized *via* FSP using the classical two-fluid nozzle [11], which was described in detail in **Chapter 1**. Therefore, only a brief introduction is given here. The precursor solution was fed to the nozzle at a liquid flow rate of 5 mL/min, and then dispersed into groups of small droplets by the pure oxygen at a gas flow rate of 5 L/min and a constant pressure droplet of 1.5 bar. The premixed methane and oxygen were at a gas flow rate of 1.5 L/min and 3.2 L/min,

respectively. Three mass flow controllers (Bronkhorst, EI-Flow) were used to control the gas flow rates. **Figure 2.1** shows photographs of the spray flames of the investigated solvents and precursor solutions in FSP experiments.

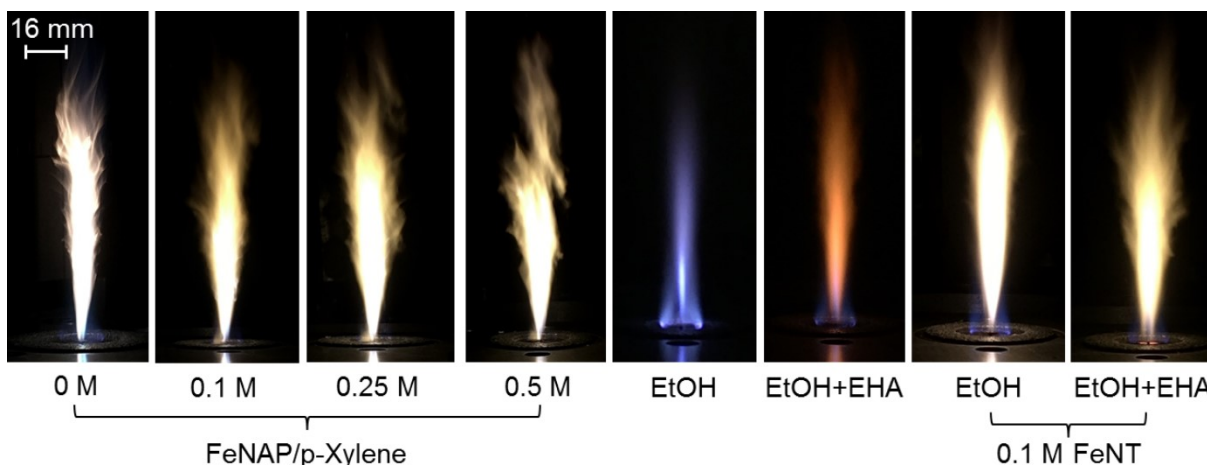


Figure 2.1: Photographs of the spray flames in FSP experiments of FeNAP/p-Xylene solutions with molar concentrations of 0, 0.1, 0.25, and 0.5 mol/L, EtOH, EtOH+EHA, 0.1 mol/L FeNT/EtOH, and 0.1 mol/L FeNT/EtOH+EHA. EtOH+EHA means the mixture of ethanol and 2-ethylhexanoic acid with a volume ratio of 1:1. These photographs were taken with reduced light intensity in the background. The lengths of these flames are in the range from 100 mm to 120 mm. The flame color of p-Xylene is white because of soot emissions. The flame color of ethanol is blue because no or less soot is produced. The flame color of the mixture of ethanol and EHA is orange owing to the low flame temperature, which is caused by the high heat of evaporation of EHA. The flame color of precursor solutions is yellow, indicating the presence of iron ions.

Figure 2.2 shows the sketch of the experimental setup for single droplet combustion experiments. The experiments were done under conditions of normal gravity, normal pressure and room temperature. Detailed descriptions of the experimental setup and procedure, and imaging processing will be shown in **Chapter 3**. Hereby only a brief introduction is given. After generation, the single isolate droplet moved upwards in the co-flowing oxygen atmosphere and was ignited

using the spark. The droplet combustion process was in-focus recorded *via* a high-speed camera with the help of a three-dimensional stage. The high-speed camera was in-line installed with a microscopy objective (Olympus SZ1145) in order to increase the lateral magnification, giving the recorded image a pixel size of $6.25 \mu\text{m}/\text{pixel}$. The particles synthesized *via* single droplet combustion were deposited on a carbon-coated copper grid (Plano GmbH-S162), which was placed above the flame top at a distance of 10 mm with a collection time of 30 minutes.

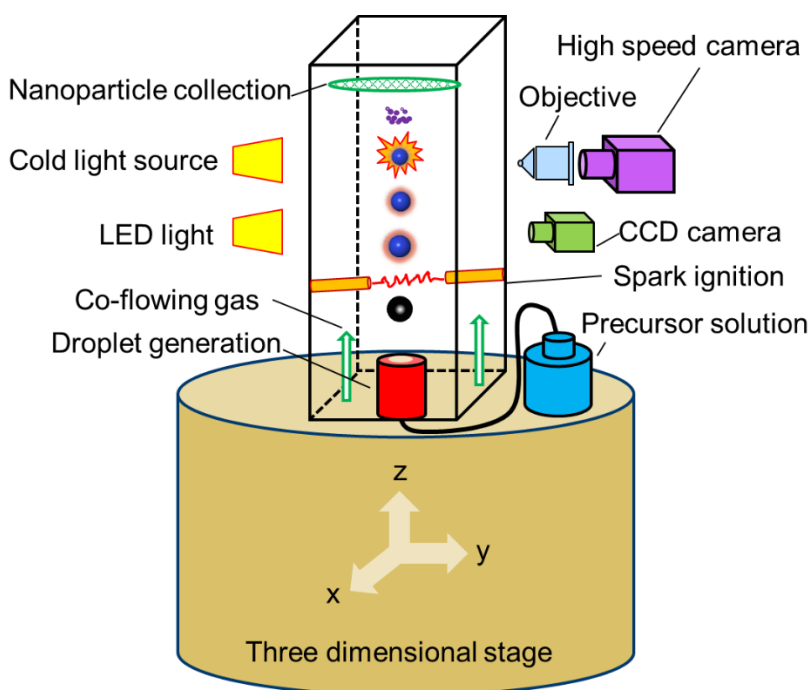


Figure 2.2: Sketch of the experimental setup for single droplet combustion.

2.2.3 Particle characterizations

Brunauer-Emmett-Teller (BET) measurements were conducted using a Quantachrome NOVA 4000e gas sorption system. The particles with a mass of $\sim 100 \text{ mg}$ were placed in a glass test cell. The prepared sample was pre-heated at $200 \text{ }^\circ\text{C}$ with degassing for ~ 2 hours in the flowing nitrogen atmosphere for cleaning the particle surface. In the following BET isotherm measurements, liquid nitrogen was adopted as the adsorbent at 77 K and at the relative pressure range (P/P_0) from 0.01 to 0.90, in order to quantify specific surface area (SSA) of iron oxide

nanoparticles prepared by FSP. Here, P and P_0 are the equilibrium and the saturation pressure of adsorbates at the temperature of adsorption, respectively.

X-ray diffraction (XRD) measurements were carried out using a PANalytical X'Pert MPD Pro system with Ni-filtered $\text{CuK}_{\alpha 1-\alpha 2}$ radiation. The diffraction patterns of iron oxide nanoparticles prepared by FSP were recorded by a PANalytical X'Celerator detector with 127 channels in the continuous scanning mode in the 2θ range from 10° to 100° with a step size of 0.0167° and a measurement time step of 200 s. A fixed divergence of $1/4^\circ$ was applied together with primary and secondary Soller slits of 0.04 rad and 0.0175 rad, in order to reduce the effects of over irradiation and asymmetry, respectively.

Low- and high-resolution transmission electron microscopy (TEM and HRTEM) images were obtained *via* a Titan 80-300 ST microscope (FEI™), which was equipped with a 300 keV electron beam. Carbon-coated copper grids (Plano GmbH, S162) were used as the support for particles synthesized by single droplet combustion and FSP. The FSP prepared particles were dispersed into ethanol. Two or three drops of the solution were placed on the grid, and dried at ambient conditions.

2.2.4 Rainbow refractometry

Rainbow refractometry was applied to record rainbow scattering patterns from single droplet combustion. **Figure 2.3** shows sketch of the experimental setup for rainbow refractometry. One laser beam (Opus 3W-532 nm, 2 mm in diameter) was expanded by the lens system into a light sheet with a shape of an elongated ellipse (20 mm in length and 2 mm in width), which illuminated on the burning droplet. The rainbow scattering patterns were recorded using one compact monochrome line scan CCD camera (DALSA Spyder3) at a frequency of 67 kHz. The camera utilized a single line of sensor pixels to build up a out-of-focus image. One Fourier-transforming lens was mounted in the front of the camera to focus objects from infinity with a focal length of

6.56 ± 0.25 mm. The recorded images have a pixel resolution of 1024 X 1024 with a spatial resolution of 96 pixels/inch.

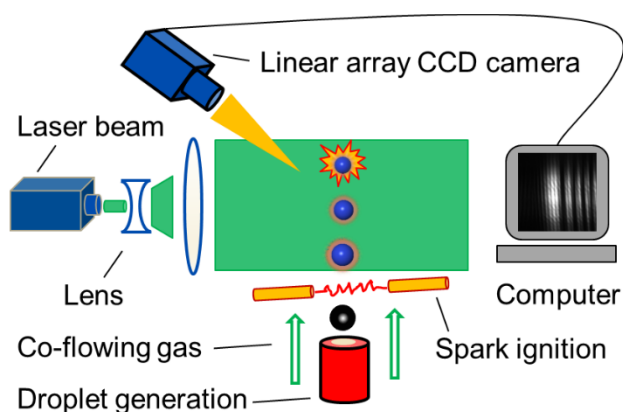


Figure 2.3: Sketch of the experimental setup for rainbow refractometry.

2.3 Results and discussion

This section presents the results and discussion into four subsections.

- (1) Single droplet combustion behaviors of metal organic precursor (**Subchapter 2.3.1**).
- (2) Single droplet combustion behaviors of metal inorganic precursor (**Subchapter 2.3.2**).

The first two subsections aim to determine the mechanism and occurrence conditions of droplet micro-explosions, as well as to trigger explosions of droplets containing metal nitrates.

- (3) Rainbow refractometry measurements of single droplet combustion (**Subchapter 2.3.3**).

The rainbow signals of single droplet combustion with/without explosions are compared and analyzed in order to provide evidences for supporting the proposed droplet micro-explosion mechanism.

- (4) TEM measurements and particle size comparison between single droplet combustion and FSP (**Subchapter 2.3.4**). The feasibility of using single droplet combustion experiments to predict nanoparticle quality for FSP is assessed.

2.3.1 Metal organic precursor: Iron (II) naphthenate

2.3.1.1 Single droplet combustion

Figure 2.4 shows the high-speed camera recorded frames of single droplet combustion of FeNAP/p-Xylene solutions with molar concentrations of 0, 0.1, 0.25 and 0.5 mol/L in the pure oxygen atmosphere. The initial droplet diameters and initial droplet velocities are $\sim 80 \mu\text{m}$ and $\sim 0.7 \text{ m/s}$, respectively. Single isolated p-Xylene droplet combusts steadily and its droplet diameter decreases with time until the end of combustion (**Figure 2.4 a**). The droplet combustion time of p-Xylene is $\sim 4.1 \text{ ms}$. Micro-explosions were observed after a short period of steady combustion for FeNAP/p-Xylene droplets (**Figure 2.4 b-d**). The time from ignition to the first micro-explosion decrease from 2.6, 2.0, to 1.1 ms with increasing precursor concentration from 0.1, 0.25 to 0.5 mol/L, respectively. The micro-explosions are continuous and multiple for the precursor solution droplet. For example, six continuous micro-explosions were detected during single droplet combustion of 0.25 mol/L FeNAP/p-Xylene (**Figure 2.5**). The first micro-explosion occurs at the relative time (the time after ignition) of 2.01 ms (milliseconds), and then the droplet surface explodes away, leaving the inner part of the parent droplet forming a new child droplet. The surface of the child droplet ejected away after a period of steady combustion (from 2.13 ms to 2.33 ms), indicating the occurrence of the second micro-explosion. In order to describe this kind of exploding combustion behaviors of droplet outer-layer, surface micro-explosion is proposed.

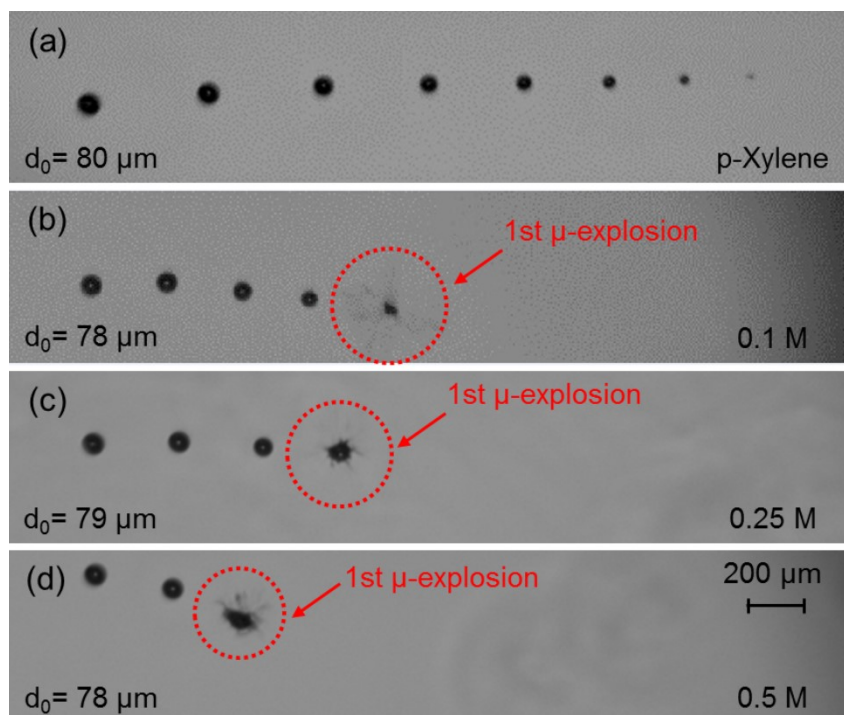


Figure 2.4: Merged image sequences of isolated burning droplets of FeNAP/p-Xylene solutions with molar concentrations of 0, 0.1, 0.25 and 0.5 mol/L. From left to right the droplets move in the upwards direction in the experiment. The initial droplet image is obtained from the high-speed camera recorded frame at the moment of ignition. In each merged image sequence, the time intervals between two continuous droplet positions are 0.581, 0.651, 0.674, and 0.616 ms. Here, d_0 represents the initial droplet diameter at the moment of ignition.

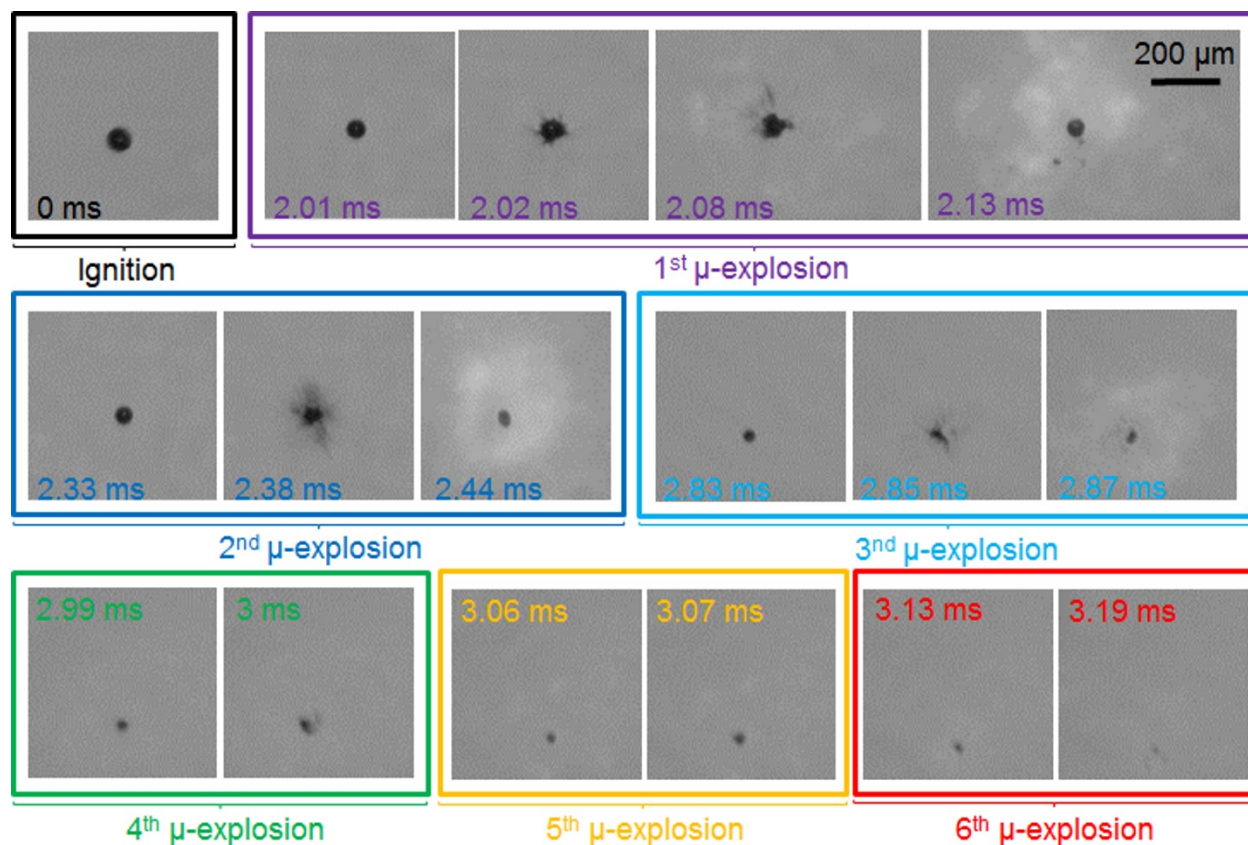


Figure 2.5: The high-speed camera recording image sequences of single droplet combustion of 0.25 mol/L FeNAP/p-Xylene. The time interval is measured from the moment of the droplet ignition. From left to right the droplet moves in the upward direction in the experiment.

The single droplet combustion experiments are highly reproducible, which is supported by the well-fitting of droplet diameter changes from ten groups of experiments (**Figure 2.6**). This is due to the stability of droplet generation and burning process. In order to avoid the influence of the differences of initial droplet diameters, the averaged value of droplet diameter changes of the ten reproducible droplets is squared and then normalized by the squared droplet initial diameter (**Figure 2.7**, top). A polynomial function of degree eight was applied to the normalized squared droplet diameter and then differentiated with respect to the normalized time, in order to calculate the droplet burning constant (**Figure 2.7**, bottom). This calculation is based on the classical spherical-symmetric diffusion-controlled combustion model, which is normally used to evaluate

the combustion behaviors of droplet in an oxidizing atmosphere [65, 66]. This droplet combustion model is also referred as the d^2 -law, *i.e.* the squared droplet diameter decreases linearly with time:

$$d_p^2 = d_0^2 - kt \quad (1)$$

where d_p , d_0 , k , and t represent the instant droplet diameter, initial droplet diameter, burning constant and time, respectively. The equation is then normalized by the initial droplet squared diameter:

$$\frac{d_p^2}{d_0^2} = 1 - k \frac{t}{d_0^2} \quad (2)$$

where $\frac{d_p^2}{d_0^2}$, and $\frac{t}{d_0^2}$ mean the normalized squared droplet diameter and the normalized time, respectively. Hereby, a constant value of burning constant is obtained when the normalized squared droplet diameter decreases linearly with the normalized time.

Depending on the burning constant, the single droplet combustion process can be classified into three consecutive periods: (1) The droplet heating and vapor accumulation. (2) The quasi-steady burning. (3) The burnout or explosion [37]. The instant of spark appearance is considered as the ignition moment in this work. The oxygen molecules in the spark channel are dissociated and ionized with a high plasma-electrical temperature. The energies of ionization and dissociation energy are transformed into thermal energy, rising up the gas temperature (could be around 6000 K) near the spark [67]. After ignition, the droplet needs time to absorb heat from the ambient as well as to evaporate the fuel from droplet surface to flame front. Thus, this kind of droplet heating and vapor accumulation results in one short period, where the burning constant increases, the droplet diameter barely decreases, and flame diameter increases. Then the droplet burns in a quasi-steady state, where the burning constant changes slightly and the droplet squared diameter decreases almost linearly with time (d^2 -law). In the burnout or explosion, the burning constant starts to drop dramatically and droplet diameter ceases to decline. Finally, the droplet stops burning or explodes. These three period characteristics are observed in the single droplet

combustion of of FeNAP/p-Xylene solutions with molar concentrations of 0, 0.1, 0.25 and 0.5 mol/L (**Figure 2.7**).

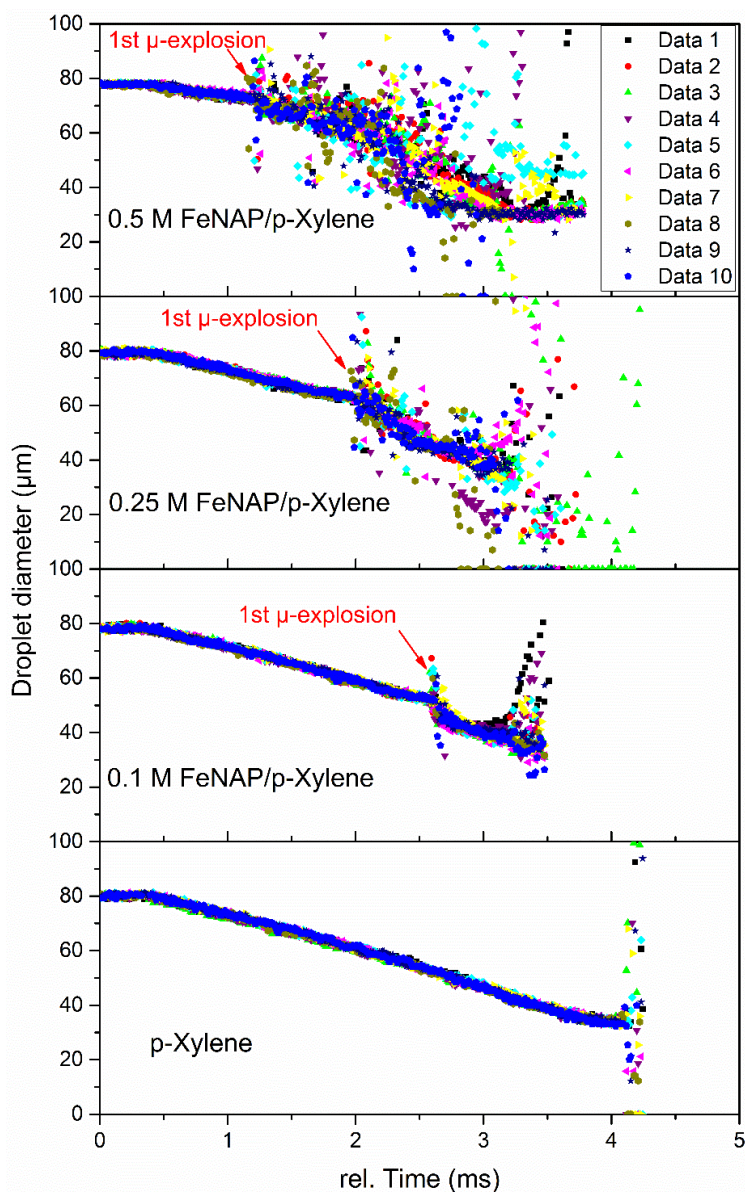


Figure 2.6: Droplet diameter changes of ten burning droplets for single droplet combustion of FeNAP/p-Xylene solutions with molar concentrations of 0, 0.1, 0.25 and 0.5 mol/L (from bottom to top). For each FeNAP/p-Xylene solution, all these ten droplets explode at the nearly same time.

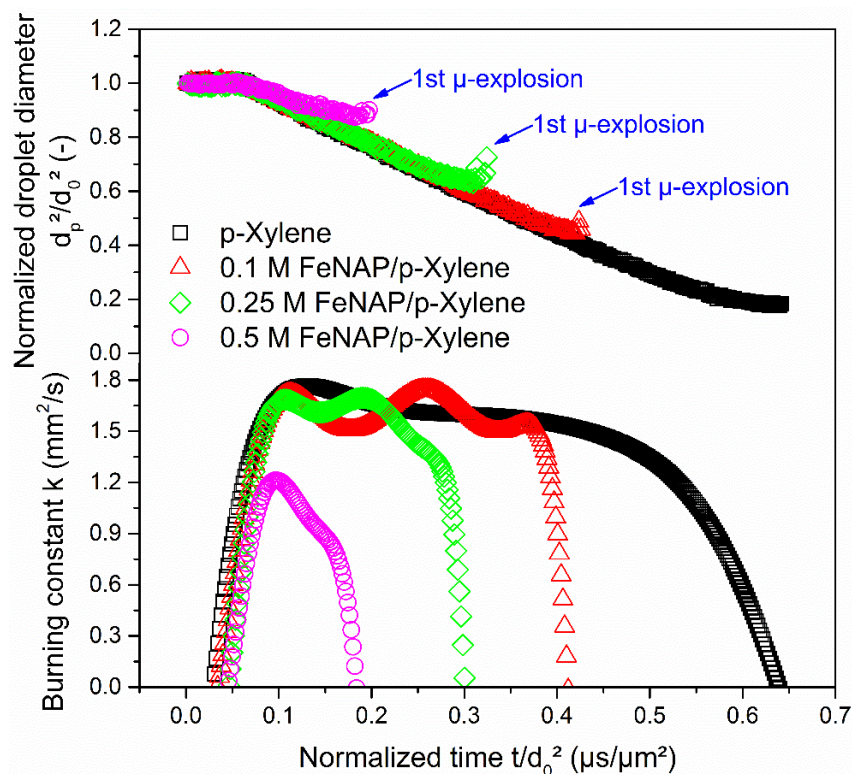


Figure 2.7: Changes of the normalized squared droplet diameter (top) and burning constant (bottom) for FeNAP/p-Xylene droplets. The ignition of the droplet corresponds to a normalized time equal to zero with a droplet diameter to d_0 . A polynomial function of degree eight was applied to the normalized squared droplet diameter and then differentiated with respect to the normalized time to calculate the droplet burning constant.

2.3.1.2 Micro-explosions during single droplet combustion

Disruptive droplet combustion (micro-explosions) is caused by the superheating and internal boiling of the high-volatility component trapped in the droplet, whose surface temperature is dominated by the low-volatility component [31]. Depending on the thermal decomposition of precursors, disruptive droplet combustion behaviors of precursor solutions are classified into puffing and droplet surface micro-explosion. The phenomenon of puffing is similar as that of water-in-oil emulsion droplet combustion, where water vapor is blown out from the droplet surface. Puffing takes place in droplet combustion of high-volatility precursors, which evaporate fast and

directly into gas phase. Thermal decompositions of precursors in liquid droplet are absent. One representative example is hexamethyldisiloxane (HMDSO) dissolved into xylene. Multiple droplet surface micro-explosions are observed during single droplet combustion of metal-organic precursors, which thermally decompose into multiple steps over a wide temperature range exceeding the limit of superheat of high-volatility solvents. Hereby the thermal decomposition temperature range (90 - 515 °C) of FeNAP exceeds the limit of superheat (306 °C) of p-xylene, which is supported by the thermogravimetric analysis and differential thermal analysis (TGA-DTA) in **Figure 2.8**. Consequently, multiple droplet surface micro-explosions occur during single droplet combustion of 0.25 mol/L FeNAP/p-Xylene (**Figure 2.5**). The outer layer of the parent droplet ejects away and combust strongly to form a large flame, leaving the inner part of the droplet to form a new child droplet, which continues to burn and explode. This experimental observation leads to the conceptual mechanism of shell formation and subsequent explosion.

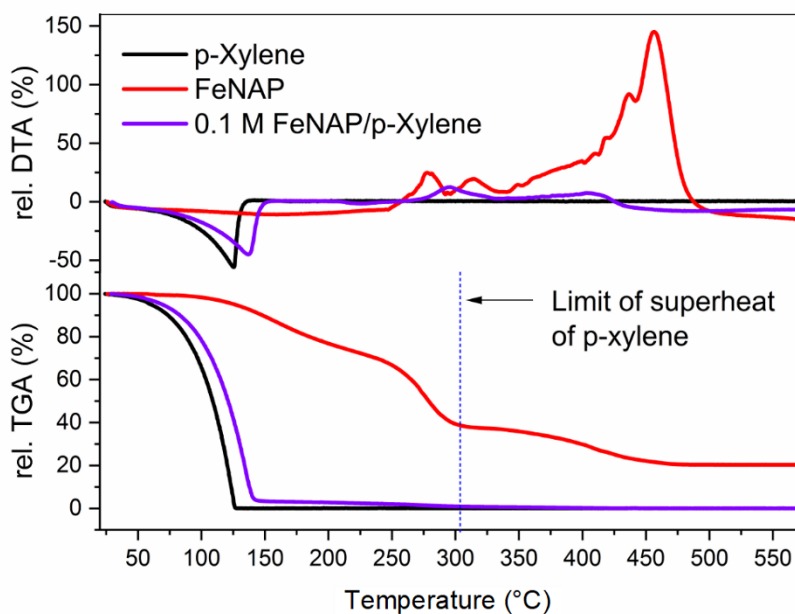


Figure 2.8: Thermogravimetric analysis (TGA) and differential thermal analysis (DTA) in the temperature range from 25 to 575°C for p-Xylene (black), FeNAP (red), and 0.1 mol/L FeNAP/p-Xylene. The measurements were performed at an increased temperature rate of 7.5 °C/min under a flow of 50 mL/min synthetic air.

Figure 2.9 shows the mechanism of droplet surface micro-explosions, which follows three steps: (1) diffusion-controlled combustion of the high-volatility component (d^2 -law, *i.e.*, the squared droplet diameter decreases linearly with time), and accumulation of the low-volatility component at the droplet surface, (2) thermal decomposition of the low-volatility precursor at the droplet surface and subsequent viscous shell formation, and (3) surface micro-explosion owing to the pressure build-up caused by the heterogeneous vapor nucleation of the high-volatility component beneath the shell [6, 28, 33]. Intermediates from precursor thermal decomposition, the undecomposed precursor and part of solvent at the droplet surface, are considered to participate in the formation of shell. The inner surface of the shell is assumed to supply sites for subsequent heterogeneous vapor nucleation [38]. Hereby heterogeneous instead of homogeneous vapor nucleation is proposed, which is based on the same occurring time of micro-explosions of precursor solutions (*i.g.*, ten 0.5 mol/L FeNAP/p-Xylene droplets in **Figure 2.6**). This reproducible explosive phenomenon is inconsistent with the stochastic nature of micro-explosions induced by homogeneous vapor nucleation, which follows random bubble nucleation and bubble expansion inside the superheated liquid due to density fluctuation [68].

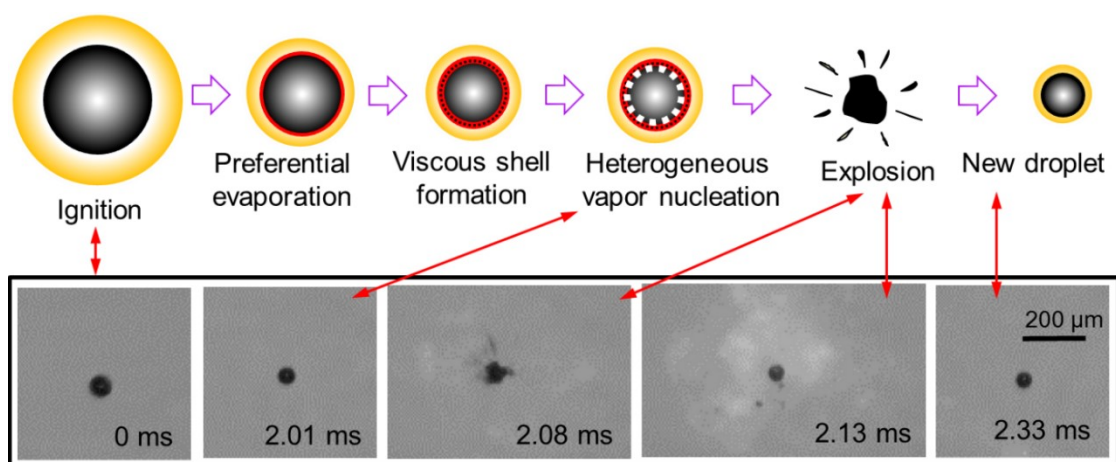


Figure 2.9: Surface micro-explosion mechanism of burning precursor/solvent droplet (top row), and the recorded images of the combustion process of 0.1 mol/L FeNAP/p-Xylene droplet *via* the

high-speed camera recording (bottom row). The time interval is measured from the moment of ignition. This figure is adapted and reprinted with the permission from Ref. [38].

The single droplet combustion of precursor solutions is considered as diffusion controlled or diffusion limited transport [32]. While the vapor is withdrawn from the droplet surface, the liquid phase mass diffusion rate is one to two orders slower than the droplet surface regression and the liquid phase thermal diffusion rate during combustion. Thus, the liquid element in the core of the burning droplet can be assumed to be trapped during most of the droplet lifetime [69]. Based on this assumption, the new formed child-droplet is considered to have the same composition as the initial droplet, and it continues to burn and explode with time. Increasing the precursor concentration accelerates the shell formation and droplet explosion (**Figure 2.4, 2.6 and 2.7**). Thus, the occurrence times of droplet surface micro-explosions are expected to become longer for the high precursor concentration solutions.

2.3.2 Metal inorganic precursor: Iron (III) nitrate nonahydrate

Figure 2.10 and **Figure 2.11** shows the high-speed camera recorded frames and the normalized squared droplet diameters, respectively, of single droplet combustion of EtOH, EtOH+EHA, 0.1 mol/L FeNT/EtOH, and 0.1 mol/L FeNT/EtOH+EHA in the pure oxygen atmosphere. After a period of steady combustion, single droplets of ethanol and 0.1 mol/L FeNT/EtOH cease to burn, leading to flame extinction and non-burning residuals (**Figure 2.10 a and c**). The transfer of water vapor from flame to droplet causes this incomplete combustion. Ethanol has a lower boiling point than water, and both liquids could completely mix with each other. The water vapor produced from flame could diffuse back to the ethanol droplet and condense into droplet, which result in flame extinction and residual formation of alcohol-based precursor-solvent droplets.

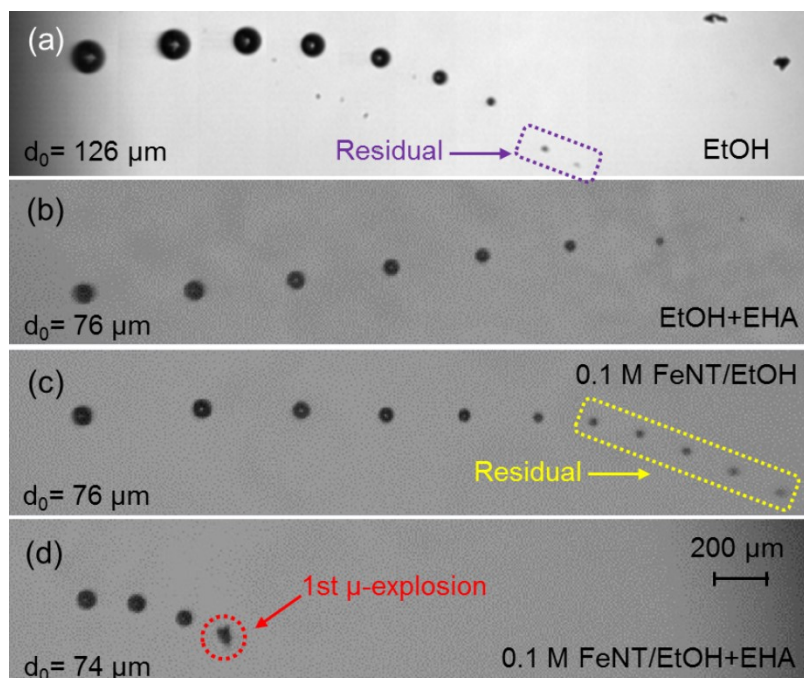


Figure 2.10: Merged image sequences of isolated burning droplets of (a) EtOH, (b) EtOH+EHA, (c) 0.1 mol/L FeNT/EtOH, and (d) 0.1 mol/L FeNT/EtOH+EHA. From left to right the droplets move in the upwards direction in the experiment. The initial droplet image is obtained from the high-speed camera recorded frame at the moment of ignition. In each merged image sequence, the time intervals between two continuous droplet positions are 1.350, 0.640, 0.663, and 0.663 ms. Here, d_0 represents the initial droplet diameter at the moment of ignition.

Mixing ethanol with EHA promotes the complete combustion of droplets (**Figure 2.10 b and Figure 2.11**). Pure ethanol and pure EHA evaporate completely up to their boiling points of 78 °C and 228 °C, respectively (Black and violet curves in **Figure 2.12**). The TG measurement of the mixture of ethanol and EHA shows a two-step process from 25 °C to 228 °C, where ethanol dominates the first step and EHA dominates the second step (Magenta curve in **Figure 2.12**). This two-step process occurs in ~26 minutes during the TG measurement. However, single droplet combustion of EtOH+EHA has a short life time of ~4.5 ms. Therefore, the evaporation of the mixture of ethanol and EHA at the droplet surface is fast dominated by the high boiling point EHA. As a result, the droplet surface temperature is enhanced above the boiling point of water,

which hinders the condensation of water vapor onto the droplet surface. However, the addition of EHA slows down the droplet burning constant compared to pure ethanol droplet (Green and black curves in **Figure 2.11**), which is caused by the larger heat of evaporation and the higher boiling point of EHA than ethanol (**Table 2.1**).

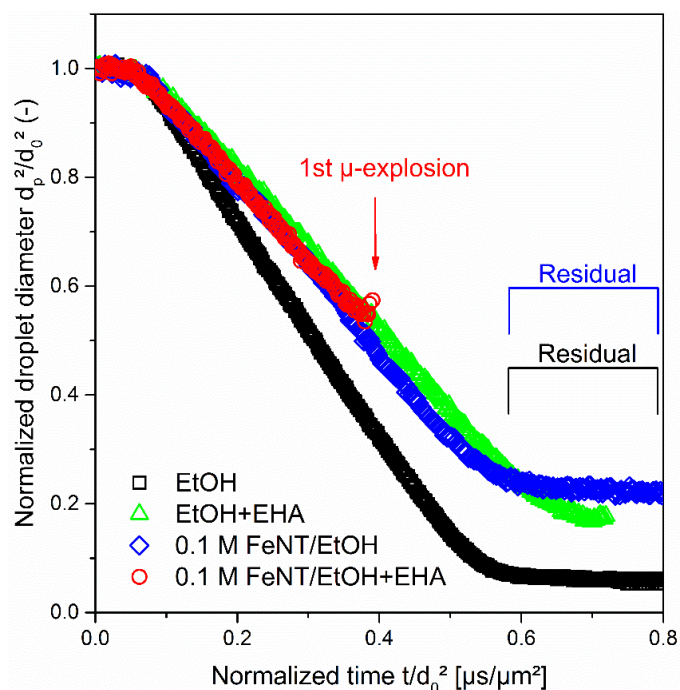


Figure 2.11: Changes of the normalized squared droplet diameter of EtOH (black square), EtOH+EHA (green triangle), 0.1 mol/L FeNT/EtOH (blue diamond) and 0.1 mol/L FeNT/EtOH+EHA (red circle). The ignition of the droplet corresponds to a normalized time equal to zero with a droplet diameter to d_0 . The normalized squared droplet diameters of ethanol and 0.1 mol/L FeNT/EtOH+EHA keep unchanging above $0.58 \mu\text{s}/\mu\text{m}^2$, which is caused by non-burning residuals (**Figure 2.10 a** and **c**).

Surface micro-explosion was observed during single droplet combustion of 0.1 mol/L FeNT/EtOH+EHA (**Figure 2.10 c**) but was absent during single droplet combustion of 0.1 mol/L FeNT/EtOH (**Figure 2.10 d**). The thermal decomposition temperature range of FeNT (Red curve in **Figure 2.12**) is below the limit of superheat ($214 \text{ }^\circ\text{C}$) of ethanol (Vertical dashed line in **Figure**

2.12). In addition, the evaporation process of 0.1 mol/L FeNT/EtOH is almost finished before reaching 100°C. Thus, micro-explosion is absent for burning droplets of 0.1 mol/L FeNT/EtOH. Different with FeNT and 0.1 mol/L FeNT/EtOH, the thermal decomposition of 0.1 mol/L FeNT/EtOH+EHA shows multiple steps over a wide temperature range exceeding the limit of superheat of ethanol. In addition, it is known that Fe(III) 2-ethylhexanoate has a thermal decomposition temperature range from 118.6 to 459.3°C [70]. Thus, the chemical reaction of EHA and iron nitrate to form iron carboxylate structure is proposed. This assumption is further supported by the presence of COO^- stretching bands of carboxylates using Fourier transform infrared spectroscopy (FTIR) measurements when EHA is added into iron nitrate based solutions [6, 8, 71].

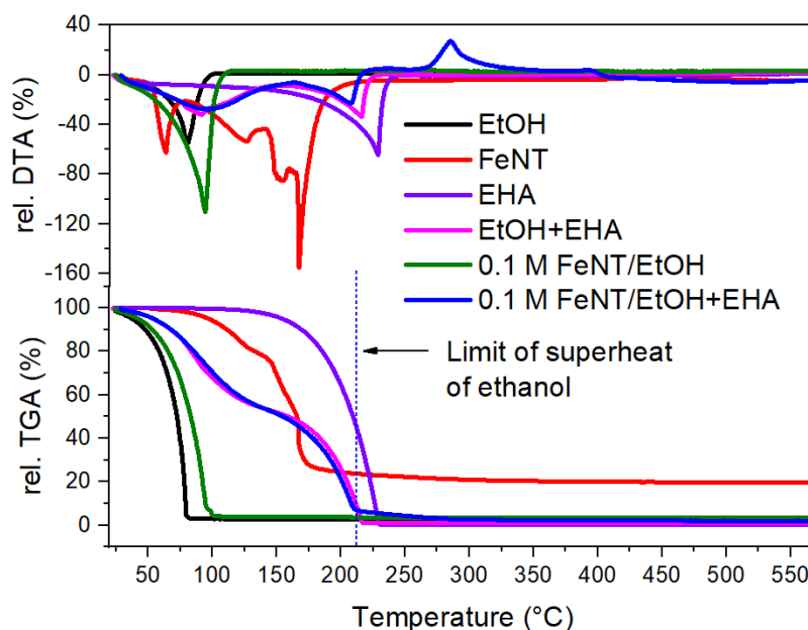


Figure 2.12: Thermogravimetric analysis (TGA) and differential thermal analysis (DTA) in the temperature range from 25 to 575°C for EtOH (black), FeNT (red), EHA (violet), EtOH+EHA (magenta), 0.1 mol/L FeNT/EtOH (olive), and 0.1 mol/L FeNT/EtOH+EHA (blue). The measurements were performed at an increased temperature rate of 7.5 °C/min under a flow of 50 mL/min synthetic air.

2.3.3 Rainbow refractometry measurements of single droplet combustion

The proposed shell formation mechanism in **Subchapter 2.3.1** can be supported by rainbow refractometry measurements. After ignition, the rainbow scattering patterns (rainbow scattering angles) of p-Xylene first increase and then decrease with time, which lasts for 3.2 ms (**Figure 2.13 a**). Rainbow scattering patterns of single component droplets are highly sensitive to refractive index inside the droplet, which is a function of temperature [29]. After ignition, while the surface temperature increases rapidly due to the fast heat transfer from the flame, the core temperature increases gradually because of the slow liquid-phase thermal diffusion (**Figure 2.14 e**). Thus, the temperature gradient causes an increasing refractive index gradient from the droplet surface to core, which changes the refraction paths of rainbow rays inside the droplet and results in the increase of rainbow scattering patterns (**Figure 2.14 c and Figure 2.15 a**). As droplets combust, the temperature gradient becomes weak because of the increase of the core temperature (**Figure 2.14 e**). As a result, the changed refraction paths resume to be straight, leading to the decrease of rainbow scattering patterns [29, 32] (**Figure 2.14 a and Figure 2.15 a**).

Different from single component droplets, the rainbow scattering patterns of precursor solution droplets exhibit two periods of increase and decrease (**Figure 2.13 b, c, and d**). The first period is caused by the temperature gradient after droplet ignition, which is similar to the single component droplet (**Figure 2.15 a**). The second period of increase and decrease of the rainbow angle was induced by the temperature gradient between the droplet surface and core, which is caused by the shell formation [30] (**Figure 2.14 d and f, and Figure 2.15 c**). The recoding time of this characteristic decrease from 2.3, 1.7, to 1.4 ms with the increasing iron precursor concentration from 0.1, 0.25, to 0.5 mol/L, respectively (**Figure 2.13 b, c, and d**). It indicates the early occurrence of droplet surface micro-explosions with increasing precursor concentrations.

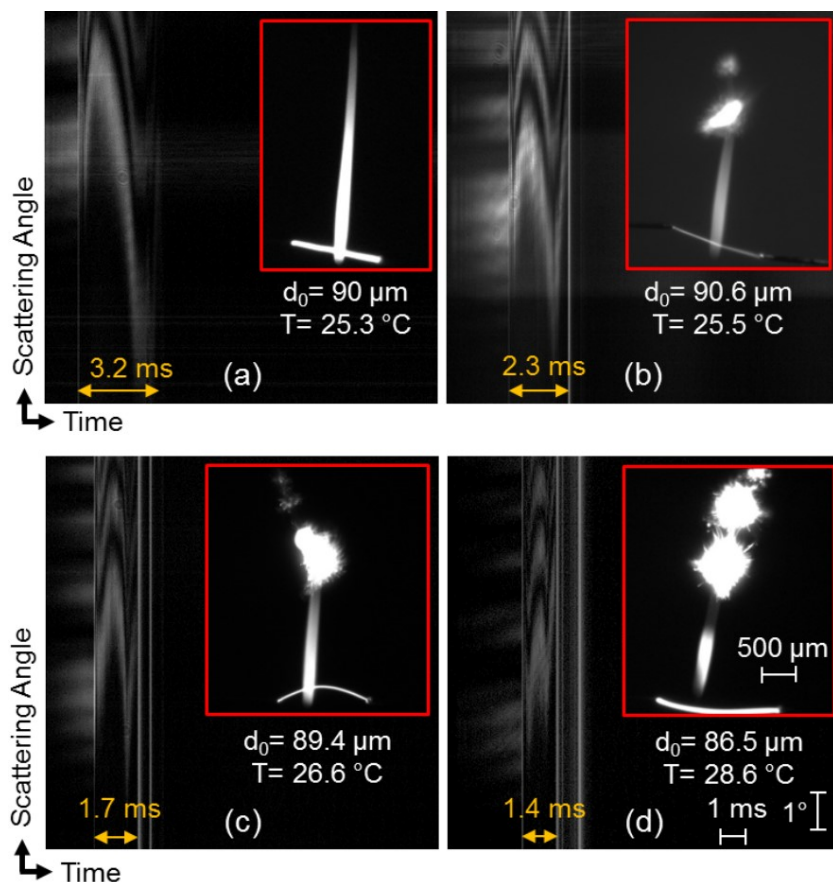


Figure 2.13: The recorded rainbow scattering patterns of single droplet combustion of p-Xylene (a), 0.1 (b), 0.25 (c) and 0.5 (d) mol/L FeNAP/p-Xylene. The vertical axis and the horizontal axis represent the scattering angle (totally 10.2°) and the time (totally 15.2 ms), respectively. The representative photograph of each single droplet flame is shown in each figure. These photographs are taken *via* a CCD camera with a low frame rate of 30 fps (frame per second). The recording time from droplet ignition to the 1st micro-explosion (marked with yellow arrows) reduces with the increasing precursor concentration. Here, d_0 and T represent the initial droplet diameter at the moment of ignition and the room temperature in the laboratory, respectively.

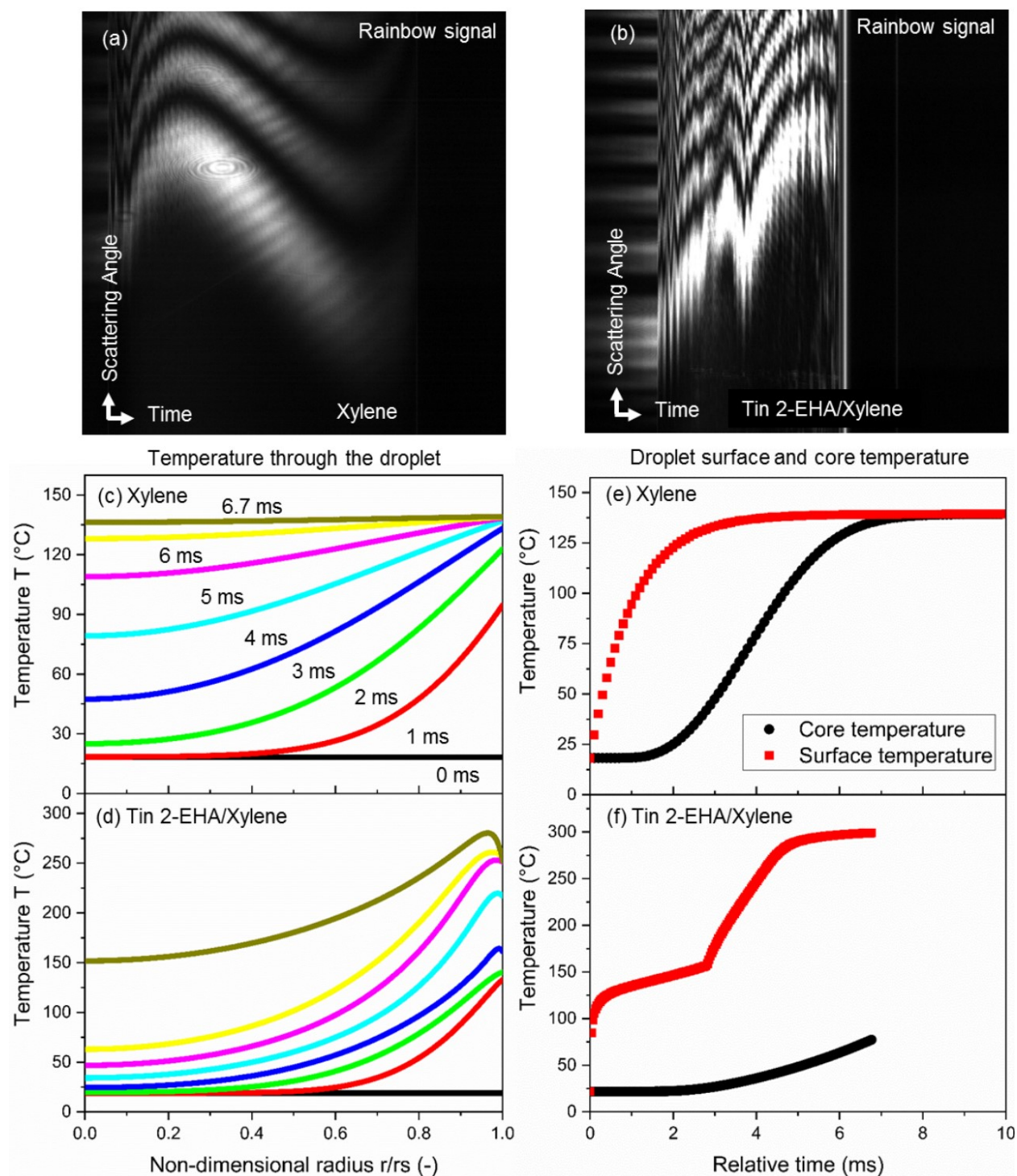


Figure 2.14: Rainbow signals of burning droplets of xylene (a) and 0.5 mol/L Tin (II) 2-ethylhexanoate dissolved in xylene (b). Simulated temperature gradients from the droplet core to surface (c) and (d). Simulated temperature changes of the droplet surface and core (e) and (f). The simulation is based on experimental rainbow signals of (a) and (b), and detailed modelling

can be found in the Ref. [30]. Figure (b) is adapted and reprinted with the permission from the Ref. [30].

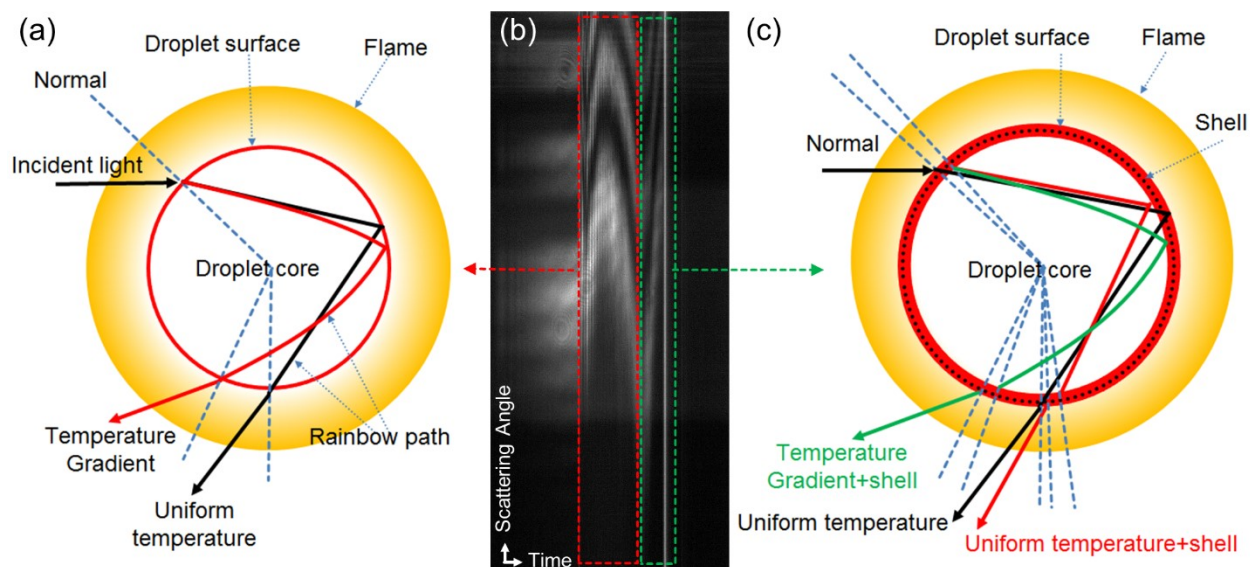


Figure 2.15: Rainbow signals of 0.1 mol/L FeNAP/p-Xylene droplet (b). The schematic of light rays to explain (a) the first period and (c) the second period of increase and decrease. The comparison of the optical light rays in (c) suggests that the second increase and decrease part of the rainbow signal is caused by the temperature gradient, which is triggered by the shell formation. This figure is adapted and reprinted with the permission from the Ref. [30].

For single droplet combustion of ethanol and 0.1 mol/L FeNT/EtOH, the rainbow scattering patterns increase after ignition, then decrease with time, and finally increase again. The second period of increase is caused by the absorption of water into the alcohol-based precursor-solvent droplets. The absorbed water mainly exists at the droplet surface, and part of it would diffuse into the droplet center, forming a composite gradient from the droplet surface to core. Water has a lower refractive index than ethanol (water and ethanol have refractive indexes of 1.33252 and 1.35912 at 25°C, respectively), and the refractive index of ethanol-water mixture decreases with the amount of water [72]. Thus, an increasing refractive index gradient is formed from the droplet surface to core, resulting in the increase of rainbow scattering patterns. It is challenging to record

the droplet flames of ethanol and 0.1 mol/L FeNT/EtOH even without any background light (the representative photographs in **Figure 2.16 a and c**), because ethanol is considered as a non-sooting fuel at normal conditions [73]. On the contrary, droplet flames of EtOH+EHA and 0.1 mol/L FeNT/EtOH+EHA are bright, owing to the high mole ratio of carbon to hydrogen of EHA. Rainbow scattering patterns of EtOH+EHA droplet show one period of increase and decrease, and 0.1 mol/L FeNT/EtOH+EHA droplet express two periods of increase and decrease.

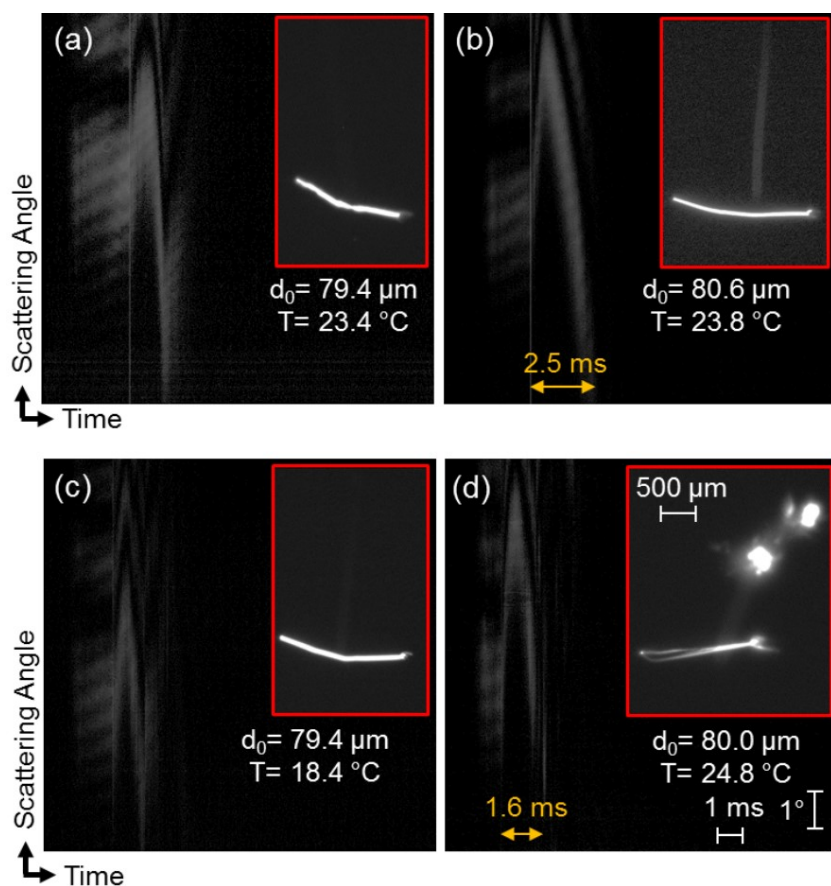


Figure 2.16: The recorded rainbow scattering patterns of single droplet combustion of (a) EtOH, (b) EtOH+EHA, (c) 0.1 mol/L FeNT/EtOH, and (d) 0.1 mol/L FeNT/EtOH+EHA. The vertical axis and the horizontal axis represent the scattering angle (totally 10.2°) and the time (totally 15.2 ms), respectively. The representative photograph of each single droplet flame is shown in each figure (The contrast of the photograph is improved in order to make the droplet flame more clearly in the

printed version.). The recording time from droplet ignition to the first micro-explosion (marked with yellow arrows) reduces with increasing precursor concentration.

2.3.4 TEM measurements and nanoparticle comparison

Agglomerated, spherical, and crystallite iron oxide nanoparticles were synthesized from single droplet combustion and FSP using the precursor solvent system of FeNAP/p-Xylene (**Figure 2.17**). The nanoparticles prepared from single droplet combustion and FSP have almost the same morphology (**Figure 2.17, first row**) and size distributions (**Figure 2.18**), when the same metal concentration is used. The mean particle size of flame-made particles increases from to 7.0, 9.4 to 13.7 nm with increasing of the iron precursor concentration from 0.1, 0.25 to 0.5 mol/L, respectively. Similarly, the mean particle size of droplet-made particles also increases from to 7.1, 10.1 to 12.8 nm with increasing of the iron precursor concentration. For the same precursor concentration, the mean particle size is almost the same for flame-made particles and droplet-made particles (**Figure 2.18**).

2 Single droplet combustion and FSP synthesis of iron oxide nanoparticles

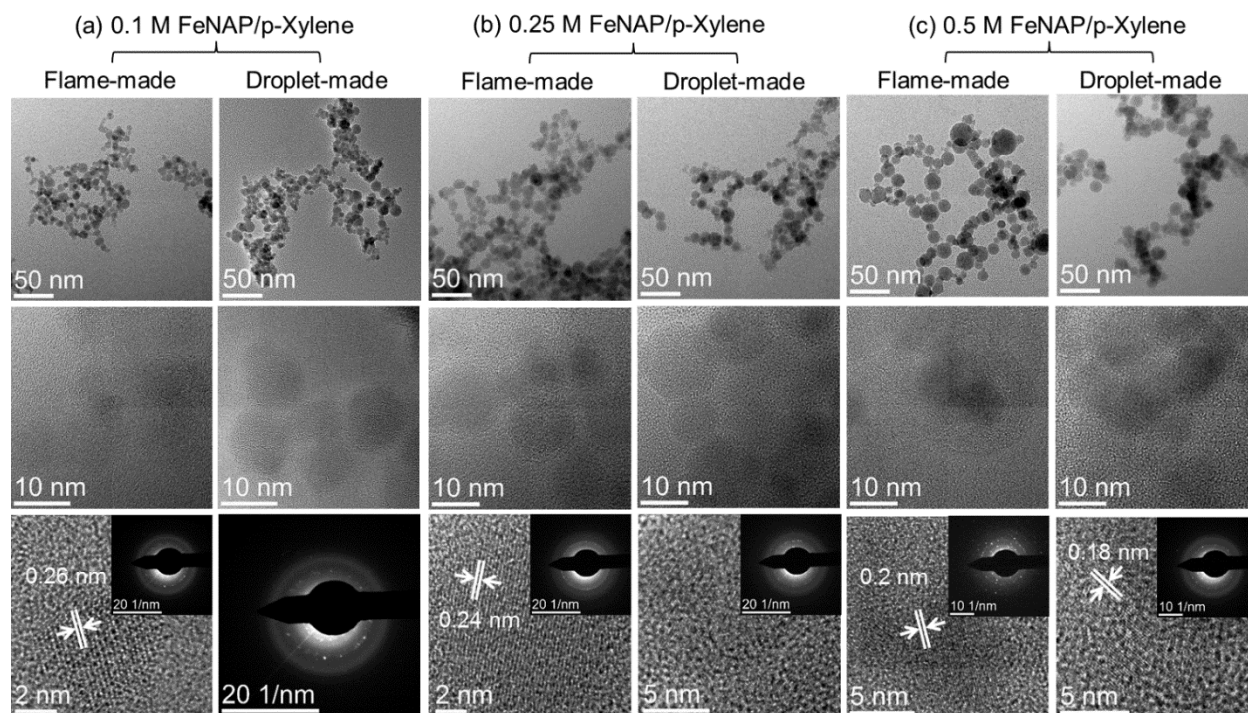


Figure 2.17: TEM images (first row), high resolution TEM (HRTEM) images (second row), and selected area electron diffractions (third row) of iron oxide particles obtained from FSP and single droplet combustion. The precursor solvent system is FeNAP/p-Xylene with a metal concentration of 0.1 (a), 0.25 (b), and 0.5 (c) mol/L. Selected area electron diffraction patterns showing ring structure.

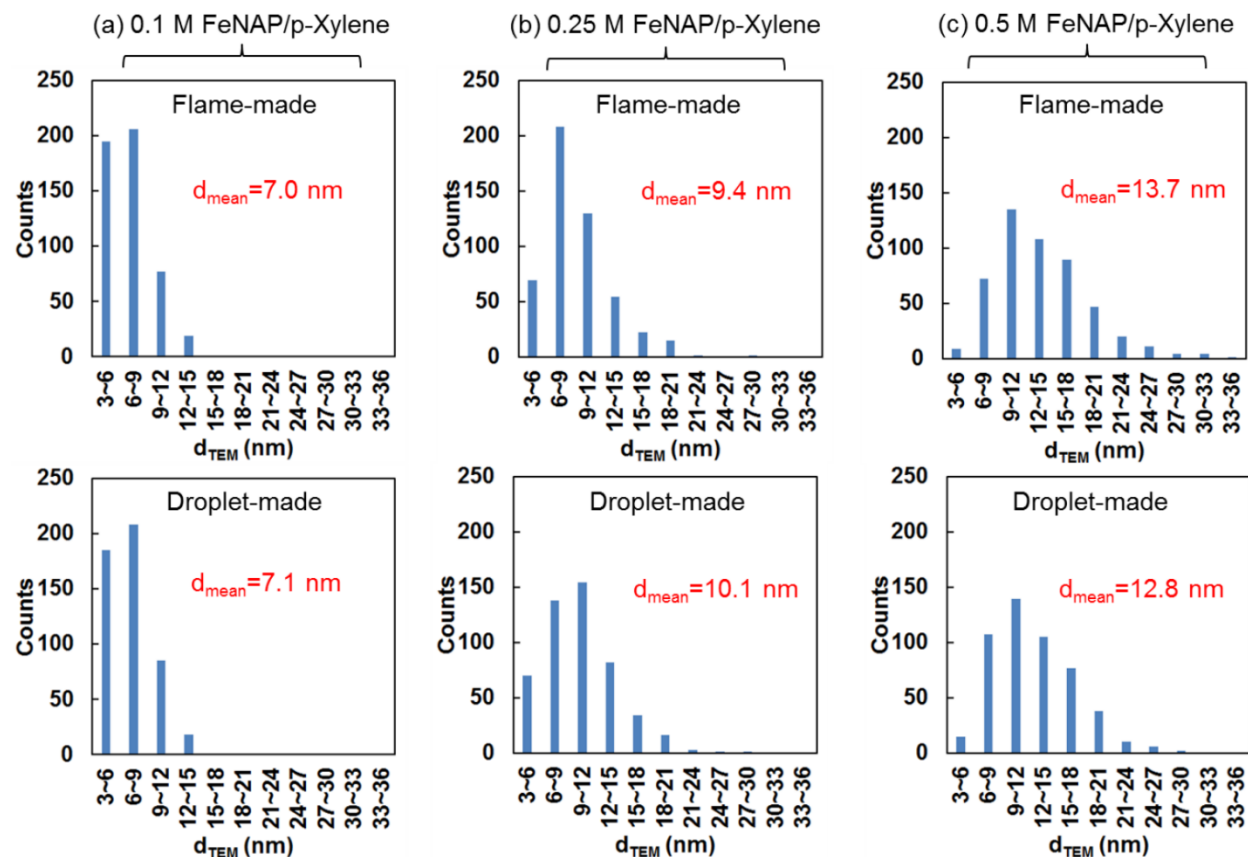


Figure 2.18: Particle size distributions of iron oxide particles obtained from FSP and single droplet combustion. The precursor solvent system is FeNAP/p-Xylene with a metal concentration of 0.1 (a), 0.25 (b), and 0.5 (c) mol/L. The mean particle size is almost the same for flame-made particles and droplet-made particles.

From single droplet combustion of 0.1 mol/L FeNT/EtOH, micro-size particles (**Figure 2.19 a**, the third column) are synthesized because of droplet-to-particle conversion, which is supported by the residuals at the end of droplet combustion (**Figure 2.10 c**). Moreover, small and homogeneous particles (**Figure 2.19 a**, the fourth column) are obtained as well, which are synthesized *via* the gas-to-particle conversion during the steadily droplet combustion. Using the mixture of 2-ethylhexanoic acid and ethanol (volume ratio as 1:1) as the solvent results in the formation of homogenous particles (**Figure 2.19 b**, the second column). Compared to pure ethanol, the addition of EHA slows down droplet combustion (**Figure 2.11**) because of its higher boiling point

and larger heat of evaporation while it has a larger heat of combustion (**Table 2.1**). However, the usage of 2-ethylhexanoic acid converts Iron nitrate into carboxylate complex, which induces droplet micro-explosions to achieve secondary atomization and to promote the homogeneous nanoparticle synthesis *via* gas-to-particle conversion [6, 33]. Therefore, three possible locations of particle formation during single droplet combustion of precursor-solvent combinations are summarized: (1) The steadily combustion periods, including the period from ignition to the first micro-explosion as well as the periods between two continuous micro-explosions. Here, the liquid precursor and its thermal decomposed intermediates absorb heat from flame, evaporate into vapors, and diffuse to the flame front. At the flame front, the fuel vapors undergo gas-phase thermal decomposition, and react with oxygen in the gas phase forming metal oxide vapors. Metal oxide vapors start nucleating in the colder flame regions owing to supersaturation, followed by particle growth (*via* coagulation and sintering), aggregation and agglomeration. Homogeneous particles are expected due to gas-to-particle conversion. (2) Residuals after flame extinction: inhomogeneous particles containing micro-size particles are expected from the droplet-to-particle conversion, where the low volatility precursors precipitate and decompose in the liquid phase. (3) Droplet micro-explosions: the secondary atomization of the solution and subsequent fast heat release from strong combustion result in the synthesis of homogeneous particles *via* gas-to-particle conversion. BET and XRD measurements of FSP synthesized iron oxide particles are shown in **Appendix A.2**.

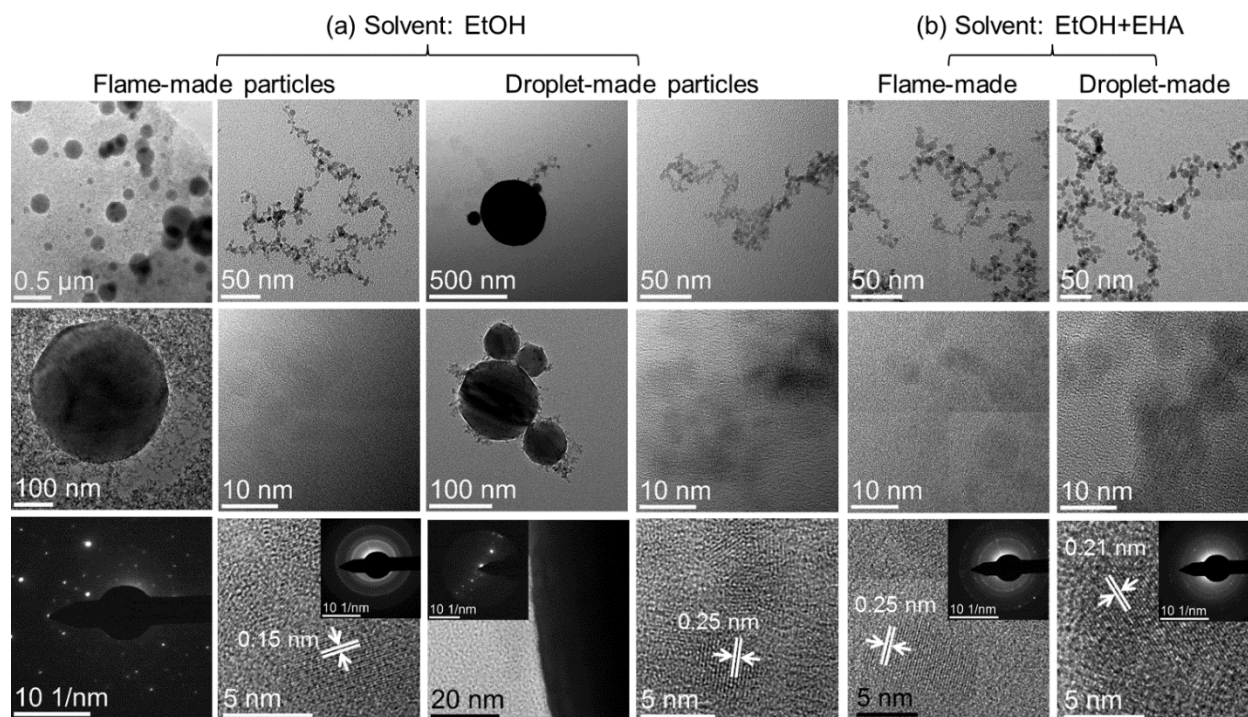


Figure 2.19: TEM images (first row), high resolution TEM (HRTEM) images (second row), and selected area electron diffractions (third row) of iron oxide particles obtained from FSP and single droplet combustion. The precursor solvent system is (a) 0.1 mol/L FeNT/EtOH, and (b) 0.1 mol/L FeNT/EtOH+EHA.

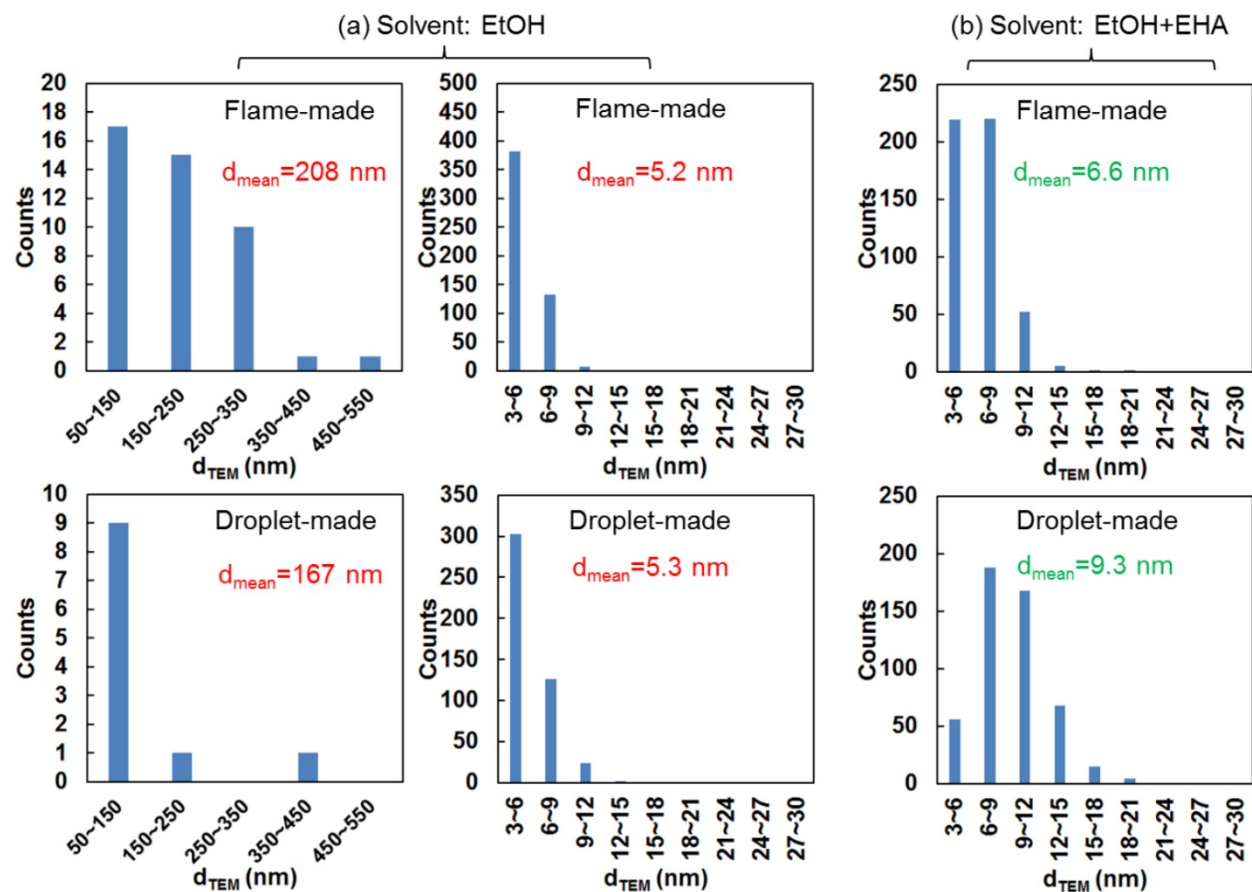


Figure 2.20: Particle size distributions of iron oxide particles obtained from FSP and single droplet combustion. The precursor solvent system is (a) 0.1 mol/L FeNT/EtOH, and (b) 0.1 mol/L FeNT/EtOH+EHA.

Iron oxide particles synthesized from single droplet combustion and FSP have shown similarity in size and morphology (**Figure 2.17, 2.18, 2.19 and 2.20**). In order to provide theoretical explanations, hereby simple monodisperse coagulation is used to estimate the changes in particle number concentration and particle size [74]:

$$d(t) = d_0 * (1 + N_0 * K_0 * t)^{\frac{1}{3}} \quad (3)$$

where $d(t)$, d_0 , N_0 , K_0 , and t are primary particle size, initial monomer size, original particle number concentration at time zero, coagulation coefficient, and particle residence time, respectively. The particle size ratio of FSP to single droplet combustion is expressed as:

$$\frac{d(t)_{FSP}}{d(t)_{SD}} = \left(\frac{1+N_{0_FSP}*K_0*t_{FSP}}{1+N_{0_SD}*K_0*t_{SD}} \right)^{\frac{1}{3}} \quad (4)$$

Here, K_0 is assumed to be a constant of $3.0*10^{-16}$ m³/s at standard conditions.

According to the investigation from FSP, the highest temperature of 2460 K was obtained at the height of 35 mm above the nozzle (**Figure 2.21 a**), where the residence time and primary particle size are 0.27 ms and 1.9 nm, respectively [75]. Nucleation and the onset of the particle growth take place right after the highest temperature. The increase in the primary particle size ceases at the height of 190 mm above the nozzle, indicating the completion of coagulation and sintering. At this distance, the related flame temperature and residence time are 1370 K and 8.4 ms, respectively. Therefore, the particle residence time in FSP is considered as ~ 8 ms. Even though the profiles of fuel, product, oxidizer and temperature from the droplet surface to the oxidizing atmosphere can be simulated (**Figure 2.21 b**) [21], the nanoparticle formation from the flame front is still a “black box”. Therefore, the particle residence time in single droplet combustion is assumed based on the first surface micro-explosion. During droplet surface micro-explosion, the particle residence time is considered as ~ 0.1 ms, which is determined by evaluating the combustion time of the ejected fragments during the first surface micro-explosion in the single droplet combustion of 0.25 mol/L FeNAP/p-Xylene (**Figure 2.5 and Figure 2.21 c**). The original particle number in the ejected fragment flame is assumed as the iron atom number difference between the droplet at spark ignition and the droplet after the first surface micro-explosion. The volume of the fragment flame is considered as the volume difference between fragment flame and the droplet after the 1st micro-explosion. Therefore, the original particle number concentration during droplet combustion is estimated. The original particle number concentration of FSP is around eighty times of that in single droplet combustion [75]. Thus, the particle size ratio of FSP to single droplet combustion is assessed as:

$$\frac{d(t)_{FSP}}{d(t)_{SD}} = \sim 1 \quad (5)$$

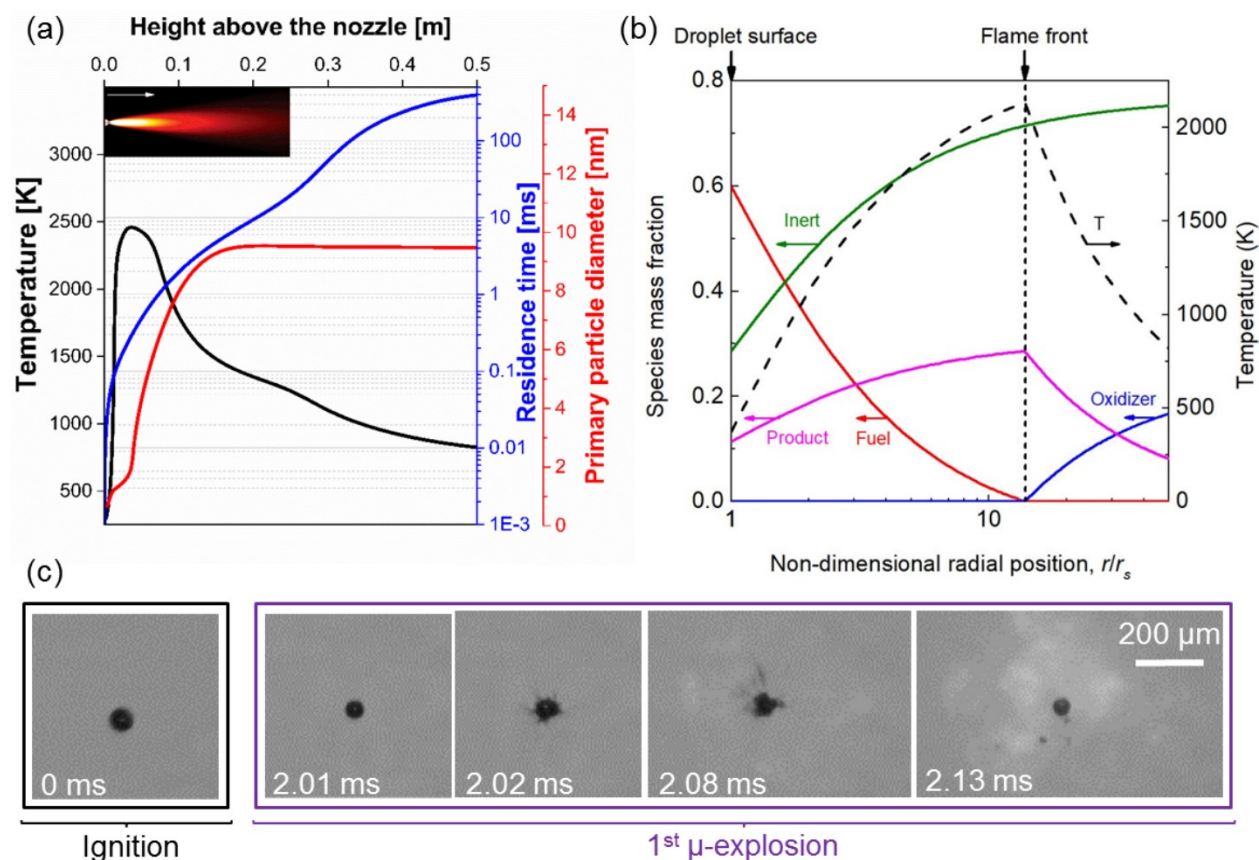


Figure 2.21: (a) Simulated temperature (black line), residence time (blue line) and primary particle diameter (red line) profiles along the centerline of the spray flame. One simulated flame image is shown in the left top to indicate the height above the nozzle in the flame. This figure is adopted with permission from the Ref. [75]. (b) Simulated temperature profile (black dashed line), mass fraction profiles of fuel (red line), product (pink line), and oxidizer (blue line) from the droplet surface to the surrounding during single droplet combustion of xylene with air. This figure is reprinted with permission from the Ref. [21]. Copyright (2021) American Chemical Society. (c) The high-speed camera recording image sequences of ignition and the first micro-explosion process in the single droplet combustion of 0.25 mol/L FeNAP/p-Xylene.

2.4 Summary and conclusions

2.4.1 Summary

- (1) The synthesis of iron oxide nanoparticles was experimentally performed using single droplet combustion and FSP techniques. Seven precursor-solvent combinations were tested to identify their chemical stabilities at room temperature. The single droplet combustion behaviors of five precursor-solvent combinations containing iron organic precursor and iron nitrate precursor were investigated using high-speed camera imaging technique and rainbow refractometry technique. Micro-explosions occur during single droplet combustion of precursor solutions using iron organic precursor instead of iron nitrate precursor. The conceptual mechanism was proposed to explain droplet micro-explosions, which can be supported by rainbow refractometry measurements.
- (2) The disruptive burning behavior (droplet micro-explosions) induces secondary-atomization of droplets, resulting in the acceleration of droplet evaporation and precursor release into the gas phase. As a result, the formation of homogeneous nanoparticles is promoted *via* the gas-to-particle conversion route. The usage of 2-ethylhexanoate acid converts low-volatility iron nitrate into high-volatility iron carboxylate, inducing droplet micro-explosions to promote the synthesis of homogeneous nanoparticles. The synthesized iron oxide particles from single droplet combustion and FSP were characterized using TEM, BET, and XRD measurements. The morphology and primary size of iron oxide particles from single droplet combustion and FSP were compared.

2.4.2 Conclusions

- (1) Droplet surface micro-explosions occur during single droplet combustion experiments of many FSP precursor solutions. The occurrence of multiple droplet surface micro-explosions depends on the following conditions: (i) Volatility/boiling point difference between the precursor and the solvent, which promotes the concentration of the low-

volatility precursor at droplet surface. (ii) Thermal decomposition of the precursor, which enhances the viscous shell formation. (iii) Limit of superheating of the high-volatility solvent, which is in the temperature range of thermal decomposition of the precursor.

- (2) Flame extinction and residual formation of alcohol-based precursor-solvent droplets result in the formation of inhomogeneous particles containing large and hollow powders at micro-scale. Adjusting the precursor-solvent system could induce disruptive droplet combustion of low-volatility metal nitrate precursors, enhancing the synthesis of homogeneous particles via FSP. It will be an economic alternative in industrial nanomaterial production by FSP, where the usage of organic precursors is estimated the largest cost factor.
- (3) Particles obtained from single droplet combustion and FSP were similar in size and crystalline state. It indicates that single droplet combustion experiments are able to predict the product quality, to interpret the cause of particle formation, and to seek solutions to improve the production of homogeneous nanoparticles in FSP.

3 Three-dimensional measurements of double droplet combustion^{II}

3.1 State of art

To understand the precursor mass transfer from liquid droplet to gas phase, it is important and necessary to study droplet evaporation and combustion in flame spray pyrolysis (FSP). While the gas-phase flame and nanoparticle synthesis have been *in-situ* analyzed with various optical diagnostics, the *in-situ* characterization of liquid droplets during FSP is mainly conducted by laser-sheet based Mie scattering and phase Doppler anemometry (PDA, also called phase Doppler interferometry) [3, 9]. Kilian *et al.* utilized laser-sheet based Mie scattering to gather the spatial droplet distribution in FSP synthesis of silica nanoparticles. They studied the spatial spreading of the nucleation zone as a function of precursor concentration [76]. Heine and Pratsinis applied PDA to *in-situ* measurements of the velocity profiles and size distributions of droplets during FSP synthesis of nanoparticles, and analyzed the effect of the initial droplet size on the evolution of the product particle size and polydispersity [77]. Gröhn *et al.* validated their computational model for zirconia nanoparticle synthesis with the PDA measured droplet velocity, size distribution and number concentration [78]. Stodt *et al.* studied the mean droplet size distributions and velocity profiles of burning and non-burning ethanol sprays using PDA measurements [24]. Aßmann *et al.* applied wide-angle light scattering technique to measure droplet sizes and their distributions in the spray flame [79]. Until now, the spatial droplet distribution, velocity profiles, number concentrations, and size distributions of droplets in FSP have been recognized. However, the *in-situ* temporal and spatial resolved measurements of evaporation and/or burning rates, lifetimes, composition changes, temperature changes and interactions of droplets in FSP are still lacking due to the severe experimental conditions.

^{II} The results presented in this chapter are partially published in the following manuscript: H. Li, N. Riefler, T. Wriedt, L. Mädler. Reference data set for three-dimensional measurements of double droplet combustion of p-xylene. Proceedings of the Combustion Institute. DOI: <https://doi.org/10.1016/j.proci.2020.06.297>.

Droplet interaction is an essential factor for studying droplet evaporation and combustion in the spray flame, because each droplet is influenced by immediately-neighboring droplets [80]. To classify interactive droplet investigations, William A. Sirignano has proposed three theory categories: spray, droplet group, and droplet array. (1) Spray theory takes into account the full coupling among the ambient gas and the local gas properties, and the droplet properties. A statistic or average representation of properties is made. (2) Group theory considers the gas conditions surrounding a cloud of droplets as given and proceeds to determine the local ambient conditions, droplet properties and vaporizations rates. A statistical description of droplet spacing is used. A representative example is the four group combustion modes proposed by Chiu and his coworkers [81, 82]. (3) Array theory adopts a well-defined geometry for a few droplets or a periodic configuration for a large number of droplets [80, 83]. In a spray, separating the influences of various parameters on the analysis of the phenomena is challenging due to the complicated droplet trajectories, dispersions in droplet sizes and velocities, and the non-uniform spatial distribution of the droplet number density [84]. As an alternative, droplet array has advantages to provide a precise geometrical description of droplet spacing and to demonstrate the functional relationship between droplet evaporation and the local ambient conditions [83]. Until now, many experimental investigations have been carried out on droplet array vaporization and combustion [80, 83, 85]. Miyasaka and Law found that buoyancy effect highly promotes the droplet evaporation rate to compensate for the interference effect during combustion of strongly interacting linear suspended droplet arrays [86]. Kato *et al.* experimentally investigated the flame spread phenomena in a suspended fuel droplet array in a high-pressure ambience, and illustrated that as droplet spacing becomes smaller flame spread rate increases and attains a maximum value at a specific spacing [87]. Shaw *et al.* indicated that droplet stream interactions affect soot generation and droplet disruption when investigating combustion characteristics of double droplet streams of methanol and methanol/dodecanol injected into hot gas environments [88]. Chen and Lin studied the variations of droplet combustion with the stream drop spacing using experiments

of droplet string of different initial spacing falling freely into a high temperature convection environment [85]. Yoshida *et al.* used microgravity experiments of droplet arrays placed at fiber intersections to investigate the flame-spread limit from interactive burning droplets, and indicated this value increases with the burning lifetime [89]. Wang *et al.* studied evaporation characteristics of single and multiple fuel droplets in a stagnant hot atmosphere using high-speed backlit image technique, and suggested that the evaporation interactions between droplets are significant at low temperature [90].

Droplet array tests using fiber suspended droplets and using freely flying droplets are two common ways to study droplet interactions. Both methods give information of the influence of local ambient conditions on droplet evaporations. For example, the critical droplet spacing (where the two separated flame fronts start to merge), the influence of ambient atmosphere (composition, pressure, and temperature), and the heat transfer between neighboring droplets. Differences exist between these two ways, which decide the application areas. For fiber suspended droplets, the heat conducted by the fiber need to be considered, and the fiber creates the difficulty to observe residual droplets. In addition, the suspended single droplets are non-spherical and have diameters of more than 1000 μm , which are larger than the real droplet sizes in spray combustion. However, the fiber suspended droplets have the advantage to investigate a large number of droplets (for example, flame-spread) due to the easy operation of the fiber system. Freely flying droplets have similar small sizes as the spray droplets, and their shapes are symmetric spherical due to the effect of surface tension. The high-speed camera imaging with microscope is able to observe the small residuals. Moreover, freely flying droplets are ideal for laser-based measurements, which are unsuitable to fiber suspended droplets because of the fiber and the droplet non-sphericity. Freely flying droplets are also ideal to study the collision between droplets [91]. However, the droplets are flying, and thus the information of droplet and flame are changing with time. Thus, it has a high requirement for the recording setups. Compared to fiber hanged or

suspended droplets, droplet streams can exclude the fiber influence, allowing the use of more optical diagnostics, including PDA, rainbow refractometry, fluorescence, and two-color laser-induced fluorescence (LIF). This is of great importance for providing adequate and accurate data to validate simulation and modelling of droplet interactions. Hereby, freely flying droplets are preferred to investigate double droplet combustion in the pure oxygen because it fits well to the application of studying the FSP process.

In this chapter, double droplet combustion experiments of pure solvent and precursor solutions are performed *via* an improved piezoelectric droplet-on-demand generator. For the first time, the three-dimensional (3D) measurement technique based on two highly time-synchronized high-speed cameras is developed in order to measure the process of double droplet combustion. The effects of droplet interactions, the oxidizing atmosphere, and the droplet composition on double droplet combustion behaviors are experimentally studied. In addition, it is known from **Chapter 2** that droplet micro-explosions occur in single droplet combustion experiments. In this chapter, the occurrence of droplet micro-explosions in double droplet experiments and the influence of droplet interactions on droplet micro-explosions are experimentally investigated as well.

3.2 Experimental setup and procedure

3.2.1 Setup construction

Figure 3.1 shows the sketch of the experimental setup for single and double droplet combustion. The setup mainly contains a glass reservoir, a droplet-on-demand generator, two electrodes, co-flowing oxygen, a CCD camera, a LED stroboscope, a cold LED light source with a gooseneck light guide, two high-speed cameras, and two objectives. The precursor solutions were stored in a glass reservoir, and fed to the droplet generator by a plastic pipe. The single or double droplets were generated from a piezoelectric droplet-on-demand generator [92, 93], and moved upwards in the co-flowing oxygen atmosphere in a glass cuvette (10 mm in length, 10 mm in width, and 40 mm in height). The gas flow rate of the pure oxygen (purity 99.95%) was controlled by a mass

flow controller (Bronkhorst, EL-Flow) to create a pure oxygen atmosphere (400 mL/min oxygen). The co-flowing atmosphere has a velocity of 0.067 m/s. The droplets were ignited by the electric spark discharge created by two tungsten electrodes (100 μm in diameter). The CCD camera and the LED stroboscope simultaneously capture the images of the generated droplets and ignited flames, in order to evaluate the conditions of droplet generation and flame formation. Highly reproducible and stable droplets and flames were required for droplet combustion experiments. The droplet combustion processes were *in-situ* recorded by the two high-speed cameras: one recorded the images of droplets with the backlight provided by the cold LED light source, and the other recorded the images of flames without any backlight.

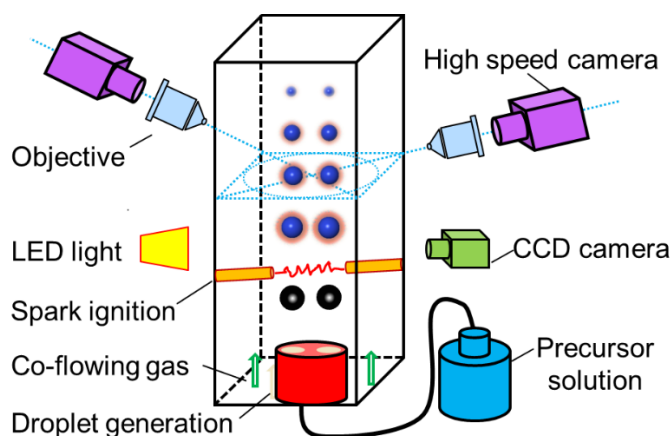


Figure 3.1: Sketch of the experimental setup for double-droplet combustion. The two high-speed cameras were horizontally installed at an angle of 90° .

Figure 3.2 a shows the piezoelectric droplet-on-demand generator, which mainly contains a titanium tube with two screw threads on each side, a piezo actuator (PIC 151, PI Ceramics) surrounding the middle part of the titanium tube, and a stainless steel nozzle plate (Micreon GmbH) installed in the top. The contraction of the piezo actuator accelerates the fluid in the titanium tube, leading to a pressure wave and the subsequent droplet ejection from the nozzle [94, 95]. The nozzle plate has a thickness of 200 μm and a diameter of 3.2 mm (**Figure 3.2 b**). The nozzle plate is flexible in installation and disassembly, and thus one generator can produce different kinds of

droplets using various types of nozzle plates. In this work, two nozzle plates were employed to generate single and double droplets, as shown in **Figure 3.2 c** and **d**, respectively. The ultra-short pulse laser for the purpose of single droplet generation (**Figure 3.2 c**) drilled one hole in the middle of the nozzle plate. Two holes with a defined center distance were drilled by the ultra-short pulse laser on behalf of double droplet generation (**Figure 3.2 d**). The droplet generation and spark ignition were conducted by a control software installed in a computer, an amplifier for the droplet driver electronic and the LED stroboscope driver, and an amplifier for the spark driver electronic [94]. The control software programmed with LabVIEW (National Instruments) generates output signals, which are transferred via RG-58 coaxial cables to the two amplifiers in order to control the droplet generation, the LED stroboscope imaging, and the spark ignition [94]. Detailed descriptions of the piezoelectric droplet-on-demand generator as well as the related experimental and simulated investigations can be found in Refs [92-95].

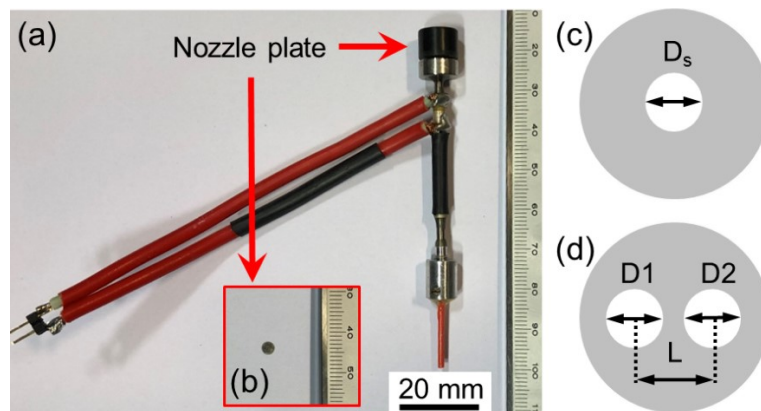


Figure 3.2: Photographs of the piezoelectric droplet-on-demand generator (a) and the nozzle plate (b). The sketches of nozzle plates for single-droplet generation (c) and double-droplet generation (d). The nozzle plate for single-droplet generation has a laser-drilled nozzle with a diameter of $D_s=75 \mu\text{m}$. The nozzle plate for double-droplet generation has two laser-drilled nozzles with diameters of $D_1=D_2=75 \mu\text{m}$, and a center distance of $L=125 \mu\text{m}$.

3 Three-dimensional measurements of double droplet combustion

Table 3.1 shows the two high-speed-camera recording system used in the present work. Two synchronized high-speed cameras (Phantom VEO 710L) were utilized to capture the images of droplets and flames. These two high-speed cameras were in-line installed with either a microscopy objective (Olympus SZ1145) or an objective (Mitutoyo 375-039), in order to increase the lateral magnifications. The two high-speed cameras were installed on two three-dimensional adjustment stages (**Figure 3.3 a** and **b**) in order to adjust the complete recording system in the right positions, where the droplet center was in the depth of field of objective (**Figure 3.3 c**). Therefore, both high-speed cameras record the in-focus images of droplets and flames.

Table 3.1: The two synchronized high-speed-camera recording systems used in the present work.

Two high-speed-camera recording system				
Camera and objective	Phantom VEO 710L + Olympus microscopy		Phantom VEO 710L + Mitutoyo objective	
Pixel resolution (pixel*pixel)	832*256	1024*256	832*256	1024*256
Pixel size ($\mu\text{m}/\text{pixel}$)	6.25		4.2	
Observe window (L*W, $\mu\text{m}*\mu\text{m}$)	5200*1600	6400*1600	3494.4*1075.2	4300.8*1075.2
Frame rate (frame per second, fps)	33000	28000	33.000	28000
Working distance (mm)	73		51	
Depth of focus (μm)	± 4.5		± 6.2	

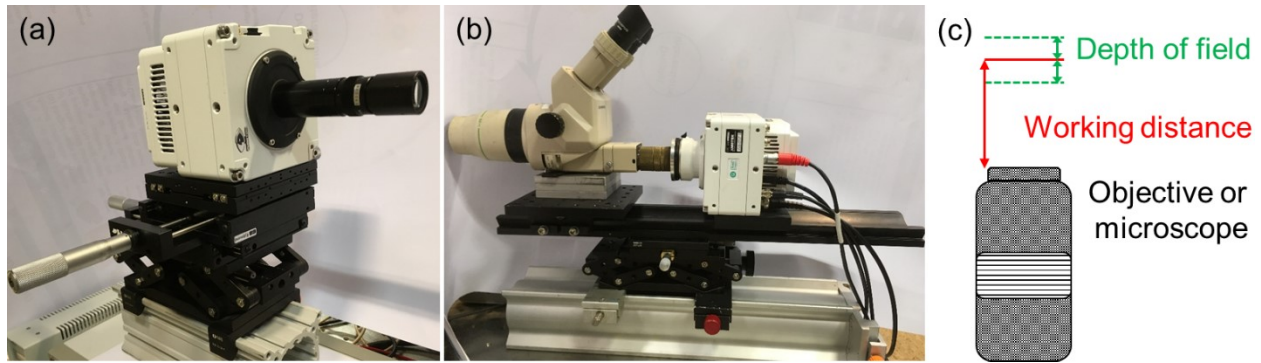


Figure 3.3: Photos of the two three-dimensional adjustment stages for (a) one high-speed camera (Phantom VEO 710L) with an objective (Mitutoyo 375-039) and (b) one high-speed camera (Phantom VEO 710L) with a microscopy objective (Olympus SZ1145). (c) Sketch showing the working distance and depth of field of objective.

3.2.2 Imaging processing

A Matlab script based on Canny edge detector were used to detect the boundaries of droplets and flames in the recorded images, as shown in **Figure 3.4 a** and **b**, respectively. The lateral magnification of the combinations of objectives and high-speed cameras (or the pixel size of the frames) were measured by taking an image of a glass ruler at the focus plane. For example, the distance of 238 pixels in **Figure 3.4 c** is equal to 1000 μm . Thus, the pixel size of the image recorded by the combination of objective and high-speed camera is 4.2 $\mu\text{m}/\text{pixel}$.

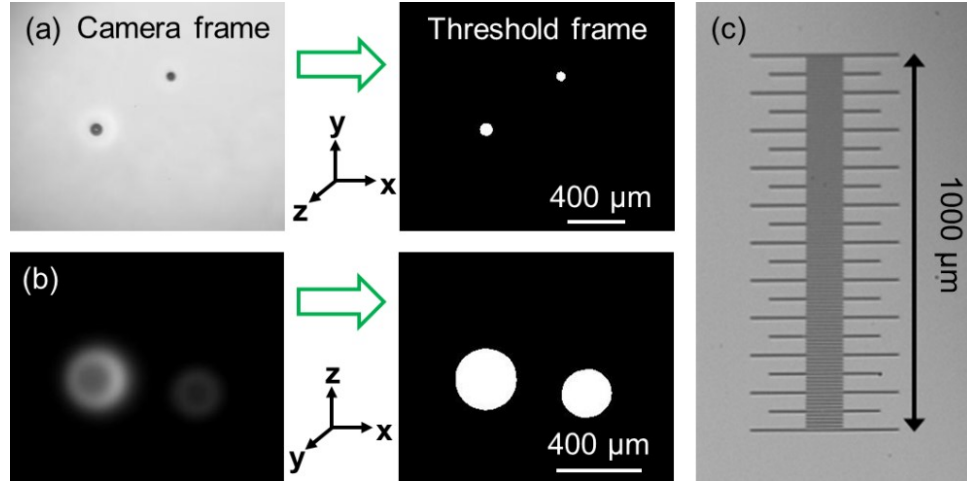


Figure 3.4: Image analysis of droplets (a) and flames (b) of a large and a small burning p-Xylene droplets using a Matlab script based on Canny edge detector. The droplet diameters of the large and the small burning p-Xylene droplets are 89 and 65 μm , respectively. The flame diameters of the large and the small burning p-Xylene droplets are 287 and 231 μm , respectively. The pixel size of the recorded images was measured by taking an image of a glass ruler at the focus plane of the combinations of objective and high-speed camera, as shown in the image (c).

The droplet 3D locations, droplet 3D velocities, droplet diameters, flame diameters, and the distance between centers of two droplets were obtained using another Matlab script (**Figure 3.5**). The droplet diameters were detected from x-axis and y-axis (e.g., D_{1x} , D_{1y}) via droplet frame. The flame diameters were obtained from three axis (e.g., F_{1x} , F_{1y} , F_{1z}) via both droplet frame and flame frame (right column in **Figure 3.5**), which are useful for detecting diameters of less spherical and overlapped flames. The mean value of the longest length in the x and y direction was taken as droplet diameter, e.g., $1st\ Droplet\ diameter = \frac{(D_{1x}+D_{1y})}{2}$. The mean value of the longest length in the x and z directions was taken as flame diameter, e.g., $1st\ flame\ diameter = \frac{(F_{1x}+F_{1z})}{2}$. The distance between the two droplet centers $[(x_1, y_1, z_1) \text{ and } (x_2, y_2, z_2)]$ was calculated using the equation, $L(t) = \sqrt{(x_1 - x_2)^2 + (y_1 - y_2)^2 + (z_1 - z_2)^2}$. The time-resolved 3D droplet velocity of

each droplet was figured out as the changes in 3D position over the time interval between two continuous frames.

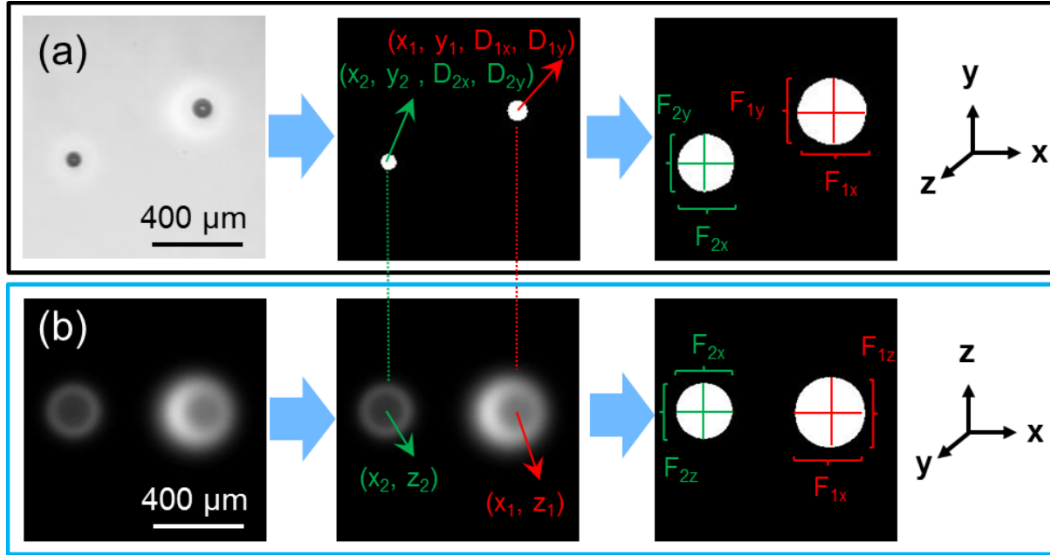


Figure 3.5: The schematics showing how to measure 3D locations (middle column), droplet diameters (middle column), and flame diameters (right column): (a) using droplet frame in the x-y plane, and (b) using flame frame in the x-z plane. The droplet center location and flame diameter in the x-axis of droplet frame are the same as these in the x-axis of flame frame.

3.2.3 Definitions of droplet spacing and flame spacing

During double droplet combustion, two droplets are burning and moving with time, which give rise to time-resolved information including trajectories, droplet diameters, and flame diameters. To describe these time-resolved information, droplet spacing $[S_D(t)]$ and flame spacing $[S_F(t)]$ are defined as a function of time (t):

$$S_D(t) = \frac{L(t)}{\left[\frac{D_1(t)}{2} + \frac{D_2(t)}{2}\right]} \quad (1)$$

$$S_F(t) = \frac{L(t)}{\left[\frac{F_1(t)}{2} + \frac{F_2(t)}{2}\right]} \quad (2)$$

where $L(t)$, $D_1(t)$, $D_2(t)$, $F_1(t)$, and $F_2(t)$, represent the separation distance between two droplet

centers, the first droplet diameter, the second droplet diameter, the first flame diameter, and the second flame diameter at the specific moment of t , respectively (**Figure 3.6**). Hereby, the first droplet is defined as the one that moved at a higher position at the instant of spark ignition.

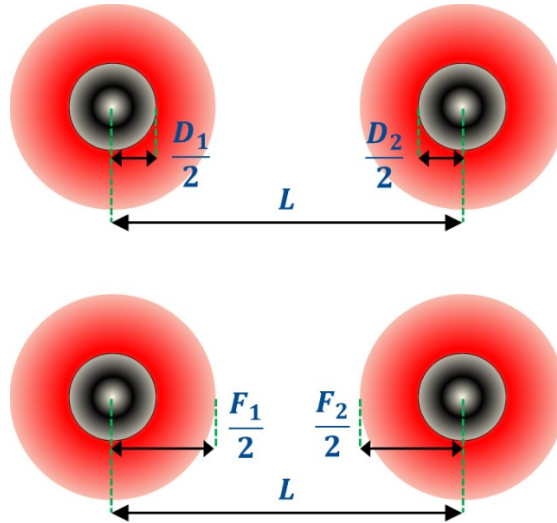


Figure 3.6: The schematics showing definitions of droplet spacing (top) and flame spacing (bottom). The two droplet surfaces begin to merge, when $S_D(t) = 1$. The two flame fronts (or flame sheets) start to merge, when $S_F(t) = 1$.

3.3 Results and discussion

This section introduces the results into four subsections based on the used solution and the droplet number:

- (1) Single droplet combustion of pure solvent in pure oxygen atmosphere (**Subchapter 3.3.1**).

The obtained data from single droplet combustion is used as a baseline for the comparison with double droplet combustion.

- (2) Double droplet combustion of pure solvent in pure oxygen atmosphere (**Subchapter 3.3.2**). The influences of droplet interactions on droplet combustion behaviors are studied in order to determine the critical values, below which droplet interaction occurs.

- (3) Double droplet combustion of pure solvent in the mixture of oxygen and nitrogen (**Subchapter 3.3.3**). The effects of oxidizing ambiances on droplet interactions, especially the occurrence of merged flames during double droplet combustion, are investigated.
- (4) Double droplet combustion of precursor solutions in pure oxygen atmosphere (**Subchapter 3.3.4**). The occurrence of micro-explosions during double droplet combustion and the influence of droplet interactions on droplet micro-explosions are studied.

3.3.1 Single droplet combustion of p-Xylene in pure oxygen atmosphere

In FSP experiments, pure oxygen is used to disperse the liquid precursor solution into micro-sized droplets, which burn initially in a pure oxygen ambience with subsequent air/product entrainment because of jet mixing [31]. Thus, droplet combustion experiments in pure oxygen ambience were carried out first. The influence of droplet interaction was reflected by the changes of single isolated droplet burning behaviors when neighboring droplet presented [85]. Therefore, the combustion characteristics of single droplet combustion were first investigated using two highly time-synchronized high-speed cameras, which would play a role as the reference for the comparison with the burning double droplets. The spark for droplet ignition appears at the same relative time of 0 ms in both droplet frame and flame frame, demonstrating the perfect time synchronization of the two high-speed camera recording system (**Figure 3.7**). The burning p-Xylene droplets are spherical due to the effect of surface tension. The droplet diameter decreases with time until the end of combustion, and this combustion process lasts ~6.4 ms. In this work, the visible (luminous) instead of infrared (nonluminous) flame radiation was recorded using the high-speed camera. The luminosity of the visible (luminous) flame radiation is mainly caused by the unburnt carbon particulates (soot) [96]. As a hydrocarbon fuel of high-soot tendency, p-Xylene has a benzene ring and a high mole ratio of carbon to hydrogen, giving rise to the formation of soot particle precursor and the increase of soot concentration in combustion, respectively [97, 98].

Consequently, the spherical flames of single isolated burning p-Xylene droplet are bright and visible despite under strong backlighting. The flame is almost invisible near the end of combustion due to the consumption of soot existing from droplet surface to flame front. The highly time-resolved 3D information of this single burning droplet were detected using the two time-synchronized high-speed digital cameras, and then visualized via 3D image (**Figure 3.8**).

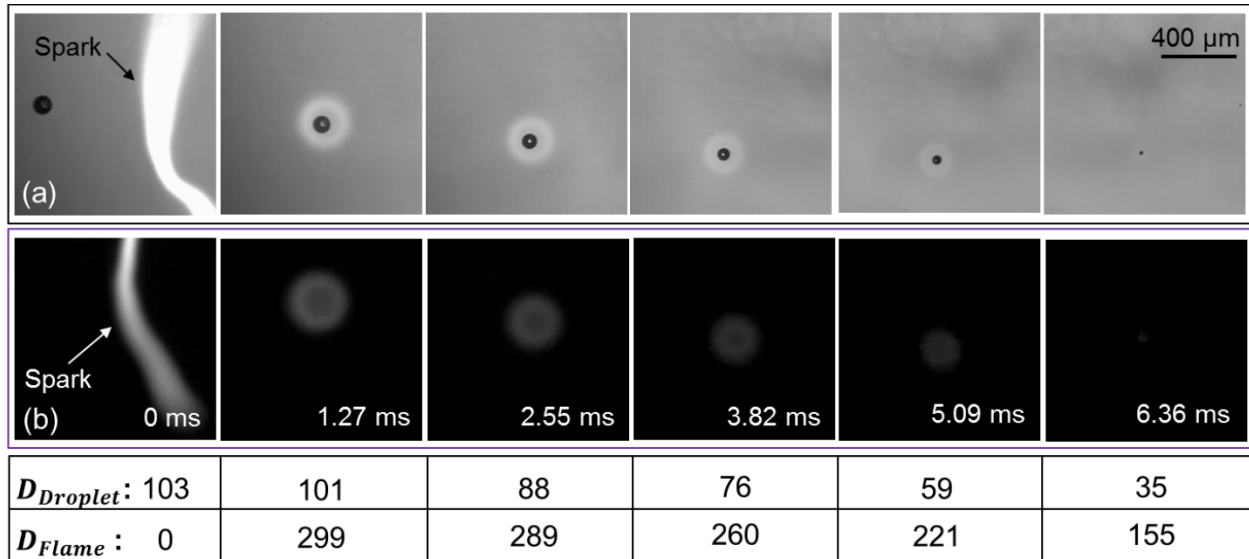


Figure 3.7: High-speed camera recorded (a) droplet frames in the x-y plane and (b) flame frames in the x-z plane of single droplet combustion of p-Xylene in pure oxygen atmosphere. The contrast of flame frames is improved in order to make flames more clearly in the printed version. The frames were recorded using the two time-synchronized high-speed cameras at a fast frame rate of 33000 fps. The droplets in the merged frames from left to right correspond to the upward movement in the experiment. Below each droplet frame the corresponding droplet diameter ($D_{Droplet}$, μm) and flame diameter (D_{Flame} , μm) are given. The time interval between two continuous frames is 1.27 ms, which corresponds to a frame interval of 42. The initial droplet diameter and initial droplet velocity are around 103 μm and 0.5 m/s, respectively.

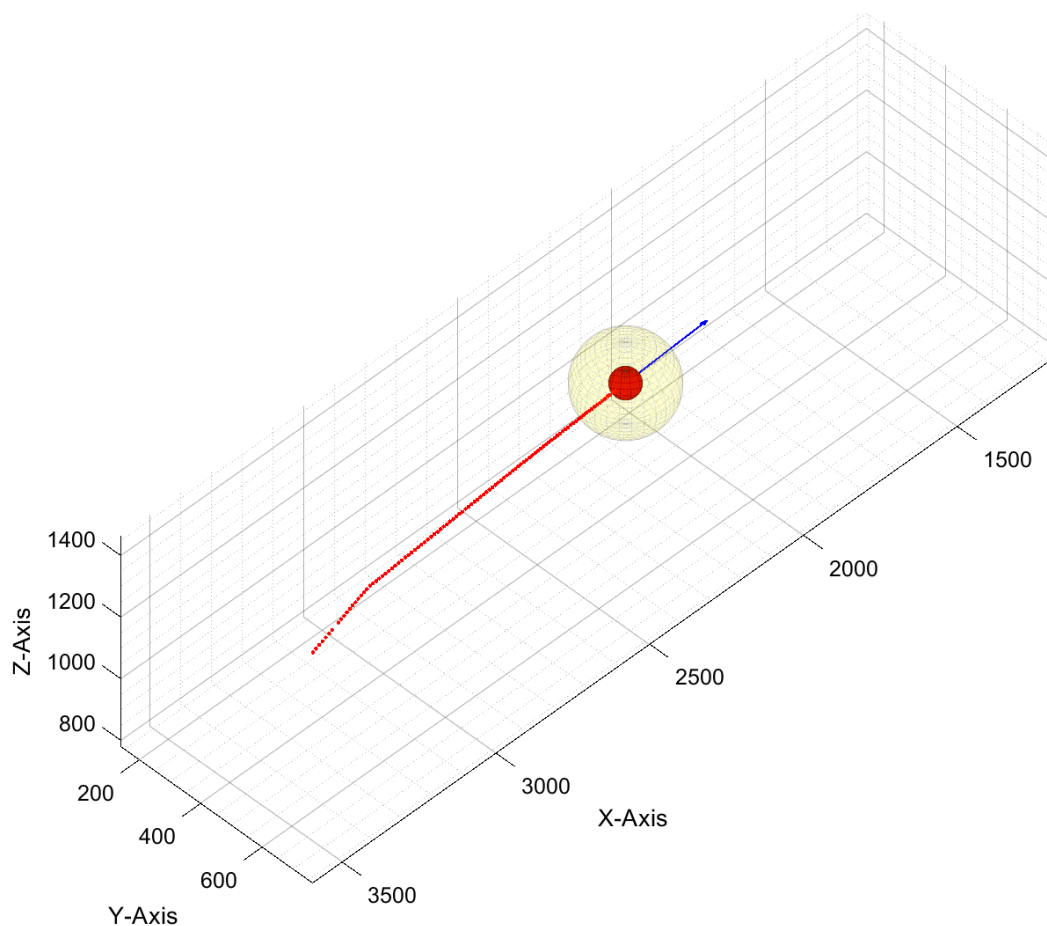


Figure 3.8: The visualized 3D image of the single burning p-Xylene droplet in Figure 3.7 at $t=2.55$ ms. Red solid sphere and red dotted line indicate the droplet and its 3D trajectory, respectively. Blue arrow and mesh sphere represent the 3D velocity and the flame, respectively.

The changes of droplet diameter and flame diameter were obtained from measurements of five highly reproducible p-Xylene droplets (**Figure 3.9 a and b**), which were averaged to get polynomial fitting curves (**Figure 3.9 c and d**). The flame diameter was detected with a delay of ~ 0.5 ms ($\sim 8\%$ of droplet combustion time) after spark ignition, demonstrating the heat transfer from spark to droplet surface, a sudden increase of droplet surface temperature, and the flame formation. During this droplet heating and vapor accumulation period, the heat from flame is mainly used to increase droplet temperature instead of evaporating the fuel at droplet surface. Thus, the droplet diameter decreases slowly from 0 to 0.7 ms (**Figure 3.9 c and d**). The

polynomial fitting curve of droplet diameter was normalized by the squared droplet initial diameter (Figure 3.9 e), and then used to gain the droplet burning constant (Figure 3.9 f). This information of single droplet combustion will be used as reference to compare with double droplet combustion.

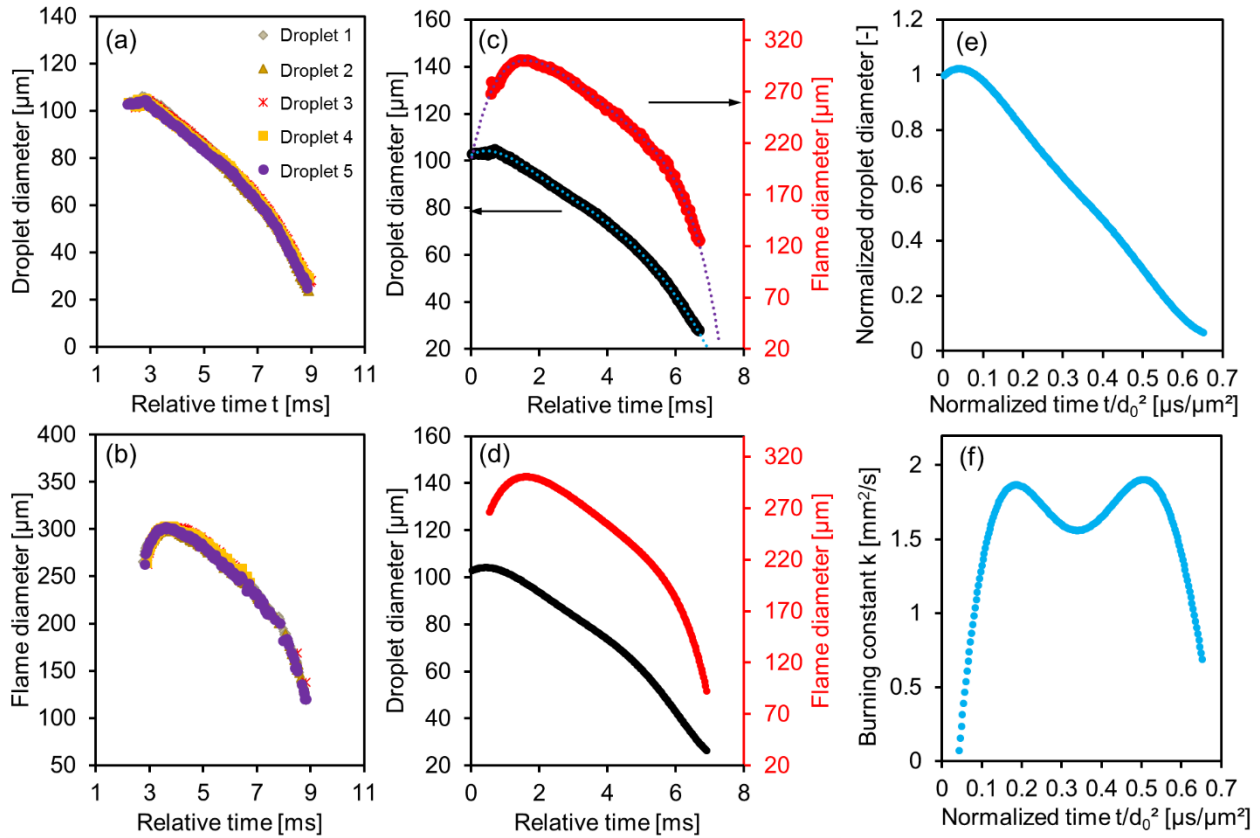


Figure 3.9: Measured data from five single isolated burning p-Xylene droplets: (a) droplet diameter, (b) flame diameter, (c) the mean droplet diameter (black curve) and the mean flame diameter (red curve), and their polynomial fitting curves (dotted lines), (d) the poly-fitting curves, (e) the normalized squared droplet diameter, and (f) the burning constant. The curves in (c), (d), (e), and (f) were shifted to set the moment of ignition to $t=0$ ms. The figure is adapted and reprinted with the permission from the Ref [39].

3.3.2 Double droplet combustion of p-Xylene in pure oxygen atmosphere

During double droplet combustion, the minimum value of flame spacing [$Min(S_F)$] demonstrates the nearest distance between the two flame fronts. Thus, this value was exploited as the criteria to classify the interaction between two burning droplets. Hereby two cases of double droplet combustion experiments in pure oxygen atmosphere are shown: the weak interaction case [$Min(S_F) = 1.7$] and the strong interaction case [$Min(S_F) = 1.2$].

For the weak interaction case [$Min(S_F) = 1.7$], the first droplet has a larger flame diameter than the second droplet due to its larger initial droplet diameter (**Figure 3.10**, $t = 0.89$ ms). When the two burning droplets are close, the first flame exhibits strong brightness (**Figure 3.10 b**, at $t = 1.75$ ms and $t = 2.6$ ms), indicating the interactions during double droplet combustion. While the second droplet shows comparable changes of droplet diameter and flame diameter to single droplet combustion, the first droplet shows a slow droplet diameter regression from 1.2 to 2.4 ms (**Figure 3.11 c**). The droplet spacing increases steadily from 5.2 to 24.2 with respect to the relative time from 0 to 6.4 ms. The flame spacing first drops suddenly, then decreases slowly from 2.2 to 1.7, and further increases continuously to 6.3 (**Figure 3.11 d**). The large values of the initial flame spacing were caused by the short-time ignition delay existing between two flame formations, where only the first flame diameters were considered to calculate the flame spacing from 0.5 to 0.57 ms. The minimum value of flame spacing was obtained at the relative time of 1.75 ms, where the first flame has the largest diameter and the second flame diameter just passes the largest value (the red vertical line dashed in **Figure 3.11 d**). The obtained 3D information were visualized as 3D image as shown in **Figure 3.12**.

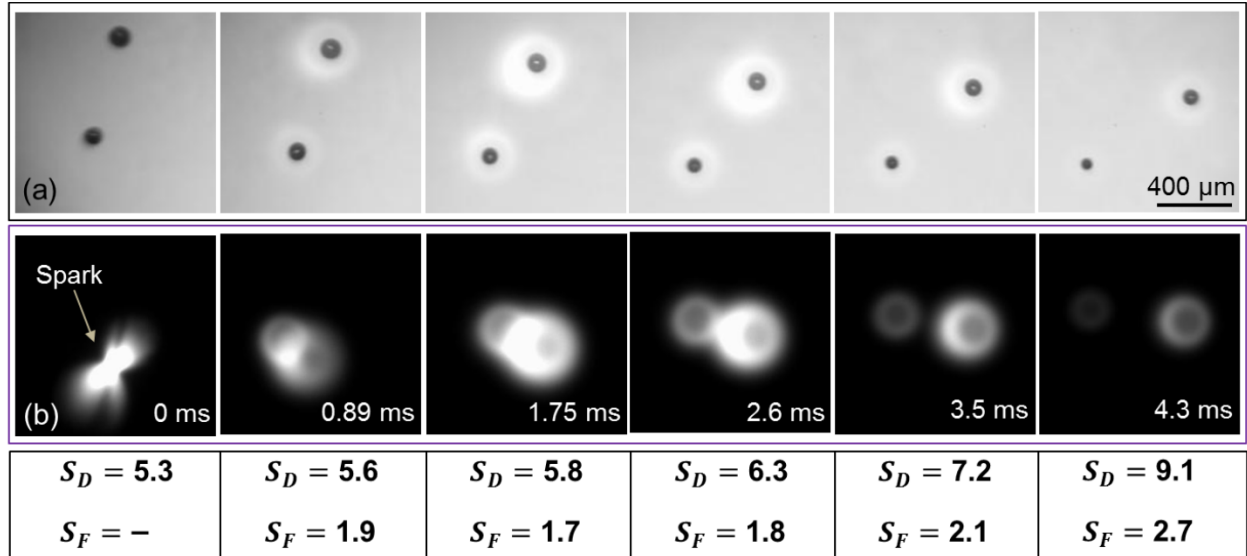


Figure 3.10: High-speed cameras recorded (a) droplet frames in the x-y plane and (b) flame frames in the x-z plane of the weak interaction case of double droplet combustion in pure oxygen atmosphere. The droplets in the merged frames from left to right correspond to the upward movement in the experiment. Below each flame frame the corresponding droplet spacing and flame spacing are given. At the moment of spark ignition ($t = 0$ ms), the initial droplet diameters of the first and second droplet are 116 and 98 μm , respectively. The initial droplet velocities of the first and second droplet are 0.77 and 0.73 m/s, respectively.

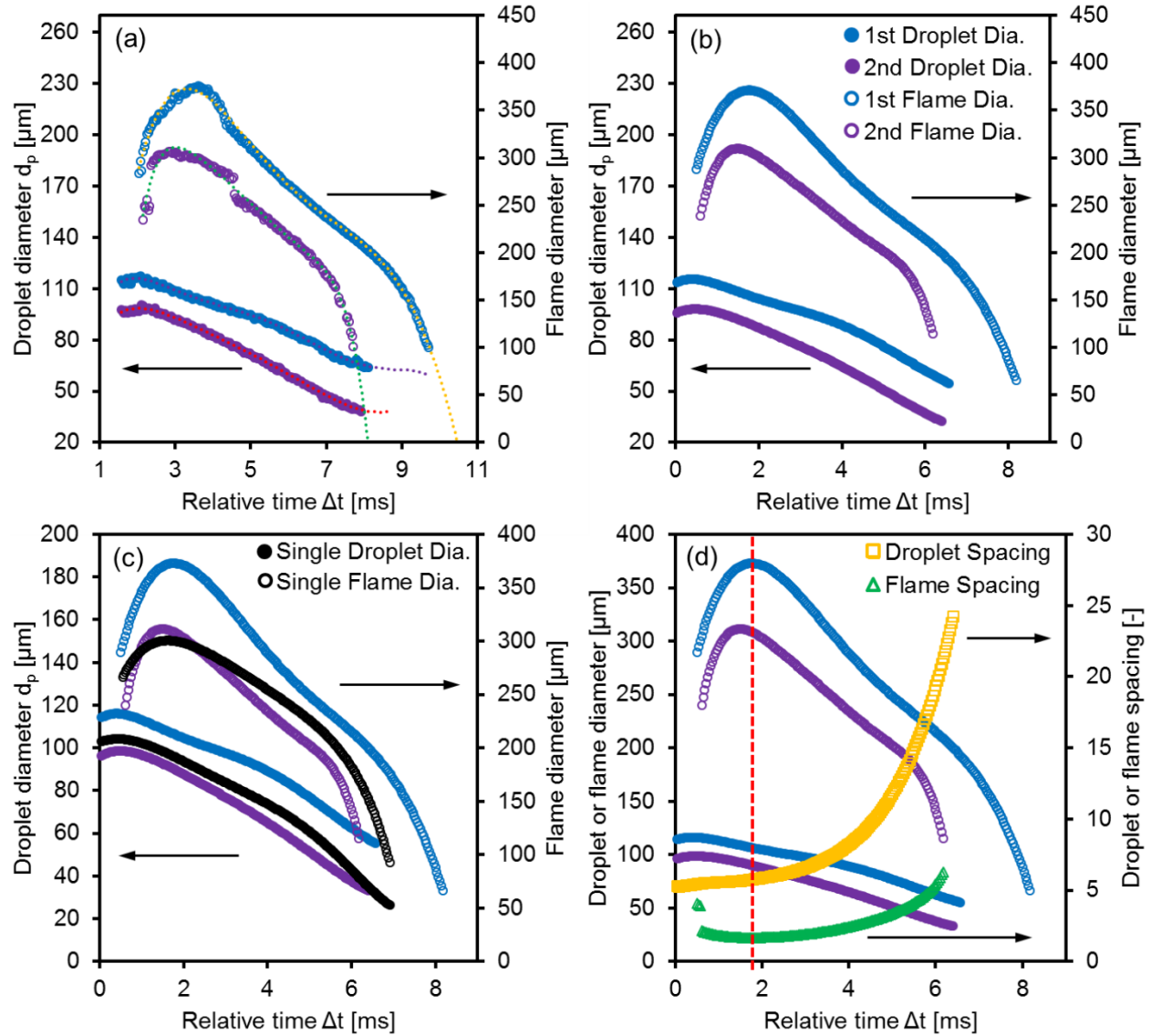


Figure 3.11: Measured data from the weak interaction case of double droplet combustion: (a) droplet diameter changes (solid circles) and flame diameter changes (empty circles), and their polynomial fitting curves (dotted lines), (b) polynomial fitting curves, (c) the comparison of droplet diameters and flame diameters with single droplet combustion, and (d) droplet spacing and flame spacing. The red vertical dashed line marks the moment of the minimum value of flame spacing. The curves in (b), (c) and (d) were shifted to set the moment of ignition to $t=0$ ms. The data of single droplet combustion is adapted and reprinted with the permission from the Ref. [39].

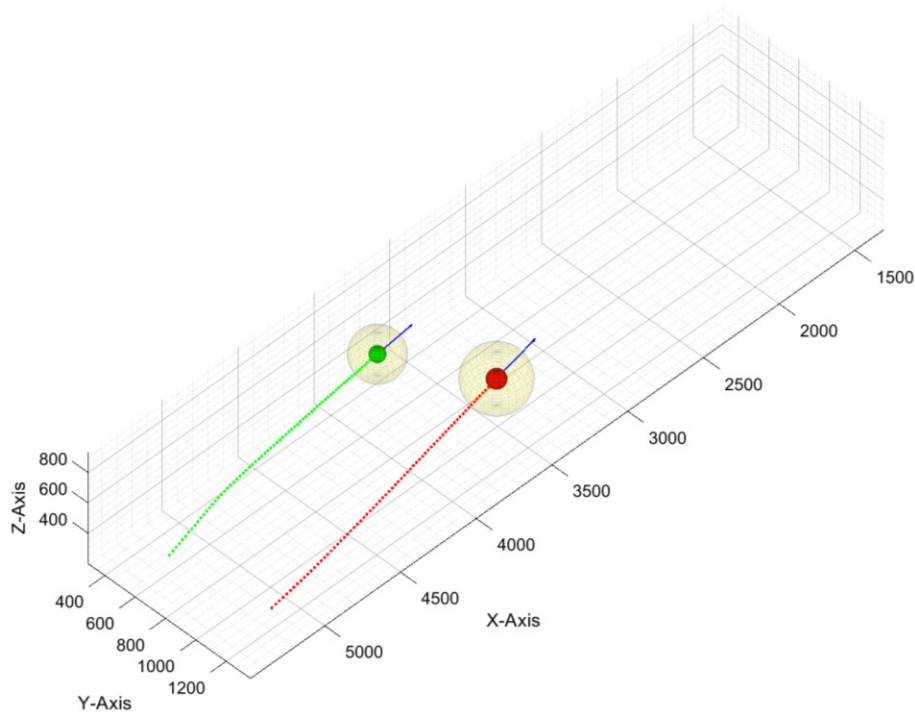


Figure 3.12: The visualized 3D image of the weak interaction case in Figure 3.10 at $t=2.5$ ms. Red and green solid sphere mean the first and second droplet, respectively. Red and green dotted line represent the 3D trajectory of the first and second droplet, respectively. Blue arrows are 3D velocities, and mesh spheres indicate flames. Deformed flame shapes are assumed as spherical in 3D image.

Figure 3.13 a and **b** show high-speed camera recorded droplet frames and flame frames of the strong interaction case [$Min(S_F) = 1.2$], respectively. The first droplet and second droplet have an initial diameter of $107 \mu\text{m}$ and $112 \mu\text{m}$, respectively. The time interval between two continuous frames is 0.82 ms, corresponding to a frame interval of 23. The flames of the strong interaction case have higher brightness and deformed shapes from 0.82 to 3.29 ms, compared to single isolated droplet combustion (**Figure 3.7**) and the weak interaction case (**Figure 3.10**). The strong interaction case has a smaller minimum flame spacing than the weak interaction case, and thus the influences of droplet interaction are starker. Both the first droplet and the second droplet display a period of slow droplet diameter regression in comparison with single droplet combustion

(Figure 3.14 c). While the droplet spacing increases almost linearly from 4.1 to 8.1 with respect to the relative time from 0 to 4.8 ms, the flame spacing decreases from 1.6 to the minimum value of 1.2 and then increases slowly to 2.3 (Figure 3.14 d). When two burning droplets are near enough, their separated flames can merge into one enveloped flame. Therefore, critical flame spacing [$S_F(t) = 1$, representing the two flame fronts starting to merge] is used to distinguish separated flames and merged flames during double droplet combustion. The critical flame spacing is absent in the strong interaction case, although the two droplets are really near to each other at the minimum flame spacing of 1.2 (Figure 3.13, $t=1.64$ ms). It is the reason of the pure oxygen ambience. According to the previous work from Sivasankaran et al. [99], increasing oxygen concentrations in the atmosphere reduces flame size and thus diminishes the interaction from the neighboring droplet.

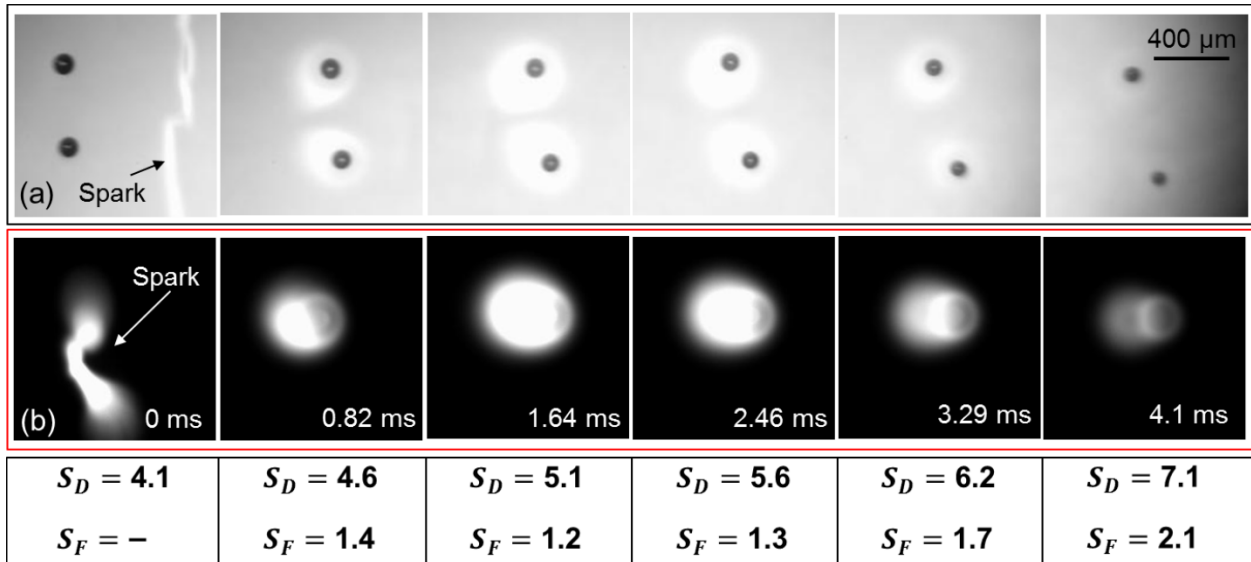


Figure 3.13: The two time-synchronized high-speed cameras recorded (a) droplet frames in the x-y plane and (b) flame frames in the x-z plane of the strong interaction case of double droplet combustion in pure oxygen atmosphere. The droplets in the merged frames from left to right correspond to the upward movement in the experiment. Below each droplet frame the corresponding droplet spacing and flame spacing are given.

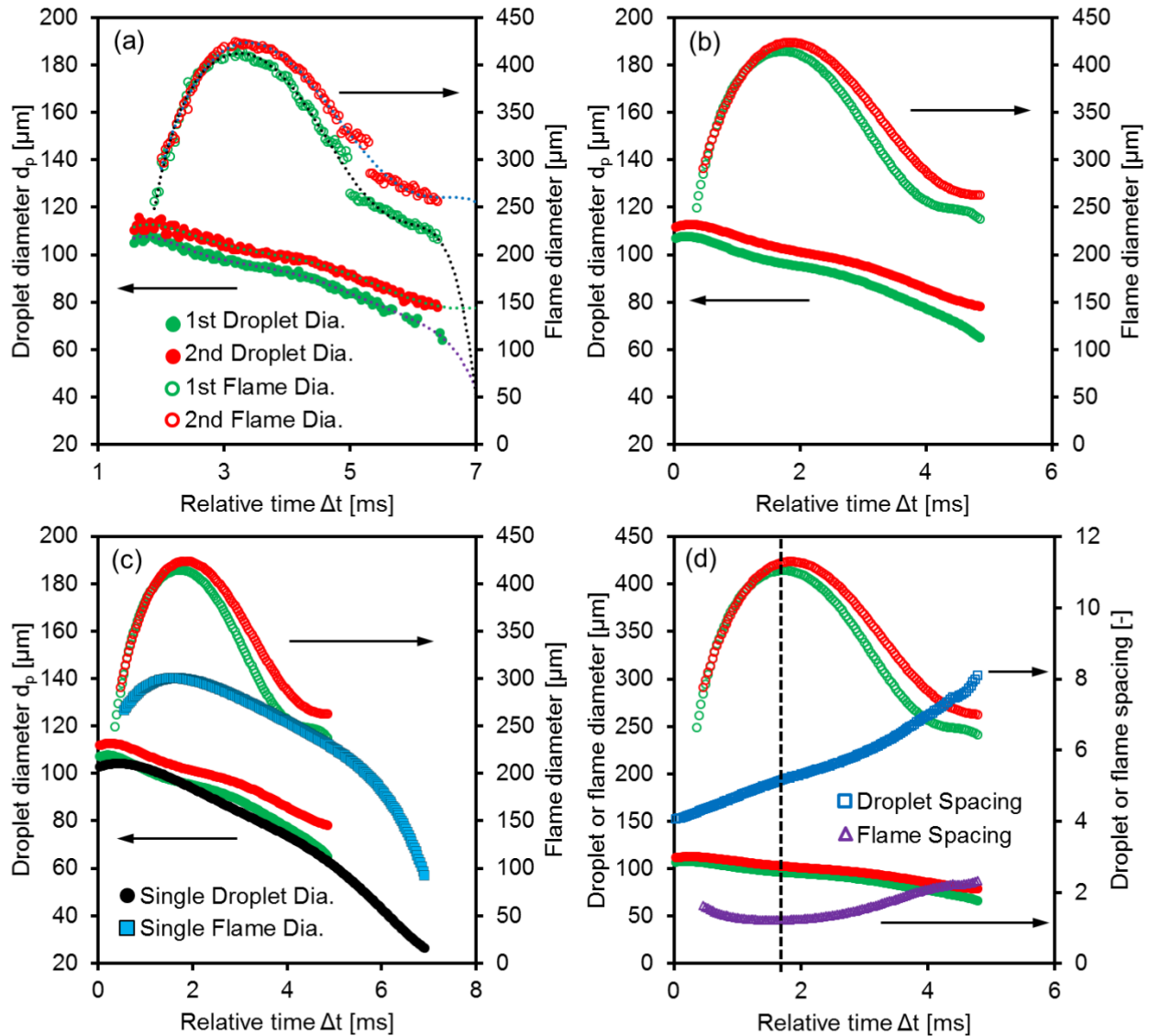


Figure 3.14: Measured data from the strong interaction case of double droplet combustion: (a) droplet diameter changes (solid circles) and flame diameter changes (empty circles), and their polynomial fitting curves (dotted lines), (b) polynomial fitting curves, (c) the comparison of droplet diameters and flame diameters with single droplet combustion, and (d) droplet spacing and flame spacing. The curves in (b), (c) and (d) were shifted to set the moment of ignition to $t=0$ ms. The data of single droplet combustion is adapted and reprinted with the permission from the Ref. [39].

Flame standoff ratio or flame-front standoff ratio was applied to characterize the time-resolved luminous flame position above droplet surface, which is defined as the ratio of flame diameter to

droplet diameter at a specific moment [$Flame\ standoff\ ratio = \frac{L(t)}{D(t)}$]. While the flame standoff ratios of single droplet combustion and the second droplet in the weak interaction case slightly increase from 0.7 to 4.2 ms, the flame standoff ratio of the first droplet in the weak interaction case increases from 0.7 to 2.4 ms, and then decrease with the relative time (**Figure 3.15 a**, black, purple and blue circles). It is a result of the influence of droplet interaction, which makes the flame of the first droplet in the weak interaction case enlarged and bright near the minimum flame spacing (**Figure 3.15 c**). Different with single droplet combustion and the weak interaction case, the flame standoff ratios of the strong interaction case increase significantly from 0.7 to 1.9 ms and further drop drastically. The strong interaction case has a smaller minimum value of the flame spacing [$Min(S_F)$], and thus the influences of droplet interactions are stronger compared with the weak interaction case. The captured droplet and flame frames at the minimum flame spacing (**Figure 3.15 b and c**) support this point. The flame standoff ratios of single droplet combustion and the weak interaction case reduce near the end of combustion, which is due to the increasing error or uncertainty of droplet diameter and flame diameter. Two points are attributed to this increasing error or uncertainty: (1) The diffraction-limited airy ring effects; (2) The difficult measurement of flame diameter caused by the decrease of flame brightness near the end of combustion. More detailed information on the two interaction cases at their minimum flame spacing are shown in **Table 3.2**.

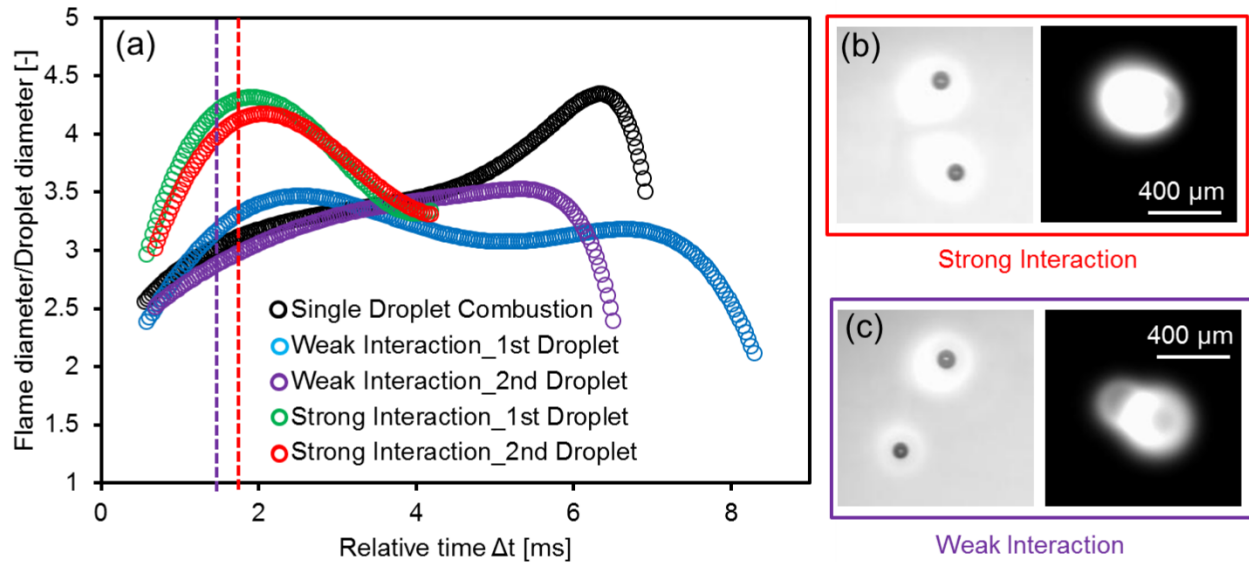


Figure 3.15: (a) Comparison of the flame standoff ratio, (b) the captured droplet and flame frames at the minimum flame spacing of the strong interaction case [dashed vertical red line in (a)], (c) the captured droplet and flame frames at the minimum flame spacing of the weak interaction case [dashed vertical purple line in (a)]. In the frames of (b) and (c), from left to right the droplets move in the upward direction in the experiment. The droplet and flame of the first droplet are on the right side in each frame. The data of single droplet combustion is adapted and reprinted with the permission from the Ref. [39].

Table 3.2: Information of the weak interaction case [$Min(S_F) = 1.7$] and the strong interaction case [$Min(S_F) = 1.2$] of double droplet combustion, at the moment of their corresponding minimum flame spacing.

	Weak interaction	Strong interaction
Minimum flame spacing (-)	1.7	1.2
Relative time from droplet ignition (ms)	1.75	1.64
Droplet spacing	5.8	5.1
1st droplet diameter (μm)	107	97
2nd droplet diameter (μm)	90	103
1st flame diameter (μm)	373	414
2nd flame diameter (μm)	309	422
1st droplet 3D velocity (m/s)	0.63	0.83
2nd droplet 3D velocity (m/s)	0.54	0.76
Separation distance (μm)	567	512

Figure 3.16 shows the comparison of normalized squared droplet diameters and burning constant among single droplet combustion, the weak interaction case, and the strong interaction case. For the weak interaction case, the normalized squared droplet diameter of the first droplet decreases rapidly and the burning constant decreases significantly from 0.11 to 0.22 $\text{ms}/\mu\text{m}^2$, compared to single droplet combustion. The normalized squared droplet size and burning constant of the second droplet in the weak interaction case are barely influenced by droplet interactions (**Figure 3.16 a and b**), although its flame size is enlarged and flame brightness is enhanced (**Figure 3.15 c**). The heat transfer from the first droplet can compensate the influence of the competition of oxygen. The previous investigation from Cho et al. [100] suggests that the flame of the first droplet resulted in a lateral flame in front of the second droplet, which in turn promptly evaporated the second droplet.

Compared to single isolated droplet combustion, regression rate of droplet squared diameter in

the strong interaction case decreases slowly from 0.07 to 0.23 ms/ μm^2 , and then reduces linearly with time like single droplet combustion (**Figure 3.16 c**). The minimum value of the flame spacing in the strong interaction case occurs at the normalized time of 0.21 ms/ μm^2 , where the droplet diameter regression rate greatly decreases and the burning constant dramatically diminishes (**Figure 3.16 c and d**). This change is caused by the competition of oxygen for more droplets in a particular finite volume in the ambience, which leads to the enlarged flame size in order to maintain the stoichiometric consumption ratio of the fuel vapor to the oxidizer at the flame front [101]. The enlarged flame size enhances the diffusion path of the p-Xylene molecules to the flame sheet, and thus hinders the intended pyrolysis of the p-Xylene molecules. This effect gives rise to the acceleration of soot formation and thus blackbody radiation. As a result, the flame brightness was enhanced, as verified by the flame brightness in **Figure 3.13**. Therefore, soot formation accelerates and the droplet burning constant reduces with decrease of the flame spacing. This point is supported by previous investigations from Sangiovanni and his coworkers on droplet interactions and soot formation characteristics of a continuous stream of fuel droplets of uniform size and spacing. They indicated that decreasing droplet spacing significantly enhances the soot formation and extends burning time of interacting droplets [102, 103]. Moreover, as droplet spacing decreases, the interactions between neighboring droplets reduce the heat and mass transfers compared to the isolate droplet, and thus decrease the droplet evaporation rate and prolong droplet evaporation and/or combustion time [84]. Different from previous investigations, hereby flame spacing instead of droplet spacing was used as an influencing factor to assess droplet interactions, because of the high time-resolved information of flame diameters and separation distances between two droplet centers using the developed 3D measurement technique. The accuracy of the measured information is shown in **Table 3.3**.

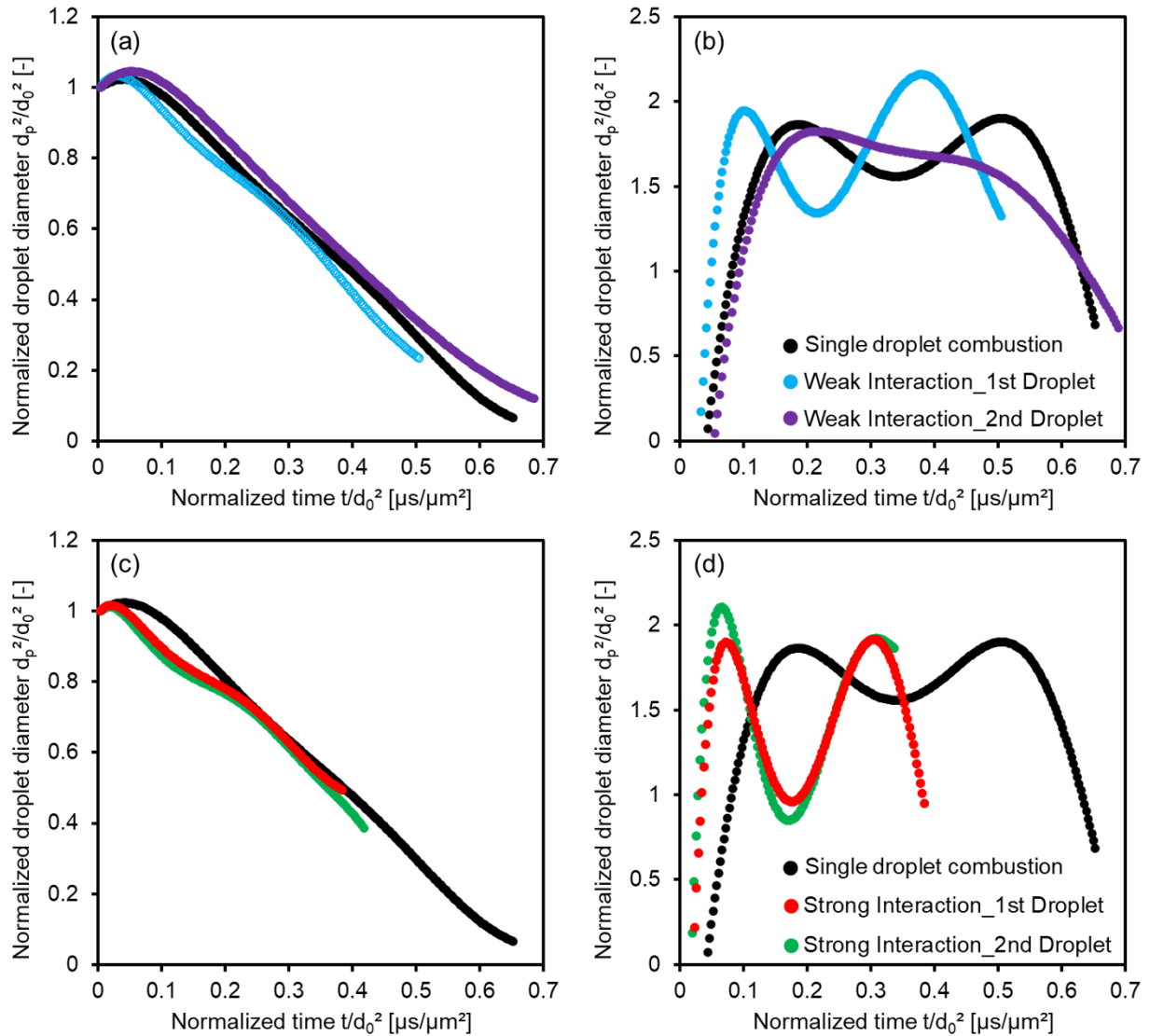


Figure 3.16: Comparison of single droplet combustion with the strong interaction case of double droplet combustion: (a) normalized squared droplet diameter, (b) burning constant. Comparison of single droplet combustion with the strong interaction case of double droplet combustion: (c) normalized squared droplet diameter, (d) burning constant. This data of single droplet combustion is adapted and reprinted with the permission from the Ref. [39].

Table 3.3: Accuracies of the measured information. The accuracy of time resolution is calculated according to the recording speed rate of the used high-speed camera. The other accuracies are calculated according to the pixel sizes of the used high-speed camera and objectives.

	Accuracy
Time resolution	0.0357 ms
Droplet diameter	$\pm 6.25 \mu\text{m}$
Flame diameter	$\pm 6.25 \mu\text{m}$
Droplet center position, X	$\pm 6.25 \mu\text{m}$
Droplet center position, Y	$\pm 6.25 \mu\text{m}$
Droplet center position, Z	$\pm 4.2 \mu\text{m}$
Droplet 3D velocity	$\pm 0.0098 \text{ m/s}$
Separation distance	$\pm 9.8 \mu\text{m}$

During the weak interaction case of double droplet combustion, flame size and brightness vary from the relative time of 0.6 to 4.3 ms, compared to single isolated droplet combustion. Thus, this time is considered as the interaction period, where the effect from neighboring droplet is reflected. During this period, the largest values of droplet spacing and flame spacing are 9.1 and 2.7, respectively (**Table 3.4**). Thus, these two values are the critical values, below which droplet interaction occurs during double droplet combustion in the pure oxygen atmosphere.

Table 3.4: Information on droplet interactions of double droplet combustion in the relative time range from 0.6 to 4.3 ms. The moment of spark ignition is regarded as the relative time of 0 ms.

	Weak interaction
Droplet spacing range (-)	5.3 to 9.1
Flame spacing range (-)	1.7 to 2.7
1st flame standoff range (-)	2.7 to 3.6
2nd flame standoff range (-)	2.6 to 3.7

3.3.3 Double droplet combustion of p-Xylene in the mixture of oxygen and nitrogen

To study the influence of oxidizing ambiances and to achieve the merged flames during double droplet combustion, the oxidizing atmosphere was varied to a mixture of oxygen and nitrogen (200 mL/min oxygen and 200 mL/min nitrogen) using two mass flow controllers (Bronkhorst-EL Flow). **Figure 3.17** shows high-speed camera recorded frames of two p-Xylene droplets burning in the mixture of oxygen and nitrogen. The first and second droplet have an initial diameter of 100 and 116 μm , respectively. Reducing the oxygen concentration in the ambience enlarges flame size and thus promotes flame merging. Therefore, the partial merged flames were observed at $t=3.6$ ms, where flame spacing and droplet spacing are 0.6 and 3.4, respectively. Wings appear at the lee side of the droplet flame, which is new finding compared to the droplet combustion in pure oxygen atmosphere. The formation of flame wings is caused by the buoyancy as well as velocity difference between the droplet and the co-flowing atmosphere.

When the two flames merging, leakages of soot particles (emitting white light via blackbody radiation) from flames were observed at 3.6, 4.8, and 6.0 ms in **Figure 3.17**. The flame front could be regarded as a thin shell or sheet, where the reaction between the fuel vapor and the surrounding oxidizer takes place at a stoichiometric consumption rate to establish a diffusion flame. Before reaching the flame front, the fuel vapor undergoes high temperature pyrolysis,

leading to the formation of soot particles in the area from droplet surface to flame front [104]. As the flame regresses inward, the soot enclosed by the flame front would be finally oxidized and thus very little soot would be released during near-complete combustion [105]. In the present work, the enclosure of the flame front was broken when two flame fronts partly merge into each other. Therefore, emissions of soot particles were observed *via* the high-speed camera.

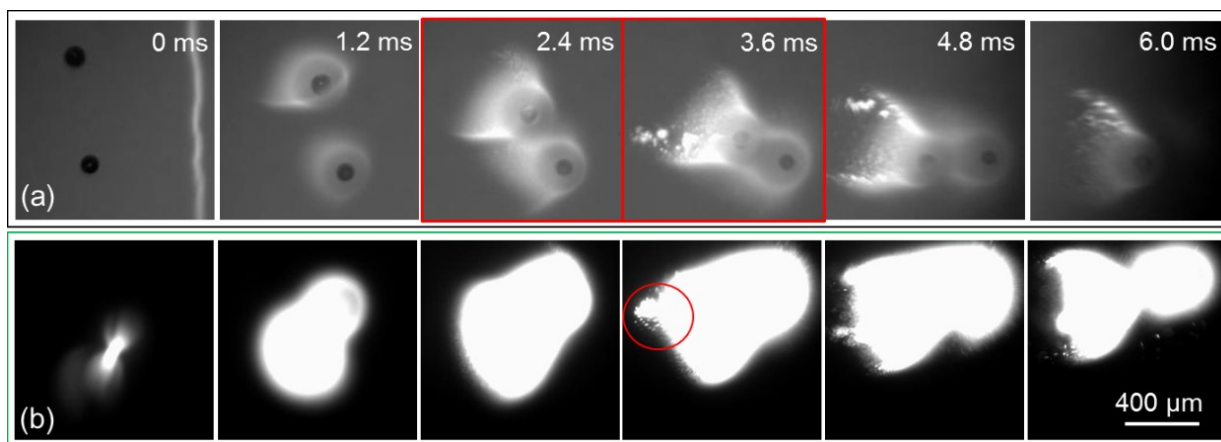


Figure 3.17: The two time-synchronized high-speed cameras recorded (a) droplet frames in the x-y plane and (b) flame frames in the x-z plane of double droplet combustion of p-xylene in the mixed gases (200 mL/min oxygen and 200 mL/min nitrogen). The droplets in the merged frames from left to right correspond the upward movement in the experiment. The exposure times of the droplet and flame frames are 7 μ s and 30 μ s, respectively. This figure is adapted and reprinted with the permission from the Ref. [39].

3.3.4 Double droplet combustion of precursor solutions in pure oxygen atmosphere

Continuous and multiple surface micro-explosions were observed using high-speed camera imaging technique during single droplet combustion of many precursor solutions (**Appendix A.1**). However, the occurrence of this kind of surface micro-explosion during double droplet combustion is still unknown. In addition, the effects of droplet interactions on double droplet combustion of pure solvent have been shown in subchapters of 3.3.2 and 3.3.3. Therefore, for the first time, double droplet combustion experiments of precursor solutions are performed in order to identify

3 Three-dimensional measurements of double droplet combustion

the occurrence of droplet micro-explosions as well as to investigate the effects of droplet interactions.

The single droplet combustion experiment of 0.5 mol/L FeNAP/P-Xylene was done first to provide a comparison baseline, which demonstrates five times of continuous explosions (**Figure 3.18**).

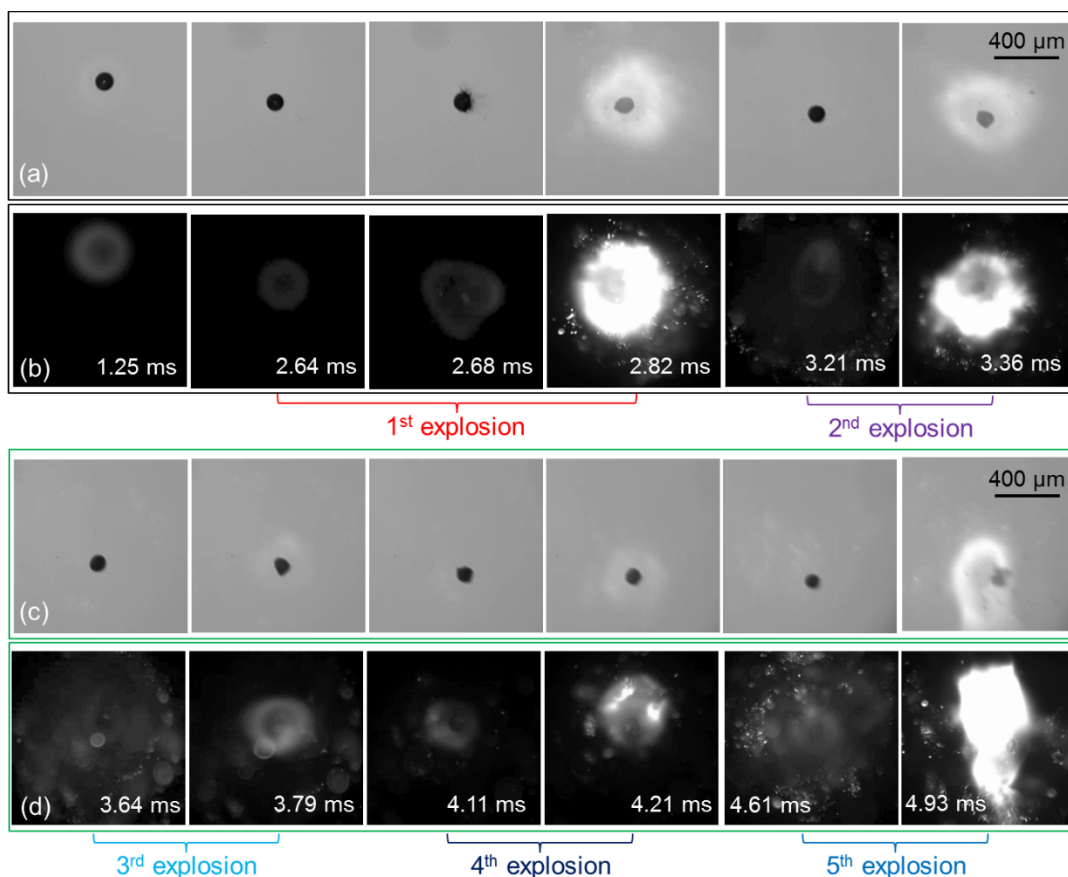


Figure 3.18: High-speed cameras recorded [(a), (c)] droplet frames in the x-y plane and [(b), (d)] flame frames in the x-z plane of single droplet combustion of 0.5 mol FeNAP/p-Xylene in pure oxygen atmosphere. The contrast of flame frames is improved in order to make flames more visible in the printed version. The droplets in the merged frames from left to right correspond to the upward movement in the experiment. At the moment of spark ignition ($t=0$ ms), the initial droplet diameter and initial droplet velocity are 128 μm and 0.86 m/s, respectively.

Droplet surface explosions were detected during double droplet combustion of 0.5 mol FeNAP/p-Xylene, which has a minimum value of flame spacing of 1.6 at the relative time of 1.07 ms (**Figure 3.19**). Hereby the values of flame spacing and droplet spacing after the first explosion are missing because of the deformed shapes of droplet and flame as well as the ejected fuels from droplet surface explosion. For the first droplet, the first surface explosion occurs at the relative time of 1.96 ms, where the fuel is secondarily atomized to form small ejected fragments. These ejected fragments spread out, mix with the surrounding oxygen, and form a large and bright flame at the relative time of 2.04 ms. The second surface micro-explosion of the first droplet is also observed in the relative time range from 2.29 to 2.61 ms. Compared to the first droplet, the first and second surface micro-explosions of the second droplet appear a little bit later at the relative times of 2.14 ms and 2.61 ms, respectively. It is due to its large initial droplet diameter. Hereby, the real recording time is shifted to define the moment of droplet ignition as the relative time of 0 ms.

3 Three-dimensional measurements of double droplet combustion

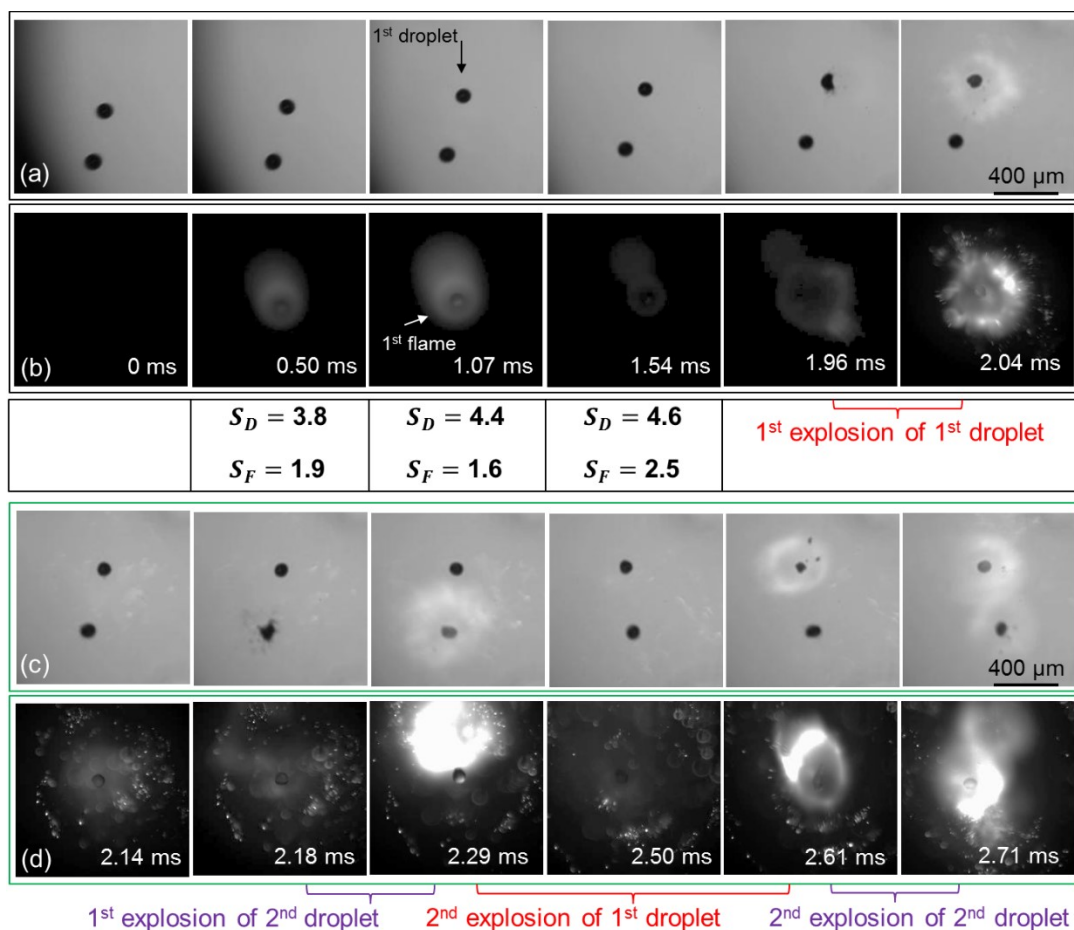


Figure 3.19: High-speed cameras recorded [(a), (c)] droplet frames in the x-y plane and [(b), (d)] flame frames in the x-z plane of double droplet combustion of 0.5 mol FeNAP/p-Xylene in pure oxygen atmosphere. The contrast of flame frames is improved in order to make flames more clearly in the printed version. The droplets in the merged frames from left to right correspond the upward movement in the experiment. The first droplet and second droplet have initial diameters of 108 μm and 111 μm , respectively.

To verify the reproducibility of this type of explosion, double droplet combustion experiment with a smaller minimum value of flame spacing of 1.1 was carried out (**Figure 3.20**). The two droplets have a close distance and their flames nearly touch with each other at the moment of the minimum flame spacing ($t=0.82$ ms). Continuous surface micro-explosions happen as well for these two droplets, demonstrating the occurrence of explosions during double droplet combustion of 0.5 mol

FeNAP/p-Xylene.

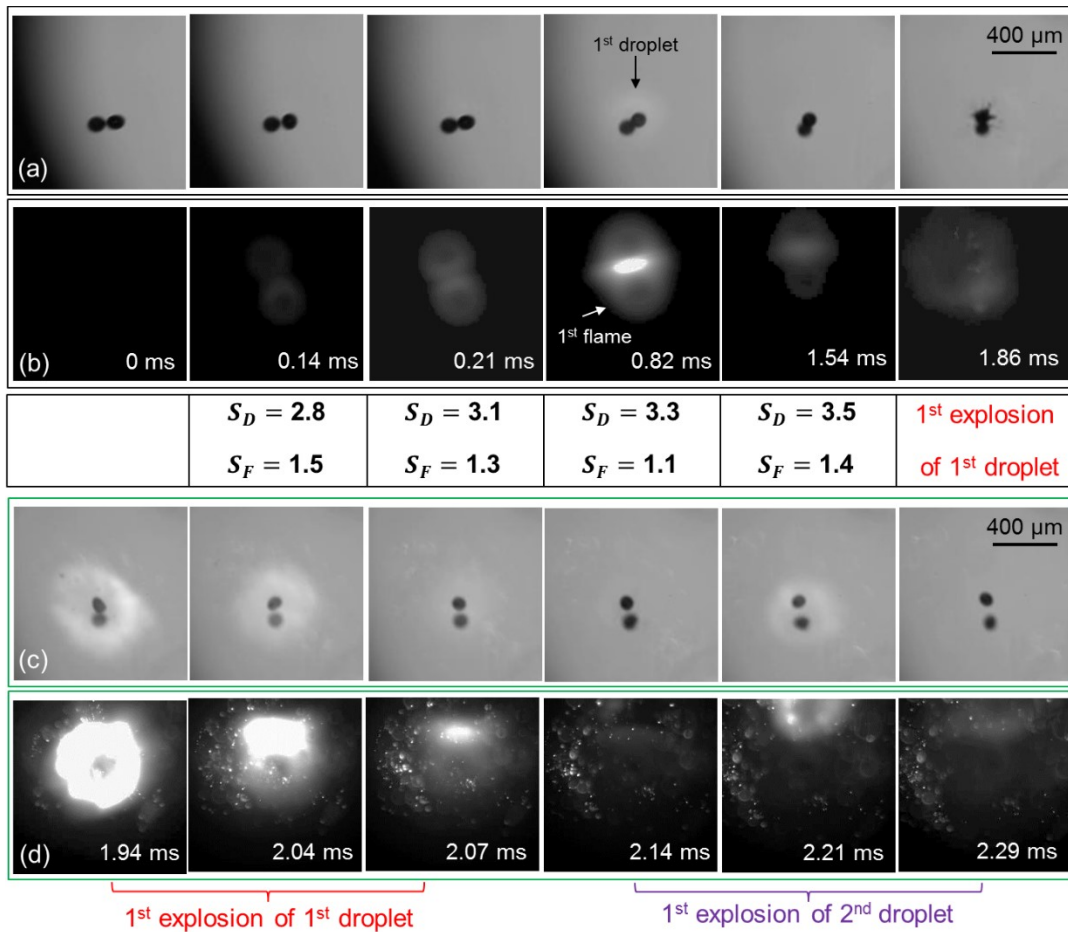


Figure 3.20: High-speed cameras recorded [(a), (c)] droplet frames in the x-y plane and [(b), (d)] flame frames in the x-z plane of double droplet combustion of 0.5 mol FeNAP/p-Xylene in pure oxygen atmosphere. The contrast of flame frames is improved in order to make flames more clearly in the printed version. The droplets in the merged frames from left to right correspond the upward movement in the experiment. The first droplet and second droplet have initial diameters of 103 μm and 109 μm , respectively.

To study the effect of droplet interaction on droplet explosions, the normalized droplet explosion times (left axis in **Figure 3.21**) and the normalized time between two successive explosions (right axis in **Figure 3.21**) are compared among single droplet explosions with the two cases of double

droplet explosions. In **Figure 3.21**, weak interaction and strong interaction are the double droplet combustion cases with minimum values of flame spacing of 1.6 and 1.1, respectively. The normalized droplet explosion times of single droplet combustion and the two droplets in the weak interaction case are very close values, and so are the normalized times between two successive explosions (**Figure 3.21 a**). While the influence of droplet interactions on the first droplet in the weak interaction case of p-Xylene is reflected (**Figure 3.16 b**, the interaction period is 3.7 ms), it is absent on droplet explosions of the weak interaction case of 0.5 mol/L FeNAP/p-Xylene even though the changes of flame size and brightness were seen from 0.5 ms to 1.54 ms (**Figure 3.19**). It is mainly caused by the short interaction period, which is 1.04 ms for the weak interaction case of double droplet combustion of 0.5 mol/L FeNAP/p-Xylene.

The normalized droplet explosion times of single droplet combustion are slightly smaller than the two droplets in the strong interaction case (left axis in **Figure 3.21 b**), indicating that droplet interactions postpone occurrences of droplet explosions. It is known from double droplet combustion experiments of p-Xylene that droplet interactions reduce the heat and mass transfer between droplet surface and flame front, and hence decrease droplet evaporation rate and prolong droplet-burning time (**Figure 3.16 c and d**). For double droplet combustion experiments of 0.5 mol/L FeNAP/p-Xylene, the enlarged flame size and the accelerated soot formation reduce the heat and mass transfer between flame front to droplet surface, delaying the processes of shell formation and heterogeneous vapor nucleation. Regarding to the normalized times between two successive explosions, the first and second droplet in the strong interaction case have almost the same values as single droplet combustion, apart from the first explosion which have larger values of 8.7% and 7.7%, respectively (left axis in **Figure 3.21 b**). It demonstrates that the influence of droplet interactions happens before the first explosion. Even though the large flame formed by ejected fragments could affect the neighboring droplet, this influence occurs at a very short time (less than 0.2 ms) and thus can be ignored.

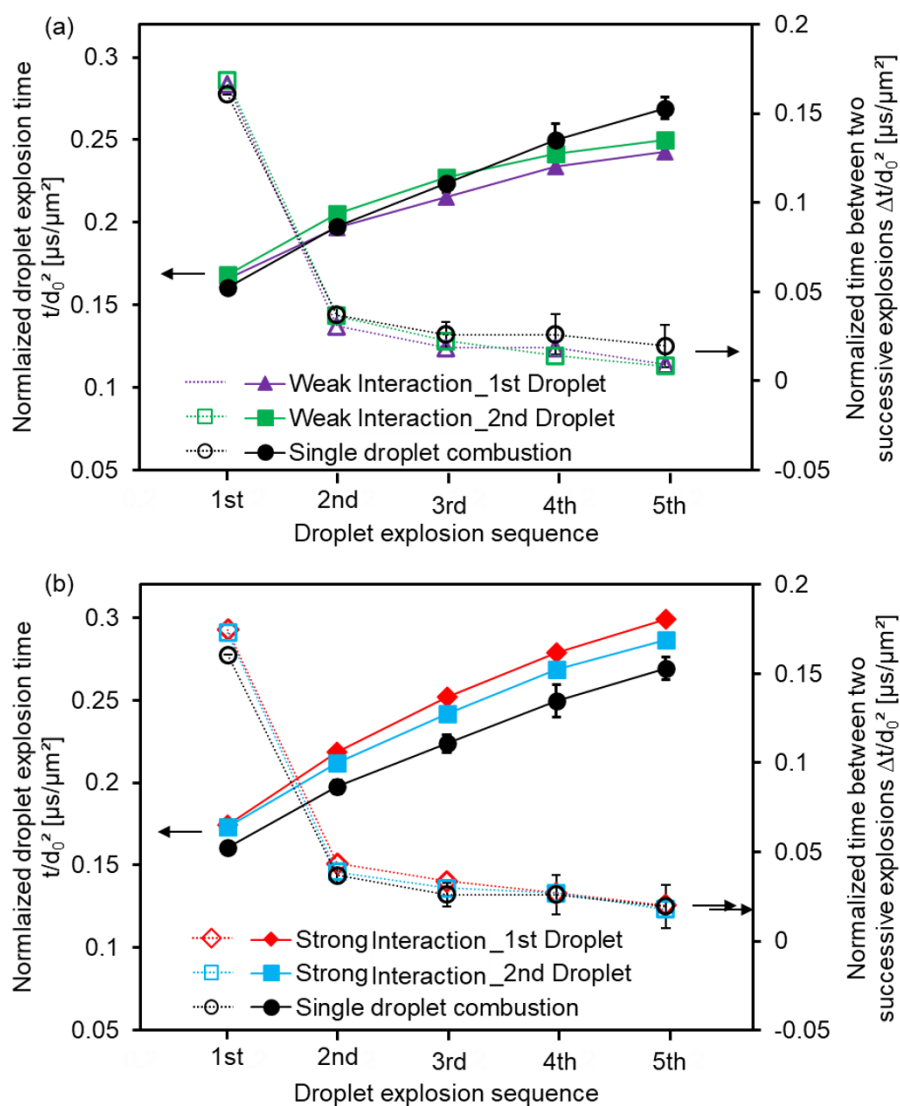


Figure 3.21: Comparison of single droplet combustion with the weak interaction case (a) and strong interaction case (b) of double droplet combustion of 0.5 mol FeNAP/p-Xylene: normalized droplet explosion time (left axis, solid lines, solid points), and normalized times between two successive explosions (right axis, hollow points, dashed lines). The normalized times between two successive explosions of 1st droplet explosion was calculated as the time difference between the first droplet explosion and spark ignition.

3.4 Summary and conclusions

3.4.1 Summary

- (1) The 3D-measurement technique using two highly time-synchronized high-speed cameras was developed to detect single and double droplet combustion processes of the pure solvent. The obtained information contain droplet diameters, flame diameters, droplet 3D trajectories, droplet 3D velocities, and the center distances between the two burning droplets, which were visualized into 3D images.
- (2) In the pure oxygen ambience, regarding to the variations of flame size and brightness, droplet interactions were observed when the droplet spacing and the flame spacing are below 9.1 and 2.7, respectively. As the flame spacing becomes small, the competition of oxygen in the surrounding ambience increases the flame size, brightness and standoff ratio as well as decreases the droplet burning constant.
- (3) Reducing oxygen concentrations in the ambience increases the flame size and brightness, deforms flame shape, resulting in the formation of partial merged flames. The destruction of flame fronts leads to the emission of soot particles from flames.
- (4) For the first time, droplet explosions were observed using high-speed cameras during double droplet combustion of precursor solutions. Double droplet explosions were continuous and multiple as single droplet explosions. Droplet interactions postpone the occurrence of double droplet explosions. However, this effect highly depends on the period and degree of droplet interaction.

3.4.2 Conclusions

- (1) Three-dimensional measurements of single and double droplet combustion processes of the pure solvent and the precursor solution can be done using two highly time-synchronized high-speed cameras. The obtained highly time-resolved 3D information will be an ideal reference for modeling and simulating droplet interactions during combustion.

- (2) Droplet interaction occurs when the distance between two burning droplets is below a critical value. The critical parameters including droplet spacing and flame spacing, below which droplet interaction occurs, can be determined. Droplet interaction is the result of more droplets competing for oxygen in a specific volume, which reduce droplet burning constant and prolong droplet combustion lifetime.
- (3) Partly merged flames and emissions of soot particles can be achieved when decreasing the oxygen concentration in the atmosphere. These two behaviors are expected to influence droplet explosions, the release of gas-phase precursor from droplet surface to flame front, and nanoparticle synthesis.
- (4) Micro-explosion occurs not only in single droplet combustion experiment but also in double droplet combustion experiment, when the appropriate precursor solution is used. The occurrence of droplet explosions could be delayed by droplet interaction when the interaction period and degree are enough.

4 Digital in-line holography measurements of single droplet combustion

4.1 State of art

The word “holography” originates from two Greek words: “holos” and “graphein”, which mean “complete or whole” and “writing or recording”, respectively. Hence, the word “holography” has the meaning of recording complete information of an object [106]. The light scattered from an object contains two important data of information: amplitude and phase. Both types of information help to reconstruct the three-dimensional (3D) shape of the object. Photography is only able to record the intensity of the object, and thus it is a two-dimensional (2D) recording technique requiring an in-focus image of the object. In contrast, holography is a 3D technique recording both for amplitude and phase, giving rise to a 3D image of the object via holographic reconstruction [107].

Digital in-line holography (DIH) is a simple and powerful tool to image objects, where the reference wave and the object wave are illuminated onto a photographic plate [108]. The Hungarian-British electrical engineer and physicist, Dennis Gabor, first proposed the principle of this holographic method (DIH setup) in 1948 and was awarded the Nobel Prize in Physics in 1971 due to his outstanding contributions to the invention and development of holography [109, 110]. With the development of digital cameras, especially, charge coupled device (CCD) and complementary metal oxide semiconductor (CMOS) sensors and numerical reconstruction methods, DIH technique is widely used to investigate 3D imaging of small objects [111-114]. Today, this high-sensitivity 3D imaging technique has found extensive applications in particle characterization (size, velocity, trajectory, shape, deformation, and refractive index) [113, 115], fluid mechanics [116], and biology [117].

The DIH technique has been widely used to investigate burning particles, droplets and sprays. Webster *et al.* used the DIH technique to in-situ detect droplet sizes and droplet 3D distributions in burning sprays, and indicated that during the measurement the flame and/or combustion

process remains undisturbed [118]. Guildenbecher *et al.* measured burning surfaces, droplet morphologies and reaction zones of molten aluminum droplet combustion in solid propellant plumes using the DIH technique. They suggested that DIH can provide an order of magnitude increase in the effective data compared to traditional imaging [119]. Wu *et al.* measured particle size and the 3D location of reacting coal powders in a pulverized flame, demonstrating the feasibility of using DIH to measure large burning particle flow fields. Chen *et al.* used DIH to experimentally detect 3D information (position, size, and velocity) of aluminum particle combustion in ammonium perchlorate based solid-rocket propellants [120]. Wu *et al.* first developed a long working distance (more than 15 cm) DIH system, which was used to in-situ characterize coal particle combustion with a spatial resolution of 3.9 μm [121]. Yao *et al.* employed a high-speed DIH technique to visualize and quantify the particle and volatile evolution during pulverized coal combustion [122]. Reviewing the previous work, the DIH technique has shown its ability to detect sizes, 3D distributions, velocities and trajectories of burning droplets (and/or particles). However, it is rarely used to investigate the flame surrounding the burning droplet, measure refractive index and temperature. Heat and mass transfer occurring from droplet surface to flame front and/or the surrounding atmosphere are important to understand droplet evaporation and combustion. In the case of a burning droplet (and/or particle), the fuel evaporates from the droplet surface, and further diffuses towards the flame front, where it reacts with oxidizers from the ambient atmosphere. The heat produced from the exothermic reaction at the flame front transfers through conduction and radiation outward to the ambient atmosphere and inward back to the droplet surface. The area between the droplet surface and the flame front contains evaporated fuels, some products generated from the flame front, and soot generated from thermal decomposition of fuels [123, 124]. There is a temperature gradient from the droplet surface to the flame front with an increasing tendency, resulting into a gradient of the refractive index. Additionally, temperature and/or composition changes take place in the droplet diffusion flame as well as near the surface of fast evaporation droplet, resulting in variations of the refractive index

surrounding the droplet [18, 19]. This kind of refractive index gradient changes the light scattering, leading to variations of a recorded hologram. Therefore, a hypothesis is proposed that the DIH hologram signals could be influenced by the refractive index gradients surrounding the burning and fast evaporating droplets.

In this chapter, the DIH theory, the construction of experimental setups, the development of methods for hologram formation and numerical reconstruction, and the measurements on non-burning and burning droplets will be introduced and discussed. The target is to study the influence of the flame surrounding the burning droplets on the formed hologram signals, and to seek a way to estimate the refractive index gradient caused by the flame using DIH.

4.2 Theory

4.2.1 The wave nature of light and the scalar diffraction theory

Light is a vector electromagnetic wave, where oscillations of the coupled electronic and magnetic fields occur according to the Maxwell's equations. The Maxwell's equations compose of four equations including Gauss' electric field law, Gauss' magnetic field law, Faraday's induction law, and Maxwell-Ampere law, as shown below:

$$\nabla \cdot \mathbf{D} = \rho_V \quad (1)$$

$$\nabla \cdot \mathbf{B} = 0 \quad (2)$$

$$\nabla \times \mathbf{E} = -\frac{\partial \mathbf{B}}{\partial t} \quad (3)$$

$$\nabla \times \mathbf{H} = \frac{\partial \mathbf{D}}{\partial t} + \mathbf{J} \quad (4)$$

where $\nabla \cdot$, \mathbf{D} , ρ_V , \mathbf{B} , $\nabla \times$, \mathbf{E} , \mathbf{H} , and \mathbf{J} are the divergence operator, electric flux density (C/m^2), electric charge density (C/m^3), magnetic flux density (Wb/m^2), curl operator, electric field strength (V/m), magnetic field strength (A/m), and electric current density (A/m^2), respectively. Hereby,

$$\mathbf{D} = \varepsilon \mathbf{E} \quad (5)$$

$$\mathbf{B} = \mu \mathbf{H} \quad (6)$$

$$\mathbf{J} = \sigma \mathbf{E} \quad (7)$$

where ε , μ , and σ represent permittivity (F/m), permeability (H/m), and conductivity (S/m) of the medium, respectively.

The permittivity and permeability of the linear, homogeneous and isotropic medium (e.g., vacuum) are scalar constants. Thus, the Maxwell's equations can be converted into wave equations [106, 125]:

$$\nabla^2 \mathbf{E} - \frac{1}{v^2} \frac{\partial^2 \mathbf{E}}{\partial t^2} = 0 \quad (8)$$

$$\nabla^2 \mathbf{B} - \frac{1}{v^2} \frac{\partial^2 \mathbf{B}}{\partial t^2} = 0 \quad (9)$$

where, $\nabla^2 = \partial^2 / \partial x^2 + \partial^2 / \partial y^2 + \partial^2 / \partial z^2$ is the Laplacian operator in Cartesian coordinate, and $v = 1 / \sqrt{\varepsilon \mu}$ is the velocity of the wave in the medium (e.g., the velocity of the wave in vacuum, $c = 2.99794 \times 10^8$ m/s). Hereby, ε_0 and μ_0 are defined as permittivity and permeability of the vacuum, respectively. Then, compared to vacuum, the relative permittivity ε_r and relative permeability μ_r of the medium can be defined as:

$$\varepsilon_r = \sqrt{\varepsilon / \varepsilon_0} \quad (10)$$

$$\mu_r = \sqrt{\mu / \mu_0} \quad (11)$$

The velocity of the wave in the medium can be described using the equation:

$$v = c / \sqrt{\epsilon_r \mu_r} \quad (12)$$

Hereby, $\sqrt{\epsilon_r \mu_r}$ is normally represented by the refractive index of the medium, *i.e.*, $n = \sqrt{\epsilon_r \mu_r}$.

The electric field of the plane wave propagating in Cartesian coordinate from the origin point $[(0, 0, 0)]$ to another point $[\mathbf{r} (x, y, z)]$ can be expressed using the equation:

$$\mathbf{E} = \mathbf{E}_0 \cos(\mathbf{k}\mathbf{r} - \omega t) \quad (13)$$

where \mathbf{E}_0 , $k = 2\pi/\lambda$, and ω are the amplitude, wavenumber, and angular frequency of the plane wave, respectively. The wavenumber and the angular frequency can be expressed as $k = \omega/v$ and $\omega = 2\pi/T$, respectively. Here, T is the period. The wavelength of the wave is represented by the symbol of λ . The equation (13) can also be written in complex form as:

$$\begin{aligned} \mathbf{E} &= \mathbf{E}_0 e^{i(\mathbf{k}\mathbf{r} - \omega t)} \\ &= \mathbf{E}_0 \cos(\mathbf{k}\mathbf{r} - \omega t) + i \mathbf{E}_0 \sin(\mathbf{k}\mathbf{r} - \omega t) \end{aligned} \quad (14)$$

In this equation, the real part of the complex function represents the physical wave, which will be used in the calculation of the electric field [125]. The electric field \mathbf{E} , magnetic field \mathbf{B} ($\mathbf{B} = \mu\mathbf{H}$) and the propagation direction are perpendicular to each other. In addition, the electric field \mathbf{E} and magnetic field \mathbf{B} has the relationship of:

$$\frac{|\mathbf{E}|}{|\mathbf{B}|} = \frac{1}{\sqrt{\epsilon\mu}} = v \quad (15)$$

Therefore, the solution of the magnetic field of the plane wave can be obtained in a similar way.

The Maxwell's equations can be used to derive the foundations of the scalar diffraction theory [126]. The Maxwell's equations give the most rigorous physical description of light, *i.g.*, a vector electromagnetic wave with electric and magnetic fields. However, the scalar diffraction theory

assumes the light field as a complex scalar potential, which valids for cases in which the dimensions of the aperture and/or the object are much larger than the wavelength [127]. The Fresnel-Kirchhoff diffraction formula is usually used to describe and model the propagation of wave (or light) from the object to the detector plane (hologram plane) (**Figure 4.1**):

$$U(x, y, z) = -\frac{i}{2\pi} \iint \frac{e^{(ikd)}}{d} U(x_0, y_0, 0) dx_0 dy_0 \quad (16)$$

where $U(x, y, z)$ and $U(x_0, y_0, 0)$ are diffraction pattern on the detector plane (diffracted field) and light pattern scattered from the object (incident field), respectively. Here, $d = \sqrt{(x - x_0)^2 + (y - y_0)^2 + z^2}$ represents the propagation distance from the point $(x_0, y_0, 0)$ to the point (x, y, z) .

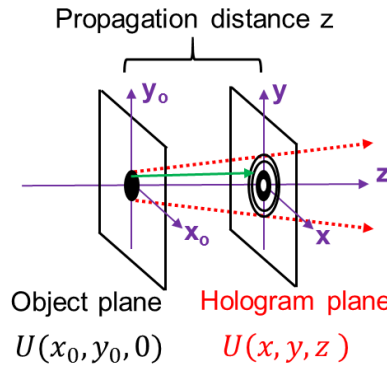


Figure 4.1: Sketch of the scalar diffraction theory.

4.2.2 Hologram formation and numerical reconstruction

Hologram recording and numerical reconstruction are two steps for DIH processing. Hologram recording means the recording of the interference fringes (holograms) caused by the reference wave and the object wave using a digital camera sensor. Then, the reference wave is numerically reintroduced to illuminate the hologram to reconstruct the 3D optical object field, extracting the 3D information [128]. Mathematical descriptions of these two steps are expressed as follows. The hologram is formed by the superposition of the object wave and reference wave (**Figure 4.2**).

$$U_{holo} = |U_{obj}|^2 + |U_{ref}|^2 + U_{ref} \cdot U_{obj}^* + U_{ref}^* \cdot U_{obj} \quad (17)$$

where U_{holo} , U_{obj} , and U_{ref} are the hologram, object wave, and reference wave, respectively. U_{obj}^* , and U_{ref}^* represent the complex conjugate of U_{obj} and U_{ref} , respectively.

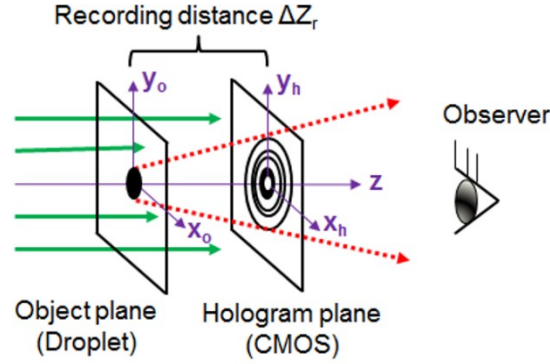


Figure 4.2: Sketch of the hologram formation.

The numerical reconstruction of hologram is conducted by introducing a reconstruction wave to illuminate the hologram (**Figure 4.3**).

$$\begin{aligned} U_{holo}^{rec} &= U_{ref} \cdot U_{holo} \\ &= U_{ref} \cdot |U_{ref}|^2 + U_{ref} \cdot |U_{obj}|^2 + U_{ref} \cdot U_{ref} \cdot U_{obj}^* + |U_{ref}|^2 \cdot U_{obj} \end{aligned} \quad (18)$$

where U_{holo}^{rec} is the reconstructed hologram. $U_{ref} \cdot |U_{ref}|^2$ and $U_{ref} \cdot |U_{obj}|^2$ represent zeroth-order beam, $U_{ref} \cdot U_{ref} \cdot U_{obj}^*$ is the real image, and $|U_{ref}|^2 \cdot U_{obj}$ indicates the virtual image. The reconstruction wave is the same as the reference wave.

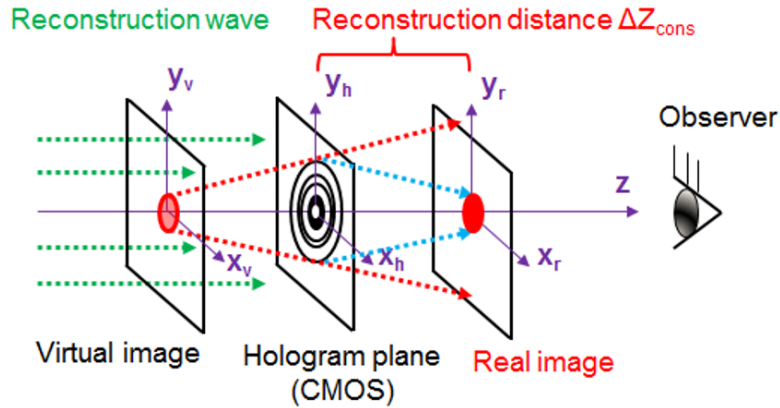


Figure 4.3: Sketch of the hologram numerical reconstruction.

4.2.3 Numerical reconstruction method

The angular spectrum method (ASM), also called the double Fourier transform method and the convolution approach, is a rigorous mathematical solution of scalar diffraction theory, which has been widely applied to model the wave propagation [129, 130]. This method considers the complex electromagnetic wave as a series of uniform infinite plane waves travelling in different directions, referred as the angular spectrum of the wave-field [131]. The key feature of this method is that wave propagation is described by the propagation of its spectrum [132]. Compared to other reconstruction methods (*e.g.*, Huygens convolution method and Fresnel transform method), ASM is considered to have the highest degree of accuracy because it requires neither the minimum reconstruction distance nor any assumptions (such as the Fresnel approximation) [133-135]. Therefore, ASM is preferred to numerically reconstruct the object in this work.

As introduced in the subchapter 4.2.1, the wave propagation can be described using the Fresnel-Kirchhoff diffraction formula (**Equation 16**). This formula can also be converted into the ASM equations using the Fourier transformation. The Fourier transformation is a powerful mathematical tool to describe and analyze periodic structures [125]. In the two-dimensional hologram plane the spatial coordinates (units: m) could be converted into the corresponding spatial frequencies (units:

1/m). The components of the scattering vector and their relationships to Fourier domain coordinates (u, v) can be expressed by the following equations [132]:

$$\vec{k} = \frac{2\pi}{\lambda} (\cos \phi \sin \theta, \sin \phi \sin \theta, \cos \theta) \quad (19)$$

and

$$\cos \phi \sin \theta = \lambda u \quad (20)$$

$$\sin \phi \sin \theta = \lambda v \quad (21)$$

respectively. Here, \vec{k} is the scattering vector from the point $(0,0,0)$ to the point (x_i, y_i, z_i) , as shown in **Figure 4.4**. The transformation from the Cartesian coordinate system to the spherical coordinate system is fulfilled using relationships:

$$\tan \theta = \frac{\sqrt{x_i^2 + y_i^2}}{z_i} \quad (23)$$

$$\cos \phi = \frac{x_i}{\sqrt{x_i^2 + y_i^2}} \quad (24)$$

$$r = \sqrt{x_i^2 + y_i^2 + z_i^2} \quad (25)$$

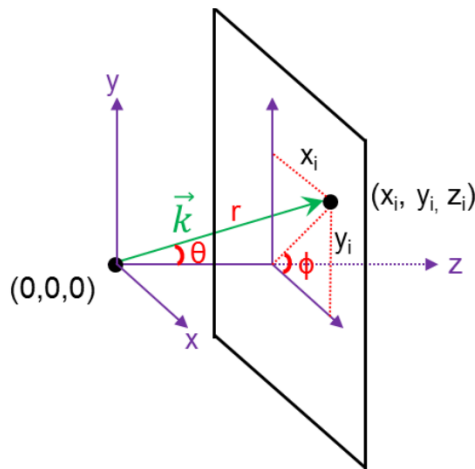


Figure 4.4: The conversion from the Cartesian coordinate (x_i, y_i, z_i) to the spherical coordinate (r, θ, ϕ) .

The Fresnel-Kirchhoff diffraction formula (**Equation 17**) can be converted in Fourier domain coordinates (u, v) using to above mentioned questions of **20-25**. Then, the wave propagation from the point $(x_0, y_0, 0)$ to the point (x, y, z) , *i.e.*, the hologram formation, can be expressed using the ASM as [106]:

$$U(x, y, z) = FFT_{2D}^{-1}\{FFT_{2D}\{U(x_0, y_0, 0)\} \cdot \Psi(u, v)\} \quad (26)$$

where, $U(x, y, z)$ and $U(x_0, y_0, 0)$ are the hologram and the object, respectively. FFT_{2D} and FFT_{2D}^{-1} represent the two-dimensional fast Fourier transform and the inverse two-dimensional fast Fourier transform, respectively. $\Psi(u, v)$ is the spatial frequency transfer function of propagation of light.

$$\Psi(u, v) = e^{(ikd\sqrt{1-(\lambda u)^2-(\lambda v)^2})} \quad (27)$$

where u and v are the spatial frequency of x and y , respectively. In addition, the wave propagation from the point (x, y, z) to the point $(x_0, y_0, 0)$, *i.e.*, the numerical reconstruction, can be expressed using the ASM in Fourier transforms as [106]:

$$U(x_0, y_0, 0) = FFT_{2D}^{-1}\{FFT_{2D}\{U(x, y, z)\} \cdot \Psi(u, v)^*\} \quad (28)$$

After the numerical reconstruction using the equation (21), the amplitude contrast image and phase contrast image of the object are obtained as:

$$I(x_0, y_0, 0) = |U(x_0, y_0, 0)|^2 \quad (29)$$

$$\phi(x_0, y_0, 0) = \arctan \left\{ \frac{Imag[U(x_0, y_0, 0)]}{Real[U(x_0, y_0, 0)]} \right\} \quad (30)$$

where $Imag[U(x_0, y_0, 0)]$ and $Real[U(x_0, y_0, 0)]$ are the imaginary part and the real part of the complex number $U(x_0, y_0, 0)$, respectively. Both the amplitude contrast image and phase contrast image could give the information of the objective including 3D location, size and morphology. The proceeds will be detailly explained in the **subchapter 4.4.1**.

4.3 Experimental setup and procedure

4.3.1 Setup construction

The experimental setup for digital in-line holography was constructed first in order to apply this technique on single droplet combustion. **Figure 4.5** shows the sketch and photos of the experimental setup for digital in-line holography, which mainly consists of one laser beam, three filters, the expanding and collimating lens system, and the recording system. The continuous-wave laser beam (Cobolt Samba, diode-pumped laser) has a maximum power of 110 mW and a wavelength of 532 nm. A neutral filter and a 532 nm bandpass filter were used in order to reduce the laser beam power and remove other wavelength lights from the environment, respectively. A spatial filter was employed to improve the uniform transverse intensity profile of the laser beam. The expanding and collimating lens system contains two convex lenses and two concave lenses, which expand and collimate the laser beam to a laser light sheet (Spherical cross section with a diameter of 14 mm). The recording system is composed of an objective (Mitutoyo 375-039 or Olympus SZ1145) and a high-speed camera (Phantom, camera model VEO 710L). The objective lenses can increase the magnification of the recording system, in order to detect small droplets (**Fig. 4.5 c**), which have an initial diameter of around 100 μm . The high-speed camera is for the purpose of recording the hologram images during the droplet combustion processes (**Fig. 4.5 d**), which have a short lifetime of less than 10 ms after ignition.

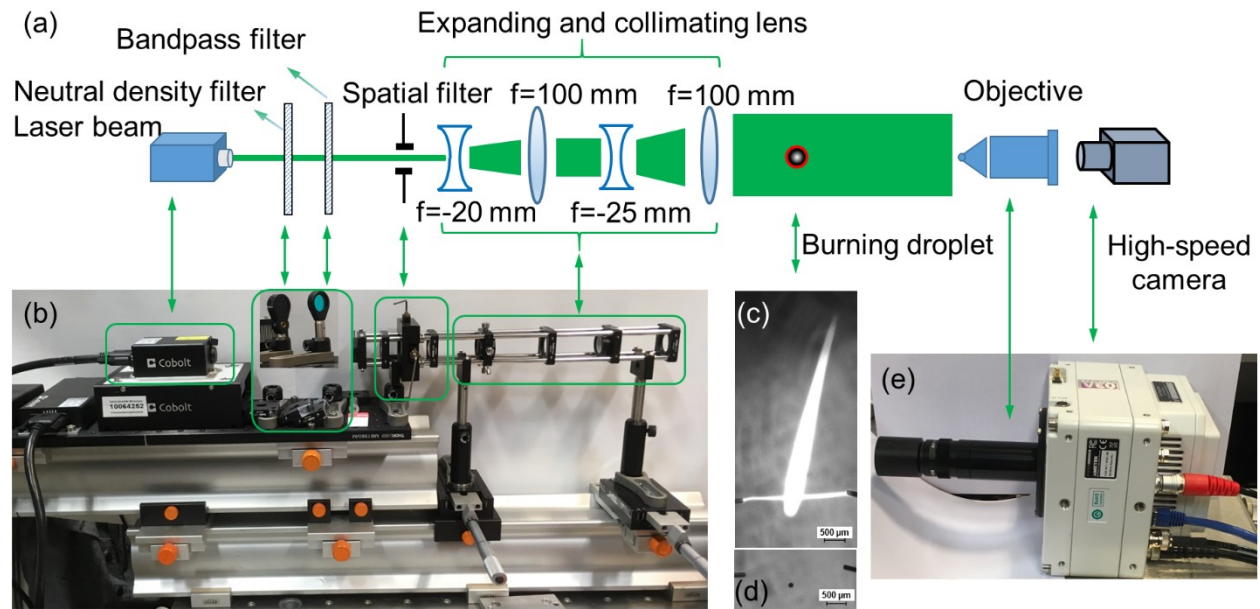


Figure 4.5: Sketch (a) and photos (b) of the experimental setup for digital in-line holography. It consists of a laser, optical filters, a beam expansion and collimating lens system, and the recording system. The holograms of burning droplet (c) and non-burning droplet (d) are recorded *via* the recording system (e).

4.3.2 Effective detector at the focal plane of the objective

In the experimental setup, one objective was installed in front of the high-speed camera in order to increase the lateral magnification of the recorded hologram images. Therefore, the effects of the objective on the recording distance and the magnification of the recorded hologram are necessary to be considered. The recording distance of the holography setup (without the objective) is calculated as the length from the sensor to the object. When one objective is mounted to the digital camera, the focal plane of the objective acts as a virtual recording plane (red dash line in **Fig. 4.6**), where the optical field is recorded by the digital camera sensor as the magnified hologram [136]. The hologram reconstruction can be conducted *via* propagating the plane wave through the recording distance from the virtual recording plane to the object plane [137]. In addition, the magnification of the hologram image is the same as that at the virtual plane, which can be measured by taking an image of a glass ruler at the focus plane.

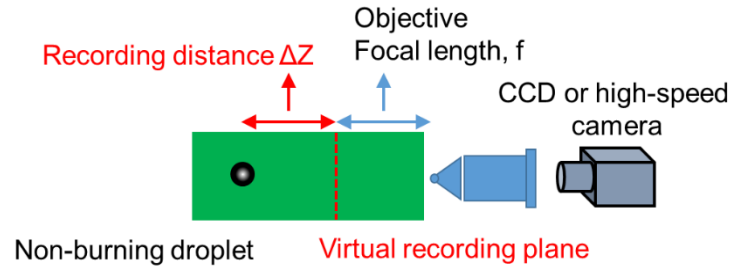


Figure 4.6: Sketch of the influence of the objective on the recording system. One effective detector (virtual recording plane) can be considered at the objective focal plane. The distance between the object and the effective detector is the recording distance.

4.3.3 Image processing

Figure 4.7 shows the pre-processing of hologram images. The raw images have background noise produced from the ambient light. The image without droplets was captured as the reference image. The raw images are subtracted by the reference image in order to filter the background noise. To reduce the time for analyzing images, only the area of interest was selected from the images after removing noise background. The selected image has the same center as the hologram. The horizontal and vertical density distributions through the center of the experimental hologram were extracted. Pre-processing of hologram images was conducted using Matlab scripts (**Appendix A3**).

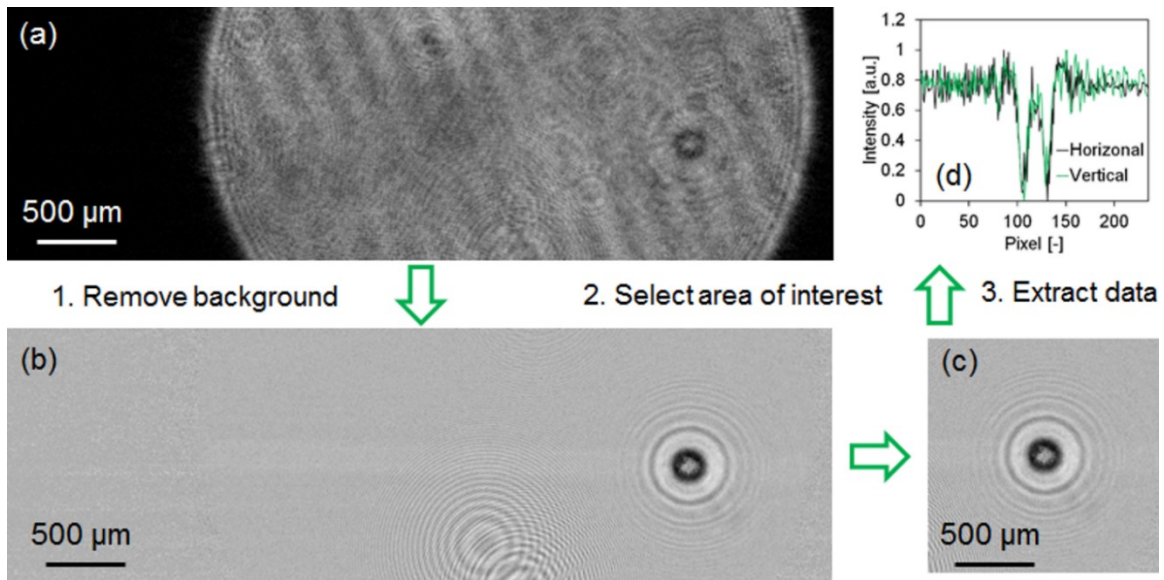


Figure 4.7: Processing of hologram images: (a) raw hologram, (b) hologram after removed background, (c) selected area of interest, and (d) extracted data. The image processing contains three steps: (1) Remove background from raw image, (2) Select area of interest from the removed background image, and (3) Extract data. In this figure, the raw hologram has a resolution of 832X256 pixel*pixel with a pixel size of 6.25 μm/pixel. The selected area of interest has a resolution of 235X235 pixel*pixel with the hologram signal in the center.

4.4 Results and discussion

This section introduces the results of holography measurements into two subsections:

- (1) The hologram formation and reconstruction of non-burning droplets (**Subchapter 4.4.1**).
The feasibility of droplet size and location measurements using the digital in-line holography is evaluated.
- (2) The experimental findings of hologram from burning droplets (**Subchapter 4.4.2**). The flame position above the droplet surface (flame standoff ratio) of single isolated burning droplets with micro-explosions is studied. The influences of the surrounding flame on hologram signals are identified.

4.4.1 The hologram formation and reconstruction of non-burning droplets

The hologram formation and reconstruction of non-burning droplets were performed to evaluate the feasibility of droplet size and location measurements using the digital in-line holography. Diffraction dominates scattering in the forward direction in digital in-line holography. Therefore, a 3D droplet can be considered as a 2D aperture or a 2D opaque disk [136, 138], which has a shape equal to the droplet cross section normal to the incident light (**Figure 4.8**). Hologram formation and numerical reconstruction of the cross section of a non-burning xylene droplet were simulated assuming the 3D non-burning droplet as a 2D aperture or a 2D opaque disk. The angular spectrum method was utilized to numerically reconstruct the cross section of a droplet from experiment and simulation.

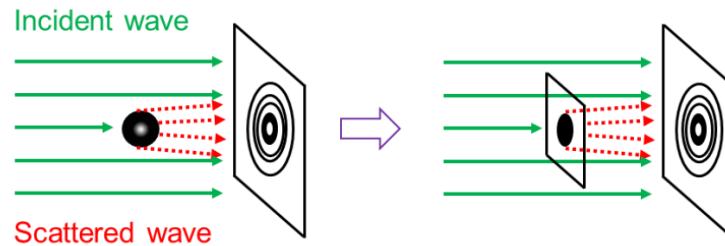


Figure 4.8: Digital in-line holography: diffraction dominated scattering. A 3D particle can be considered as a 2D aperture or opaque disk, with a shape equal to its cross section normal to the incident light.

To verify the following experimental studies, two sets of simulations on hologram formation and numerical reconstruction were carried out (**Table 4.1**). The first one is a spherical particle with a diameter of 120 μm at various recording distances from 5, 10, 20, 30, to 50 mm (**Figure 4.9**). The second set includes particles with various diameters from 70, 120, 170, 220, to 270 μm at a fixed recording distance of 30 mm (**Figure 4.10**). The constructed droplet images have clear boundaries (**Figure 4.9 b** and **Figure 4.10 b**), which have large intensity differences with the surrounding background (**Figure 4.9 d** and **Figure 4.10 d**). However, when the recording distance

used in numerical reconstruction (reconstruction distance) is not the same as the actual value, the boundaries of the reconstructed droplet images become blurry (**Figure 4.11**). This blurriness increases with the increasing distance to the focal plane. Therefore, this characteristic is used as an important criteria to evaluate the reconstruction results. The method to the blurriness values is shown in **Appendix A4**.

Table 4.1: Two sets of simulations on hologram formation and numerical reconstruction of nonburning droplets.

The first set			The second set		
Droplet diameter D (μm)	Recording Z (mm)	distance	Droplet diameter D (μm)	Recording Z (mm)	distance
120	5		70	30	
120	10		120	30	
120	20		170	30	
120	30		220	30	
120	50		270	30	

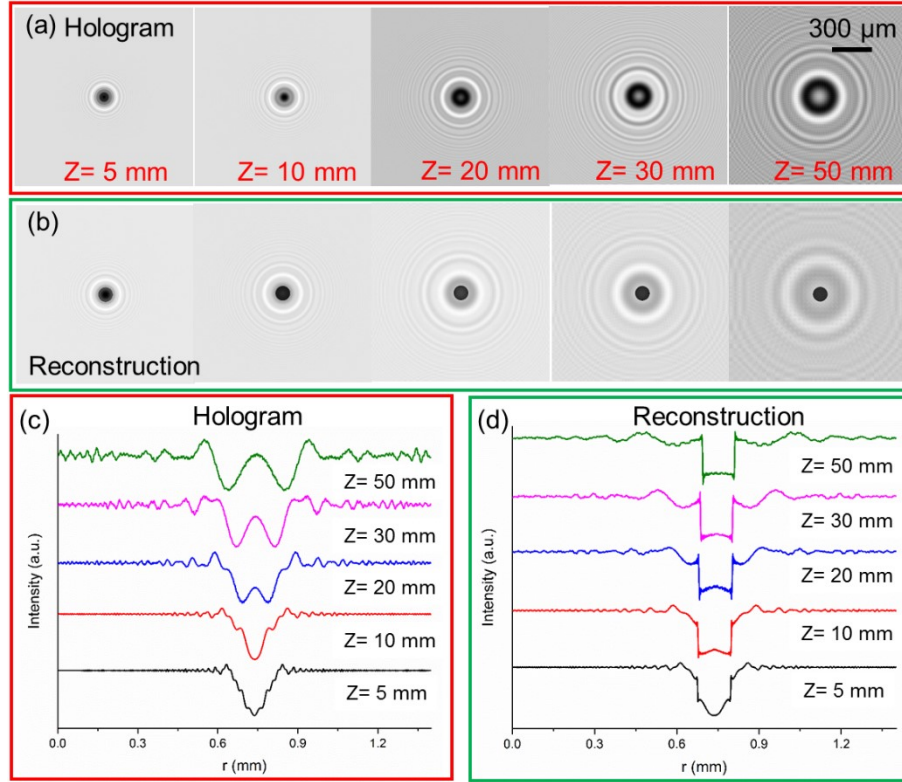


Figure 4.9: The simulation of a particle with a diameter of 120 μm at various recording distances from 5, 10, 20, 30, to 50 mm. (a) hologram formation, (b) numerical reconstruction, (c) density distribution horizontal through the center of the hologram, and (d) density distribution horizontal through the center of the reconstructed object. The images from hologram and reconstruction have a resolution of 235X235 pixel*pixel with a pixel size of 6.25 μm/pixel.

According to the previous work from Tyler and Thompson, a complete analytical description of the reconstructed field associated with a Fraunhofer hologram can be produced by considering the hologram as a new diffracting aperture of finite extent [139]. This analytical description can be used to describe the transmittance amplitude of a spherical object on the hologram with an incident plane wave [139, 140]:

$$I(r) = 1 - \frac{2\pi d^2}{\lambda z} \sin\left(\frac{\pi r^2}{\lambda z}\right) \left[\frac{2J_1(2\pi dr/(\lambda z))}{2\pi dr/(\lambda z)} \right] + \frac{\pi^2 d^4}{\lambda^2 z^2} \left[\frac{2J_1(2\pi dr/(\lambda z))}{2\pi dr/(\lambda z)} \right]^2 \quad (25)$$

where, d , λ , z , r , and J_1 are particle diameter, wavelength of incident light, recording distance, the distance to the center in the hologram plane, and first-order Bessel function, respectively.

The hologram of a spherical droplet contains a series of central symmetrical fringes (**Figure 4.9 a and b**), which are caused by the interference of light reaching on the hologram plate from different sources. The spatial frequency of these fringes [also called local fringe frequency, $f(r)$, fringes per unit distance], which is the inverse of the fringe spacing in the hologram, can be extracted from the derivative of the argument of the sine term in the **equation (25)** and then divided by 2π [139]:

$$f(r) = \frac{1}{2\pi} \cdot \frac{d\left(\frac{\pi r^2}{\lambda z}\right)}{dr} = \frac{r}{\lambda z} \quad (26)$$

The spatial frequency of fringes in hologram images in the two sets of simulations are listed in **Table 4.2**, which are calculated using the **equation (26)**. According to **the equation (26)**, it can be concluded that the spatial frequency of fringes is inversely proportional to the recording distance (z) and proportional to the distance to the center in the hologram plane (r) [106, 139]. This conclusion can be reflected in the simulated results from **Figure 4.9 c** and **Table 2**. In addition, the changes of particle diameters do not influence the spatial frequency as shown in **Figure 4.10 c** and **Table 2**.

Table 4.2: The spatial frequency of fringes in hologram images in the two sets of simulations on hologram formation and numerical reconstruction of nonburning droplets.

Droplet diameter D (μm)	Recording distance Z (mm)	Spatial frequency (1/mm) with the distance to the hologram center			
		r = 0.1 mm	r = 0.3 mm	r = 0.5 mm	r = 0.7 mm
120	5	37.59	112.78	187.97	263.16
120	10	18.80	56.39	93.98	131.58
120	20	9.40	28.20	46.99	65.79
120	30	6.27	18.80	31.33	43.86
120	50	3.76	11.28	18.80	26.32
70	30	6.27	18.80	31.33	43.86
120	30	6.27	18.80	31.33	43.86
170	30	6.27	18.80	31.33	43.86
220	30	6.27	18.80	31.33	43.86
270	30	6.27	18.80	31.33	43.86

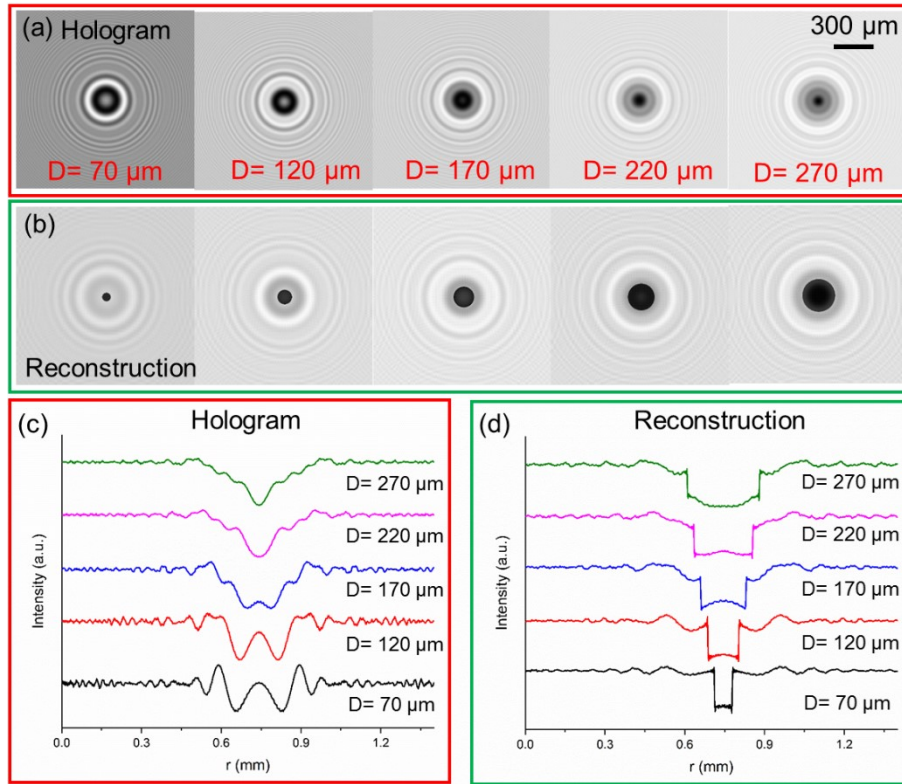


Figure 4.10: The simulation of particles with various diameters from 70, 120, 170, 220, to 270 μm at a fixed recording distance of 30 mm. (a) hologram formation, (b) numerical reconstruction, (c) density distribution horizontal through the center of the hologram, and (d) density distribution horizontal through the center of the reconstructed object. The images from hologram and reconstruction have a resolution of 235X235 pixel*pixel with a pixel size of 6.25 μm/pixel.

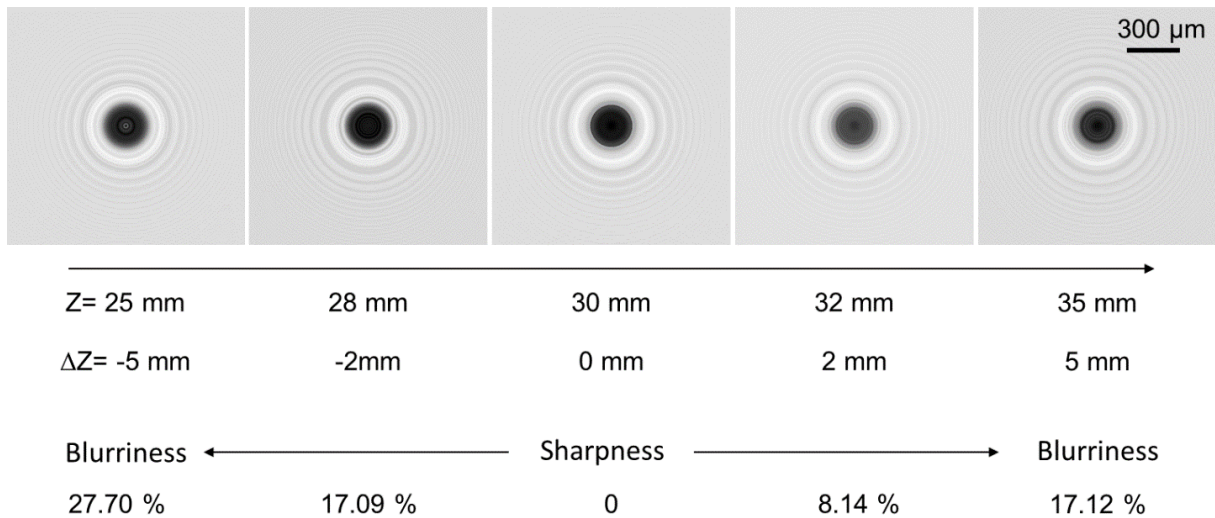


Figure 4.11: Numerical reconstruction of one particle with the diameter of $240 \mu\text{m}$ and the recording distance of 30 mm . From left to right, the reconstruction distances used in numerical reconstruction increase from $25, 28, 30, 32$ to 35 mm . The blurriness of reconstructed image increases with the increasing distance to the focal plane.

The droplet diameters can be obtained from the reconstructed images using a Matlab script. The Matlab script is designed to detect edges in intensity image using the sensitivity threshold method of canny (canny edge detection). Canny edge detection is a popular edge detection algorithm, which was developed by John F. Canny in 1986 [141]. This image edge detection technique is really useful for extracting important structural information in an image [142]. Particle diameters obtained from numerical reconstruction have small deviations ($< 2.8\%$) compared to input particle diameters (**Table 4.3**), demonstrating the feasibility of applying this method to measure sizes and locations of non-burning droplets.

Table 4.3: Particle diameters obtained from numerical reconstruction and their deviation compared to input particle diameter.

Recording distance Z (mm)	Diameter from Canny D_{canny} (μm)	Input diameter D_{input} (μm)	Deviation (μm)
5	121.24	120	1.24
10	122.99	120	2.99
20	120.47	120	0.47
30	120.42	120	0.42
50	120.42	120	0.42
30	71.97	70	1.97
30	122.31	120	2.31
30	172.48	170	2.48
30	222.41	220	2.41
30	272.42	270	2.42

The comparison between experiment and simulation was done on a non-burning xylene droplet with a diameter of 120 μm and a recording distance of 30 mm. The horizontal and vertical density distributions through the center of the experimental hologram fit well with that of the simulated hologram (**Figure 4.12 c**). The horizontal and vertical density distributions through the center of the reconstructed image from experiment fit well with that from simulation (**Figure 4.13 c**). The reconstructed droplet diameters obtained from experiment and simulation are 122 μm , which is almost the same as the measured droplet diameter using a high-resolution CCD camera (**Figure 4.14**).

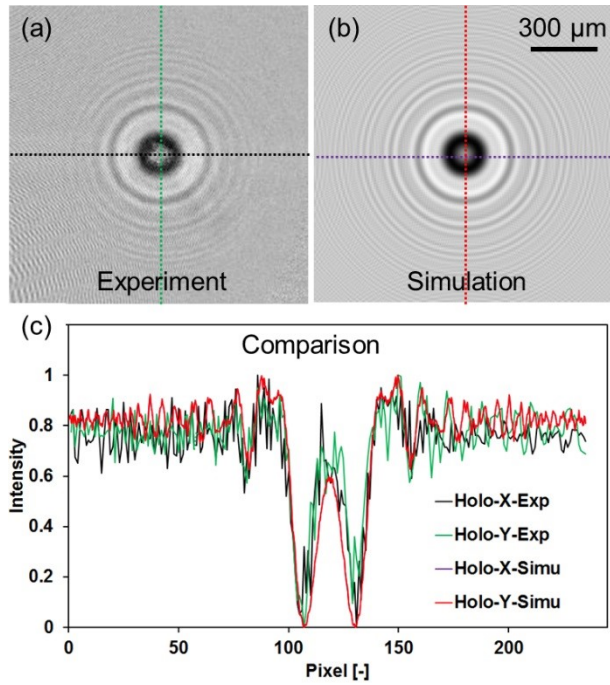


Figure 4.12: Hologram images from experiment (a) and simulation (b), and their intensity distribution comparison (c).

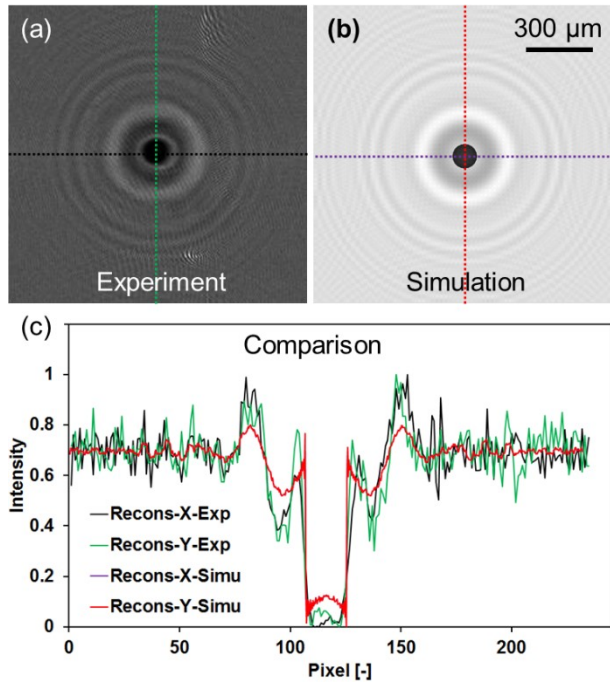


Figure 4.13: Reconstructed images from experiment (a) and simulation (b), and their intensity distribution comparison (c).

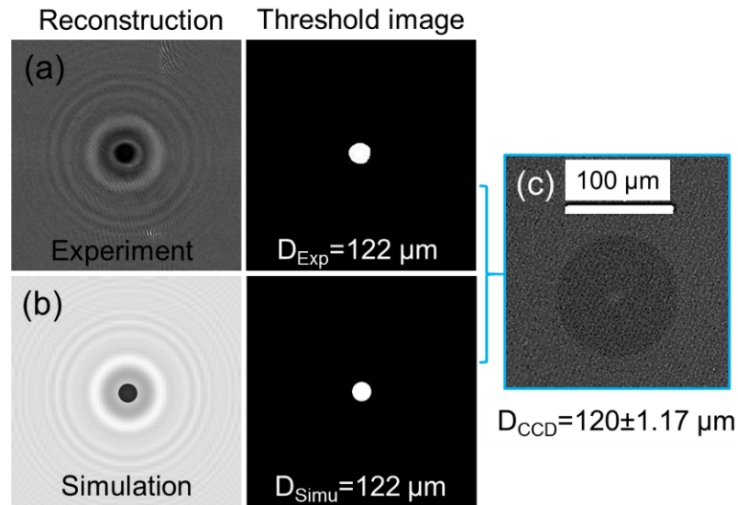


Figure 4.14: Reconstructed images (left column) and threshold images (middle column) from experiment (a) and simulation (b), as well as the droplet image captured by a high-resolution CCD camera (c). Obtained values of droplet diameters: $D_{Exp}=D_{Simu}=122 \mu m$. $D_{CCD}=120 \pm 1.17 \mu m$ (CCD camera, 1 pixel=1.17 μm).

4.4.2 The preliminary holographic measurements of burning droplets

The aim of applying digital in-line holography technique on single droplet combustion is to estimate the refractive index gradient from the droplet surface to the flame front. To achieve this, the effect of the surrounding refractive index gradient on hologram is studied first. Next, the holography measurements on single droplet combustion of pure xylene and 0.5 mol/L Tin (II) 2-ethylhexanoate dissolved in xylene (abbreviated as Tin 2-EHA/Xylene) are performed, because these two kinds of solutions have been investigated in detail [30, 38]. In the previous work, the interferometric particle imaging (IPI) technique and the standard rainbow refractometry (SRR) technique were used to measure sizes and rainbow patterns of the burning droplets of Tin (II) 2-EHA/Xylene. The mass and heat transfer inside the burning droplets (**Figure 2.14 in chapter 2**) were estimated using a multicomponent diffusion limited model [30]. In addition, the chemical stability and the vaporization behaviors of Tin (II) 2-EHA/Xylene solutions were studied using attenuated total reflection Fourier transform infrared (ATR-FTIR) spectroscopy and

thermogravimetric analysis (TGA), respectively. Droplet micro-explosions are observed using the high-speed imaging technique in the single droplet combustion experiments, and the time from ignition to explosion decreases with the increasing precursor concentration. The SnO₂ nanoparticles obtained from FSP and single droplet combustion using the same metal-organic solutions exhibit similar size and crystallization. The particles produced from single droplet combustion reveal two types of nanoparticles with different size distributions and morphologies and thus two nanoparticle formation paths (**Figure 4.15**) during single droplet combustion are proposed. [38].

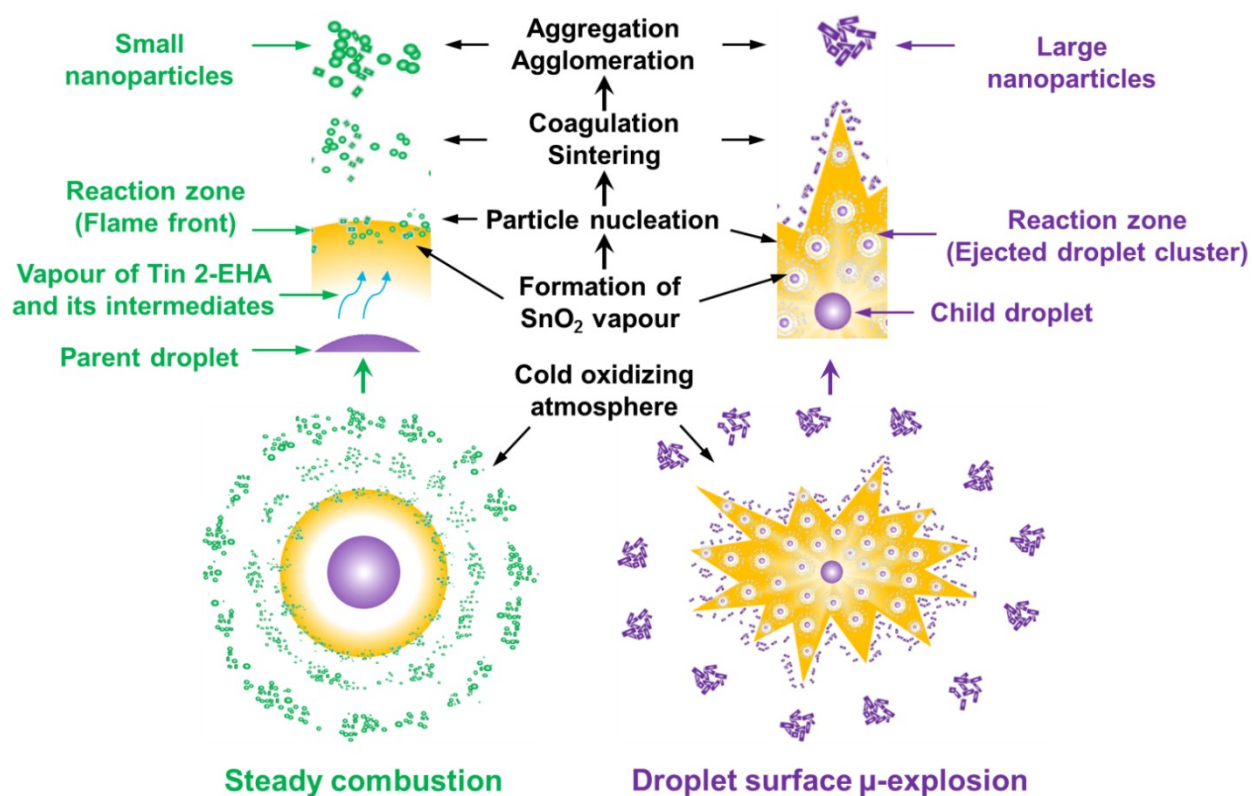


Figure 4.15: Schematic illustration of the two nanoparticle formation paths during single droplet combustion of Tin 2-EHA/Xylene: steady combustion (left) and droplet surface μ -explosion (right). This figure is adapted and reprinted with the permission from Ref. [38].

High-speed camera imaging on single droplet combustion of pure xylene and 0.5 mol/L Tin 2-EHA/Xylene was first performed to provide references and baselines for the holographic

measurements of the reproducible single droplet combustion (**Figure 4.16**). Flame standoff ratio (the ratio of flame diameter to droplet diameter) is commonly employed to characterize the luminous flame position above the droplet surface. To the best of my knowledge, for the first time the flame standoff ratio of single isolated burning droplets with micro-explosions was detected using the high-speed camera imaging technique (**Figure 4.16 a**, red points). The flame standoff ratios of pure xylene and 0.5 mol/L Tin 2-EHA/Xylene fit well with each other during the period from droplet ignition to the largest flame (from 0 to 1.8 ms in **Figure 4.16 a**). This indicates that during this period the high-volatility solvent dominates surface evaporation of the precursor solution droplet and this solvent mainly takes part in the reaction in the flame front. During multicomponent droplet combustion, flame shrinkage (or flame contraction) occurs owing to the composition change at the droplet surface [143]. Flame shrinkage was also observed during droplet disruptive combustion of precursor solutions. For example, during single droplet combustion of 0.5 mol/L Tin 2-EHA/Xylene, its flame standoff and flame diameter suddenly decrease from 2.1 ms to 2.8 ms compared to pure xylene droplet (The flame shrinkage is marked in **Figure 4.16**, a and b). This indicates the process of viscous shell formation in the droplet surface as well as the resulting hindrance of fuel evaporation at the droplet surface. Flame shrinkage leads to reheating of the droplet surface and thermal decomposition of metal-organic precursor, which induces viscous shell formation, heterogeneous vapor nucleation and subsequent droplet micro-explosion [38].

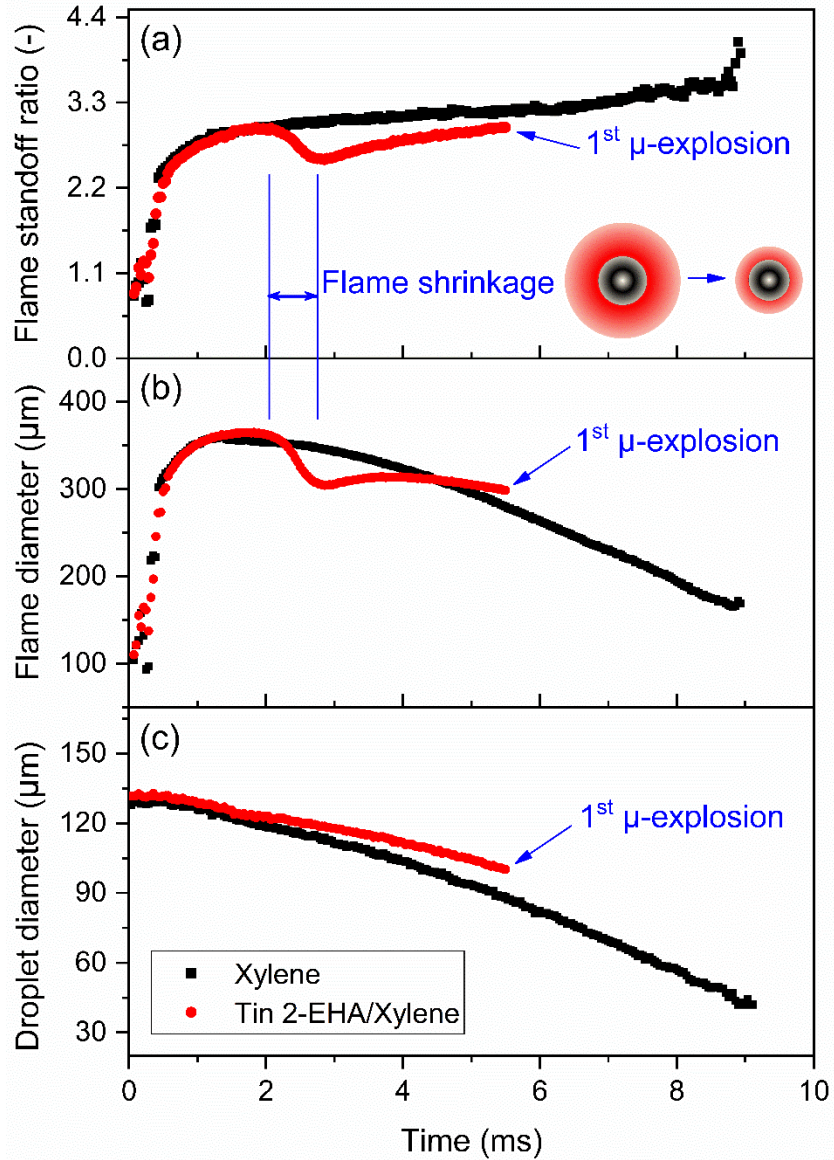


Figure 4.16: Comparisons between single droplet combustion of xylene and 0.5 mol/L Tin 2-EHA/Xylene: (a) flame standoff ratio, (b) flame diameter and (c) droplet diameter. The flame shrinkage is marked using two blue vertical lines and is also expressed using two small sketches.

Depending on the evolutions of the flame diameter and the flame standoff ratio, four instances were selected during single droplet combustion of xylene and 0.5 mol/L Tin 2-EHA/Xylene: ignition, largest flame, shrinkage (The minimum point of flame diameter before explosion), and just before the first explosion. The information including relative time, droplet diameter, flame diameter, and

flame standoff ratio of these four instances are listed in **Table 4.4**. The droplet frames, flame frames and hologram frames at these four instances were captured from single droplet combustion experiments of xylene (**Figure 4.17**) and 0.5 mol/L Tin 2-EHA/Xylene (**Figure 4.18**). The hologram signals of spherical droplets are centrally symmetrical, and thus the horizontal density distributions from the center of the hologram frames were extracted for comparisons (**Figure 4.19**). At the ignition moment, droplets need time to absorb heat produced from the spark and thus the flames are not yet formed (**Figure 4.17** and **Figure 4.18**, the first columns). In addition, the hologram signals (**Figure 4.19**, the first row) are almost the same for both 0.5 mol/L Tin 2-EHA/Xylene droplet and xylene droplet. At the largest flame point, the flame shape and brightness (**Figure 4.17** and **Figure 4.18**, the second columns), and hologram signal (**Figure 4.19**, the second row) are almost the same for both 0.5 mol/L Tin 2-EHA/Xylene droplet and xylene droplet. The well-fitting of hologram signals during the period from ignition to the largest flame demonstrate again that 0.5 mol/L Tin 2-EHA/Xylene droplet and xylene droplet have similar combustion processes. At the shrinkage instance, the flame standoff (**Figure 4.16 a**) and the flame brightness (**Figure 4.17** and **Figure 4.18**, the third columns) of 0.5 mol/L Tin 2-EHA/Xylene are lower than that of xylene.

Table 4.4: Droplet diameter, flame diameter and flame standoff ratio of the selected four instances during single droplet combustion of xylene and 0.5 mol/L Tin 2-EHA/Xylene.

Solution		Xylene			0.5 mol/L Tin 2-EHA/Xylene	
Selected instances	Description	Relative time (ms)	Droplet/Flame diameter (μm)	Flame standoff ratio	Droplet/Flame diameter (μm)	Flame standoff ratio
Time1 (t1)	Ignition	0	129/N.A.	N.A.	132/N.A.	N.A.
Time2 (t2)	Largest flame	1.86	120/354	2.95	122/364	2.98
Time3 (t3)	Shrinkage	2.86	114/346	3.04	119/304	2.55
Time4 (t4)	Before 1st explosion	5.5	88/280	3.18	100/299	2.99

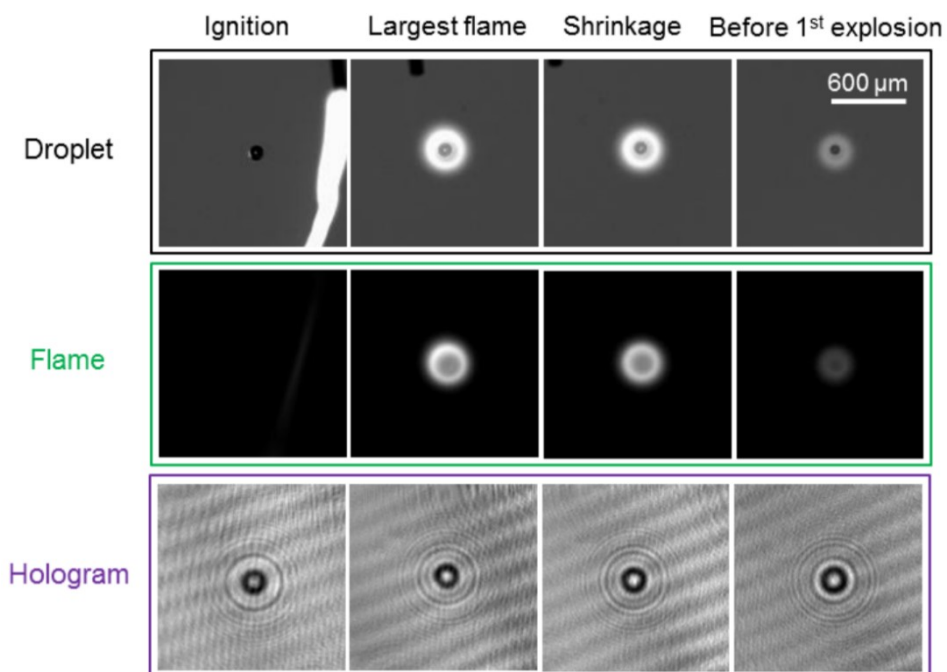


Figure 4.17: Frames of droplet (top arrow), flame (middle arrow), and hologram (bottom arrow) of the selected four instances during single droplet combustion of xylene.

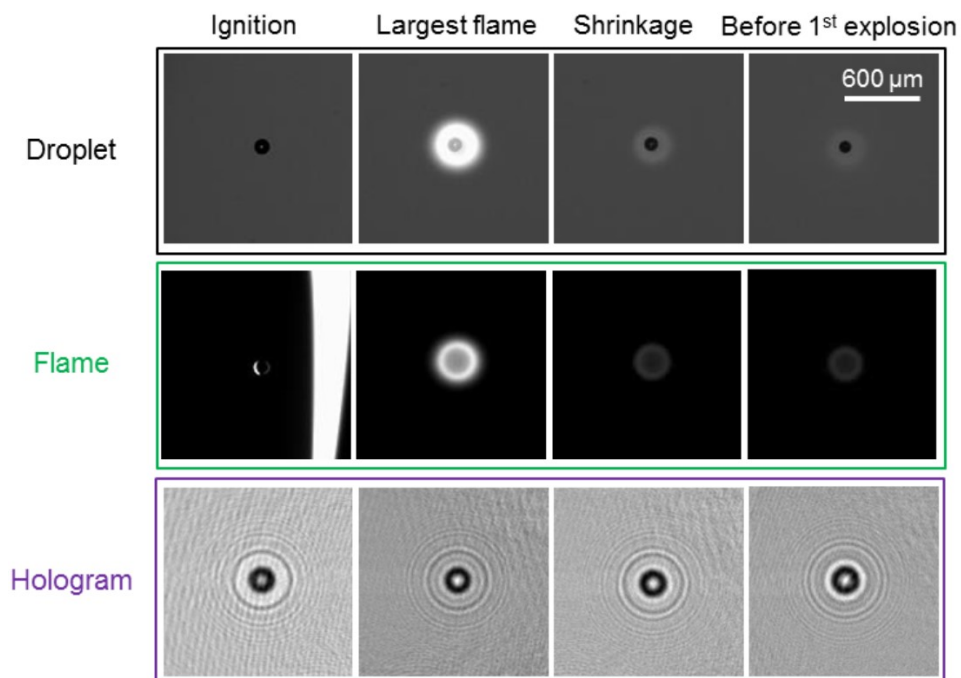


Figure 4.18: Frames of droplet (top arrow), flame (middle arrow), and hologram (bottom arrow) of the selected four instances during single droplet combustion of 0.5 mol/L Tin 2-EHA/Xylene.

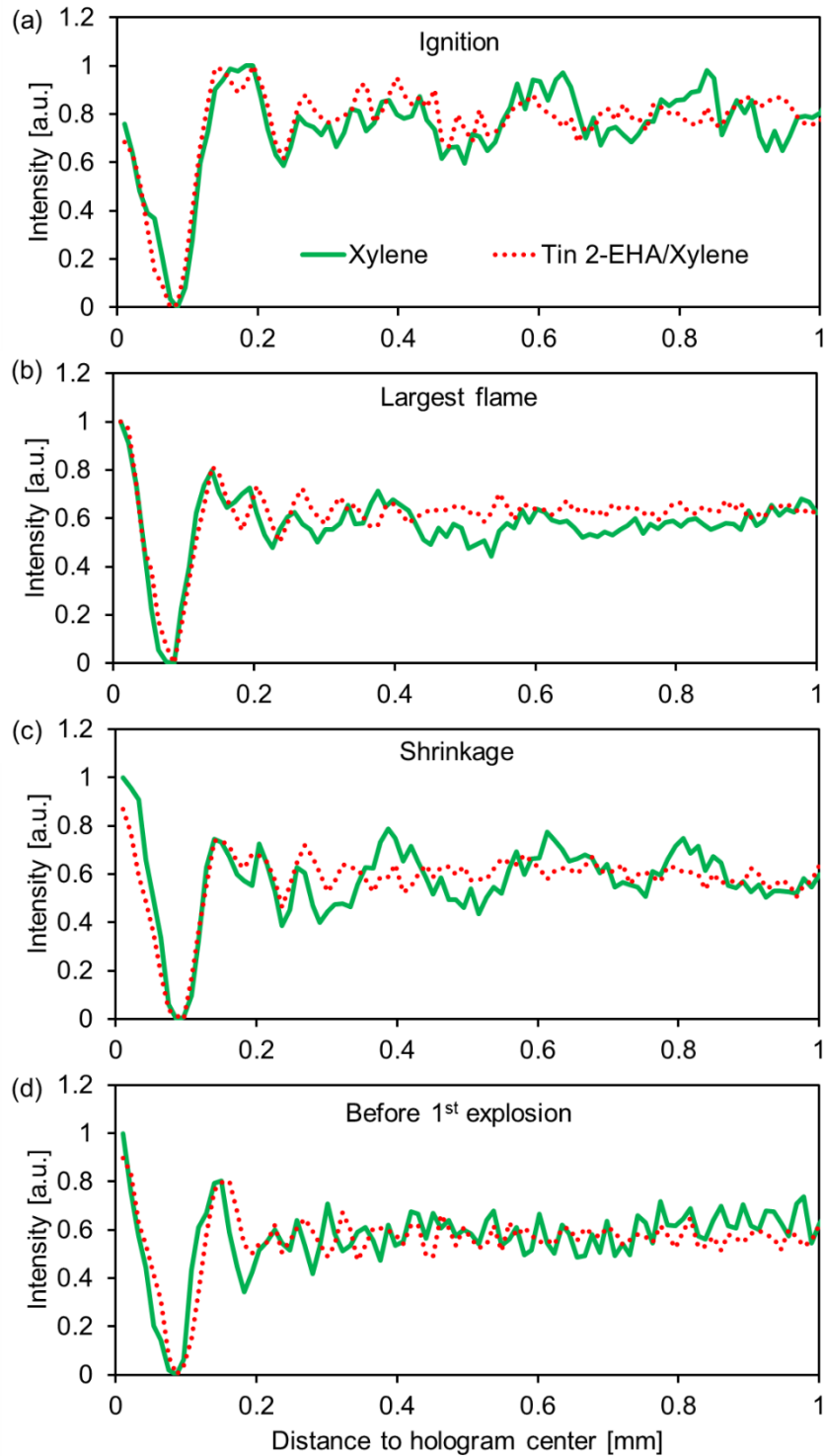


Figure 4.19: Hologram signals of the selected four instances during single droplet combustion of xylene (green solid curve) and 0.5 mol/L Tin 2-EHA/Xylene (red dash curve): (a) ignition, (b) largest flame, (c) shrinkage, and (d) just before the first explosion.

A new finding was observed for the hologram signals of burning droplets, *i.g.*, the hologram central fringe of droplets with a surrounding flame has a higher intensity (brightness) than droplets without a surrounding flame (**Figure 4.19**). It is assumed that a decreasing refractive index gradient exists from droplet surface to flame front, which acts as a special “lens” influencing the light scattering and/or diffraction measured with holography. A similar phenomenon was also observed for fast evaporating droplets, which are surrounded by air/vapor mixtures with refractive index gradients. The surrounding refractive index gradients deflect the light and hence lead to the unusually brightness of central fringes of droplet holograms [144-146].

At the two moments of shrinkage and just before the first explosion, the central fringes of xylene droplet have higher brightness than 0.5 mol/L Tin 2-EHA/Xylene droplet. This is caused by the difference of flame sizes as well as the difference of flame brightness. At these two moments, xylene flames have large size and strong brightness, which result in a greater (steeper) refractive index gradient and thus promote the brightness of central fringes [144].

4.5 Summary and conclusions

4.5.1 Summary

- (1) An experimental setup of digital in-line holography was constructed, and the methods for hologram formation and numerical reconstruction were developed. The effects of droplet diameter and recording distance on the formation of holograms were investigated using simulations. Holography measurements were performed on non-burning and burning droplets
- (2) The hologram of spherical droplet is a series of rings (or named as fringes), which are central symmetrical. The ring spatial frequency is inversely proportional to the recording distance.

- (3) The refractive index gradient surrounding the burning droplet makes the hologram center fringe bright. This kind of change can be used to verify the multilayered sphere model, which will involve the surrounding refractive index gradient.

4.5.2 Conclusions

- (1) To determine the influence of the surrounding flame on hologram signals, the digital in-line holography technique and the high-speed camera imaging technique are used. The unusual brightness of the hologram center fringe is caused by the refractive index gradient surrounding the burning droplet. This finding could be used to provide experimental validations for simulating the refractive index gradient surrounding burning droplets.
- (2) For the first time the luminous flame position above the droplet surface (flame standoff ratio) of single isolated burning droplets with micro-explosions was measured. The evolution of flame standoff ratio of precursor solution supports the proposed droplet micro-explosion mechanism.

5 Outlook

5.1 Single droplet combustion and FSP synthesis of iron oxide nanoparticles

- (1) For the precursor-solvent combination of dissolving Iron (III) nitrate nonahydrate into the mixture of ethanol and 2-ethylhexanoic, searching the lowest amount of 2-ethylhexanoic acid and other low-cost organic acids, which could result in the homogeneous iron oxide nanoparticle formation, are needed for reducing the cost of precursors and solvents in industrial production.
- (2) Single droplet combustion experiments consume a small amount of precursor solution (around 5 mL per experiment) compared to the production using lab-scale and pilot reactors. Therefore, this method will be an economic pre-testing to screen various precursor-solvent systems for desired nanoparticles for large-scale productions. For example, metal acetates, metal nitrates and metal carbonates are low-cost inorganic precursors, which could be tested first using single droplet combustion experiments to select the appropriate precursor-solvent system.
- (3) Nano-scale and molecular-scale approaches are proposed to further unravel the mechanisms of the particle generation and surface micro-explosions. These information include structure, density, and thickness of the shell, as well as the early particle formation during the steady droplet combustion and droplet surface micro-explosions.

5.2 Three-dimensional measurements of double droplet combustion

- (1) The current double droplet generator could only support the strong interaction between two burning droplets for a short period, which makes the investigation on droplet explosions challenging. Therefore, increasing the interaction time is needed, which could be reached using more burning droplets or decreasing the oxygen concentration in the atmosphere.

(2) Comparison of nanoparticle morphology and size from single droplet combustion and double droplet combustion are expected after improving the generator for reproducible and stable double droplet generation.

(3) In FSP, the dispersed droplets burn initially in the pure oxygen and then in a complexed atmosphere considering entrainments of air and product. Thus, the investigation of ambience compositions, e.g., oxygen composition and water vapor, on droplet combustion behaviors and nanoparticle formations are expected.

5.3 Digital in-line holography of single droplet combustion

(1) The extension from in-line holography to off-line holography is expected by modifying the experimental setup. Off-line holography is strong on detecting phase changes of object waves and thus is suitable to measure the refractive index (temperature) gradient inside the burning droplet.

(2) The experimental measurements on double droplet combustion are expected to detect the three-dimensional information including droplet size, location, and velocity.

(3) Building up a multilayered sphere model to simulate and estimate the refractive index gradient surrounding the burning droplet is needed.

5.3.1 The proposed method to estimate the surrounding refractive index gradient

As introduced in the **subchapter 4.4.2**, the refractive index gradient surrounding the burning droplet causes the hologram central fringe bright. This experimental finding could be used to estimate the refractive gradient surrounding the droplet. Marié and his coworkers used Generalized Lorenz-Mie theory for a multilayered sphere to simulate holograms of fast evaporating droplets, demonstrating the influence of the surrounding refractive index gradients on hologram formation [144]. Their work has proven the feasibility of using DIH to estimate the refractive index gradients surrounding the fast evaporating droplets.

The burning and/or fast evaporating droplet with surrounding refractive index gradients, showing spherical symmetry structure (e.g., shape, component and refractive index), can be considered as a multilayered sphere. The concentric layers from droplet center to ambient atmosphere can represent the refractive index gradients inside the droplet and the surrounding atmosphere. Therefore, this kind of multilayered sphere model is ideal to simulate the scattering of electromagnetic radiation of particles with core-shell structures and droplets with radially stratified structures [147]. Aden and Kerker first developed such a model to investigate the scattering of plane electromagnetic waves from two concentric spheres [148]. Wait generated a recursive algorithm based on Lorenz-Mie theory to calculate the electromagnetic scattering from a radially inhomogeneous sphere [149]. Bhandari proposed a calculation procedure for the complete set of scattering coefficients to describe the fields within the different regions of a multilayered sphere [150]. Wu and Wang developed a computing procedure using more stable and accurate recursing equations to calculate scattering coefficients of a multilayered sphere [151]. Then, Wu and his co-workers improved their algorithm for computing the scattering coefficients of plane waves and shaped beams by multilayered spheres, which has also been used to study the sensitivity of the main rainbow signal to the radial varying refractive index [152]. Kai and Massoli developed a finely stratified sphere model to calculate the internal and scattered fields, which can be used in analyzing the scattering by spheres with continuous-profile refractive indexes [153]. Yang has developed an improved recurrence algorithm using Mie theory, in order to circumvent numerical difficulties (e.g., layer number limitation, absorption and complicated calculation) in previous models [147]. Li *et al.* proposed efficient and stable algorithms to derive the Debye series decomposition for light scattering by plane waves and Gaussian beam from multilayered spheres, which have been successfully applied in simulating rainbow signals [154, 155]. The previous model, simulation, and experimental work have proved the ability of using the multilayered sphere model to obtain the electromagnetic scattering. From the experimental holograms, the influence of surrounding refractive index gradient on intensity distribution can be measured. It can be used

to verify the Mie-scattering model, which will involve the surrounding refractive index gradient. Therefore, developing one multilayered sphere model using Lorenz-Mie theory and/or Generalized Lorenz-Mie theory is expected to calculate the light scattering from the burning droplet with the radial refractive index gradient, and to further simulate the responsible hologram images in the future.

The multilayered sphere model could be developed by building up four groups of layers from the droplet center to the oxidizing atmosphere (**Figure 5.1**): (1) The first group of layers from droplet center to droplet surface. The refractive index gradient inside the droplet has no effect on the formed hologram [144], and thus can be assumed as a constant value here. (2) The second group of layers from the droplet surface to the flame front; (3) The second group of layers from the flame front to the oxidizing atmosphere; and (4) The fourth group of layers representing the oxidizing atmosphere. The refractive index gradient existing in each group is represented by the radially layers with constant refractive indexes (**Figure 5.2**).

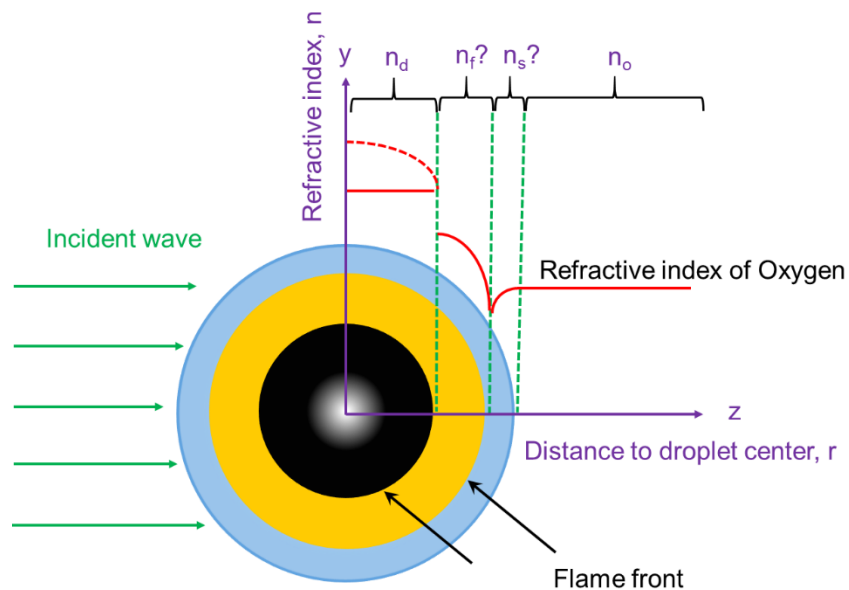


Figure 5.1: Sketch of the refractive index gradient surrounding the burning droplet. Here, n_d represents the refractive index of the droplet, n_f means the decreasing refractive index gradient

from droplet surface to flame front, n_s is the increasing refractive index gradient from flame front to the oxidizing atmosphere, and n_o indicates the refractive index of the oxidizing atmosphere.

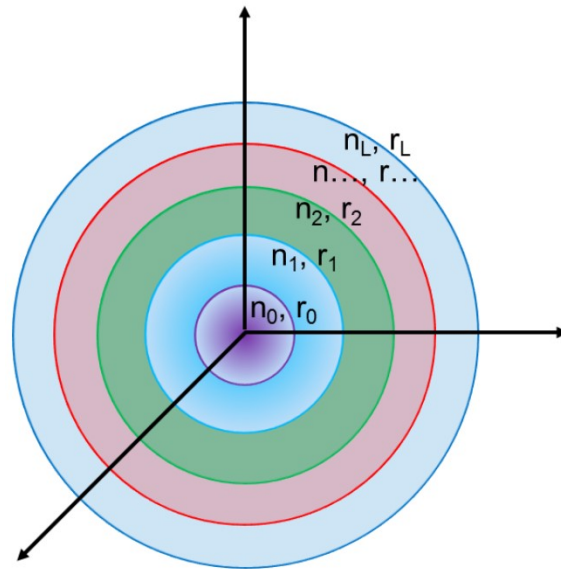


Figure 5.2: Sketch of the multilayered sphere model. The sphere contains of L layers from center to surface. Each layer has its own refractive index and radius. For example, the second layer has a refractive index of n_2 and a radius of r_2 . Here the radius of each layer means its outer radius. The inner radius of each layer is equal to the outer radius of the layer it enveloped. For example, the inner radius of the third layer is equal to the outer radius of the second layer.

Appendix

A.1 Precursor-solvent combinations used in single droplet combustion experiments

Table A.1: The precursor-solvent combinations during which single droplet combustion experiments μ -explosions were observed.

Precursor	Solvent	Explosion type	Particle size and morphology	Reference
Tin (II) 2-ethylhexanoate	Xylene	Surface explosion, no residual	Nano, homogeneous	[31]
Ce (III) 2-ethylhexanoate		Surface explosion, no residual	Not available (N.A.)	
Cr (III) 2-ethylhexanoate		Surface explosion, no residual	N.A.	
Zinc naphthenate	Ethanol	Surface explosion, no residual	Nano, homogeneous	[33]
	Xylene	Surface explosion, no residual	Nano, homogeneous	
Iron (III) nitrate nonahydrate	Ethanol+xylene+diethyleneglycol monobutylether(DEGBE)+2-ethylhexanoic acid (2-EHA) (1:1:1:1 volume ratio)	Surface explosion, no residual	Nano, homogeneous	
Aluminum (III) nitrate nonahydrate		Surface explosion, no residual	Nano, homogeneous	
Titanium tetraisopropoxide (TTIP)	Xylene	Surface explosion, no residual	Nano, homogeneous	[28]
	Ethanol	Puffing, surface explosion, no residual	Nano, homogeneous	
	Ethanol+xylene (1:1 volume ratio)	Surface explosion, no residual	Nano, homogeneous	
Lithium nitrate+ Titanium tetraisopropoxide (TTIP)	Ethanol+EHA	Puffing, surface explosion, no residual	Nano, homogeneous	[6]
	Ethanol	Puffing, residual	Nano+micro	
	Benzyl alcohol (BnOH)	Surface explosion, no residual	N.A.	
	BnOH+EHA	Surface explosion, no residual	N.A.	
Iron (II) naphthenate	p-Xylene	Surface explosion, no residual	Nano, homogeneous	Unpublished work

Iron (III) acetylacetonate		Surface explosion, no residual	Nano, homogeneous
Iron (III) nitrate nonahydrate	Ethanol+EHA (1:1 volume ratio)	Surface explosion, no residual	Nano, homogeneous
Manganese naphthenate	Xylene	Surface explosion, no residual	N.A.
Manganese naphthenate+Lithium acetylacetonate	Xylene+EHA	Surface explosion, no residual	N.A.
	Benzyl alcohol+EHA	Surface explosion, no residual	N.A.
Manganese naphthenate+Lithium tert-butoxide	Xylene+EHA	Surface explosion, no residual	N.A.
	Benzyl alcohol+EHA	Surface explosion, no residual	N.A.
Hexamethyldisiloxane (HMDSO)	Xylene	Puffing, residual	Nano, homogeneous
	Ethanol+xylene (1:1 volume ratio)	Puffing, no residual	Nano, homogeneous

Table A.2: The precursor-solvent combinations during which single droplet combustion experiments μ -explosions were not observed.

Precursor	Solvent	End of combustion	Particle size and morphology	Reference
Zinc nitrate hexahydrate	Ethanol	Residual	Nano+micro	[31]
Iron (III) nitrate nonahydrate	Ethanol	Residual	Nano+micro	Unpublished
Hexamethyldisiloxane (HMDSO)	Ethanol	Residual, no explosion	Nano, homogeneous	
Tetraethyl orthosilicate (TEOS)	Xylene	No residual, no explosion	Nano, homogeneous	
	Ethanol+Xylene (1:1 volume ratio)	No residual, no explosion	Nano, homogeneous	
	Ethanol	Residual, no explosion	Nano, homogeneous	

Table A.3: Properties of precursors and solvents used in single droplet combustion.

Precursor or solvent	Formula	Boiling point (°C)	Limit of superheat (°C)	Critical point (°C)	Solubility in Water, (mass%, at 25°C)
Ethanol	C ₂ H ₆ O	78	214	241	Miscible
Water	H ₂ O	100	333	374	N.A.
Hexamethyldisiloxane (HMDSO)	C ₆ H ₁₈ OSi ₂	100-101	219	243	Insoluble
Iron (III) nitrate nonahydrate	Fe(NO ₃) ₃ •9H ₂ O	125	N.A.	N.A.	150 g/100 mL
Zinc nitrate hexahydrate	Zn(NO ₃) ₂ •6H ₂ O	~125	N.A.	N.A.	184.3 g/100 ml, 20 °C
Xylene	C ₈ H ₁₀	139	306	344	Insoluble
Aluminum (III) nitrate nonahydrate	Al(NO ₃) ₃ •9H ₂ O	150, decomposes	N.A.	N.A.	67.3 g/100 mL
Tetraethyl orthosilicate (TEOS)	C ₈ H ₂₀ O ₄ Si	168	295	332	Reacts with water
2-ethylhexanoic acid (2-EHA)	C ₈ H ₁₆ O ₂	228	357	401	Insoluble
Titanium tetraisopropoxide (TTIP)	C ₁₂ H ₂₈ O ₄ Ti	232	N.A.	N.A.	React with water, hydrolysis
Lithium nitrate	LiNO ₃	600	N.A.	N.A.	52.2 g/100 mL (20 °C)
Tin(II) 2-ethylhexanoate	C ₁₆ H ₃₀ O ₄ Sn	decomposes	N.A.	N.A.	Degrades in water to form Sn(IV)
Ce (III) 2-ethylhexanoate	C ₂₄ H ₄₅ CeO ₆	decomposes	N.A.	N.A.	N.A.
Cr (III) 2-ethylhexanoate	C ₂₄ H ₄₅ CrO ₆	decomposes	N.A.	N.A.	N.A.
Zinc naphthenate	C ₂₂ H ₁₄ O ₄ Zn	decomposes	N.A.	N.A.	N.A.
Iron (II) naphthenate	C ₂₂ H ₁₄ FeO ₄	decomposes	N.A.	N.A.	Insoluble
Manganese naphthenate	C ₂₂ H ₁₄ MnO ₄	decomposes	N.A.	N.A.	N.A.
Iron (III) acetylacetonate	Fe(C ₅ H ₇ O ₂) ₃	decomposes	N.A.	N.A.	2 g/L

Critical point is obtained from Haynes WM, Lide DR. Handbook of chemistry and physics. CRC Press, Boca-Raton; 2007, Section 6, 49-64. Limit of superheat is took as 89% of the critical point, according to Blander, M., & Katz, J. L. (1975). Bubble nucleation in liquids. AIChE Journal, 21(5), 833-848.

A.2 BET and XRD measurements of FSP synthesized iron oxide particles

The specific surface areas of flame-made particles are achieved using BET measurements. For the precursor solvent system of FeNAP/p-Xylene, the specific surface areas of as-prepared particles decrease from 203.16, 140.13, to 98.73 m²/g with increasing of the precursor concentration from 0.1, 0.25, to 0.5 mol/L, respectively (**Figure A.1 a**). The specific surface areas of particles using 0.1 mol/L FeNT/EtOH and 0.1 mol/L FeNT/EtOH+EHA are 169.79 and 205.00 m²/g, respectively (**Figure A.1 b**). These flame-made iron oxide particles are analyzed using XRD measurements to identify phase compositions. The diffraction peaks of magnetite (Fe₃O₄), maghemite (γ -Fe₂O₃), and hematite (α -Fe₂O₃) are found in the XRD patterns of five FSP prepared iron oxide particles (**Figure A.2**). Thus, the particles are considered as a mixture of three crystallite structures. The sharp XRD parks of iron oxide particles prepared by FSP using 0.1 mol/L FeNT/EtOH indicate different crystalline sizes from small and large particles.

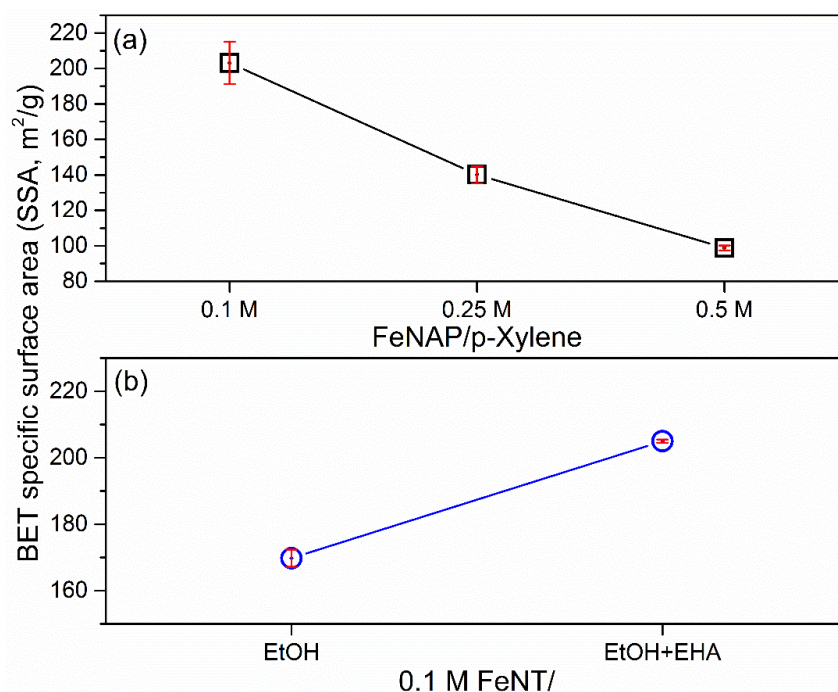


Figure A.1: BET specific surface area of FSP synthesized particles using (a) iron (II) naphthenate diluted with p-Xylene with a metal concentration of 0.1, 0.25, and 0.5 mol/L, and (b) 0.1 mol/L iron(III) nitrate nonahydrate diluted with ethanol and the mixture of ethanol and 2-ethyhexanoate

acid. The error bar (red, vertical) represents the standard deviation. The deviations of specific surface areas are 11.95, 4.88, and 1.35 m²/g for 0.1, 0.25, and 0.5 mol/L FeNAP/p-Xylene, respectively. The deviations of specific surface areas are 2.66, and 0.50 m²/g for 0.1 mol/L FeNT/EtOH and 0.1 mol/L FeNT/EtOH+EHA, respectively.

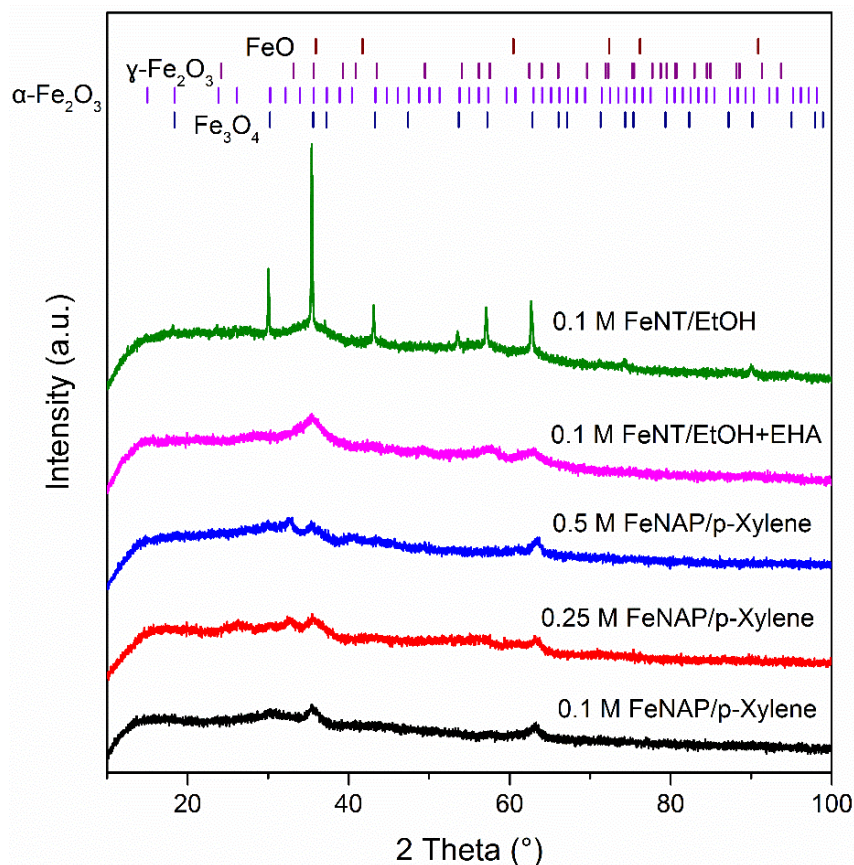


Figure A.2: XRD patterns of iron oxide particles prepared by FSP using iron (II) naphthenate diluted with p-Xylene with a metal concentration of 0.1, 0.25, and 0.5 mol/L, and (b) 0.1 mol/L iron(III) nitrate nonahydrate diluted with ethanol and the mixture of ethanol and 2-ethylhexanoate acid. The positions of the diffraction peaks of wustite (FeO, ICSD 82233), maghemite (γ -Fe₂O₃, ICSD 87119), hematite (α -Fe₂O₃, ICSD 291494), and magnetite (Fe₃O₄, ICSD 28664) are indicated for reference. The diffraction peaks of magnetite (Fe₃O₄), maghemite (γ -Fe₂O₃), and hematite (α -Fe₂O₃) could be detected in the XRD patterns of these five FSP prepared iron oxide particles.

A.3 Matlab scripts to pre-process hologram images

The main goal of these Matlab scripts is to remove background from raw hologram images and then to select area of interest as new images. The area of interest is square, and its center coincides with the center of the hologram signal. The side length of the selected region changes automatically in each frame in order to obtain the maximum. The captured image numbers are stored in "namesImgs" in Workspace. Pixel size in each captured image can be found in "windowSizes" in Workspace.

Following changes must be made before running the code.

- (1) Define the directory where all code files are located. Code "define_Directory.m", Line no.9.
- (2) Write the name of video file. Code "separateFrames.m", Line no.6.

Check the following things if desired results are not obtained.

- (1) Check the "Threshold_Vide.avi" in "videos" folder. If thresholding is not good then it might be the reason for getting incorrect results. Change threshold parameters. Alter the "canny" parameters in file "threshold.m", line no.18. Also alter the parameter in "refineThresholdResults.m", line no. 16.
- (2) Before running code, build up the following empty folders: "final_images", "raw_images", "removeBackground_images", "threshold_images" in the directory.

A.3.1 Main code: capture_window_around_droplet

```
% -----  
% Last Modified: 15-May-2019 (Wednesday)  
% This code loads a video and captures a picture around droplet.  
% This size of this captured window changes automatically based on largest possible size.  
% -----  
  
clear all;
```

```
% check if desired folders exist in the directory or not.
checkFolders();

% define working directory of code in this function.
define_Directory();

% this function separates the frames of original video and saves in a folder.
separateFrames(workingDir);

% this function initializes some arrays.
[tifFiles, name, number, cellCentres, cellArea, row, column] = initialization(workingDir);

% this function removes background from original images and saves in a folder.
removeBackground(workingDir, tifFiles, number);

% this function make a video from background removed images.
makeVideoRemoveBackground(workingDir);

% this function thresholds the original images and saves in a separate folder.
[cellCentres, cellArea] = threshold(workingDir, tifFiles, number);

% this function make a video from threshold images.
makeThresholdVideo(workingDir);

% this function refines the results of droplet centre and area found in "threshold" file.
[cellCentres, cellArea, row, column] = refineThresholdResults(cellCentres, cellArea, row, column);

% this function captures a pictures of defined size around droplet.
captureRegion(workingDir, tifFiles, number, row, column);

disp('All Done...!!!');
```

A.3.2 Function: checkFolders

```
% -----
% This function checks whether desired folders exit in directory or not.
% It will do nothing if folders already exist.
% It will create folders if they do not exist.
% -----

function checkFolders()

    disp('*** Checking if folders exist, if not then folders are being created...!!!');
    if ~exist('raw_images', 'dir')
        mkdir('raw_images')
    end
    if ~exist('removeBackground_images', 'dir')
        mkdir('removeBackground_images')
    end
    if ~exist('threshold_images', 'dir')
        mkdir('threshold_images')
```

```
end
if ~exist('final_images', 'dir')
    mkdir('final_images')
end
```

```
end
```

A.3.3 Function: define_Directory

```
% -----
% In this function, user must define the current working directory of code.
% -----

function define_Directory()

    % display on command window
    disp('*** Defining the working Directory...!!!');

    % define a directory where all the project files are located.
    workingDir = 'D:\Matlab Code\Holography\area_around_droplet_automatic_changing_window';

    % writing the working directory into workspace.
    assignin('base', 'workingDir', workingDir);

end
```

A.3.4 Function: separateFrames(workingDir)

```
% -----
% This function separates the frames of Original video and saves in the "raw_images" folder.
% -----

function separateFrames(workingDir)

    disp('*** Splitting the frames of Original Video...!!!');    % display on command window
    filename = 'H01_Z_30mm.avi';    % define the name of the video.
    fullpath = fullfile(workingDir, 'videos', filename);    % make full path of the video
    original_Video = VideoReader(fullpath);    % define the instance of the video
    loop = 1;    % each frame will be saved with increasing number
    while hasFrame(original_Video)    % continue while-loop until the last frame
of video
        img = readFrame(original_Video);    % read a frame
        filename = [sprintf('%s%04d', 'img', loop) '.tif'];    % make a name of frame to save
        fullpath = fullfile(workingDir, 'raw_images', filename);    % define full path to save the frame
        imwrite(img, fullpath);    % write the frame into direvtory
        loop = loop+1;    % increase loop to save next frame with different
name
```

```

end                                     % finish loop

end

```

A.3.5 Function: initialization

```

% -----
% This function initializes some arrays and reads all the .tif images splitted from video in last
% function.
% -----

function [tifFiles, name, number, cellCentres, cellArea, row, column] = initialization(workingDir)

    disp('*** Initializing Variables...!!!');           % display on command window
    filePattern = fullfile(workingDir,'raw_images', '*.tif'); % connect images folder with directory
to read original images
    tifFiles = dir(filePattern);                       % list all images in folder
    name = {tifFiles.name}';                          % copy the names of images in the folder
    number = numel(tifFiles);                         % find the number of images in folder

    cellCentres = cell(1,number);                    % initialize a cell to store centre of droplet
in each frame
    cellArea = cell(1,number);                       % initialize a cell to store area of droplet in
each frame
    row = zeros(1,number);                          % initialize an array to store the row value of
centre point
    column = zeros(1,number);                        % initialize an array to store the column
value of centre point

end

```

A.3.6 Function: removeBackground

```

% -----
% This function loads original images from "raw_images" folder. Removes background from them.
% And saves the new images into "removeBackground_images" folder.
% -----

function removeBackground(workingDir, tifFiles, number)

    disp('*** Removing Background from original images and saving...!!!'); % display on command
window
    img_name_size = tifFiles(1).name;                % copy the name of first image in the
folder
    img_fullpath_size = fullfile(workingDir, 'raw_images', img_name_size); % define complete path
of first image
    img_Read_size = imread(img_fullpath_size);      % read first image

```

```

[size_img_rows, size_img_cols] = size(img_Read_size);      % Find dimensions of first image
(all images must have same dimensions)

x=size_img_rows;                                         % Image pixels : vertical.
y=size_img_cols;                                         % Image pixels : horizontal.
background2 = zeros(x, y);                                % initialize a zero matrix of defined size

for i=1:1:number                                          % start a loop for total no. of frames
    img_name = tiffFiles(i).name;                          % copy the name of image
    img_fullpath = fullfile(workingDir, 'raw_images', img_name);% define complete path to load
original image
    img_Read = double(imread(img_fullpath));              % read original frame
    background1 = img_Read;                                % it is equal to background-1
    for j=1:1:x                                           % start a loop for all vertical pixels
        for k=1:1:y                                       % start a loop for all horizontal frames
            background2(j,k)=background1(j,k)+background2(j,k); % sum up the intensity
distributions of all the images
        end                                               % finish loop
    end                                                   % finish loop
end                                                       % finish loop

background2 = background2/number;                          % average the background intensity
distribution.
read3 = zeros(x, y);                                     % initialize a zero matrix of defined size

%               background2                               =               double(imread('D:\Matlab
Code\Holography\area_around_droplet_automatic_changing_window\raw_images\img0001.tif'));
for k=1:1:number                                          % start a loop for total number of frames
    img_name = tiffFiles(k).name;                          % copy the name of image
    img_fullpath = fullfile(workingDir, 'raw_images', img_name);% define complete path to load
original frame
    img_Read = double(imread(img_fullpath));              % read frame
    read1 = img_Read;                                     % it is equal to read1
    read2 = read1;                                       % assigning the value of read1 to read2
    for i=1:1:x                                           % start a loop for all vertical pixels
        for j=1:1:y                                       % start a loop for all horizontal pixels
            read3(i,j)=read2(i,j)-background2(i,j)-1;    % remove background
        end                                               % finish loop
    end                                                   % finish loop
    img_gray = mat2gray(read3);                            % convert image into Grayscale
    filename = [sprintf('%s%04d', 'img', k) '.tif'];      % define the name of image
    fullname = fullfile(workingDir, 'removeBackground_images', filename);% combine image
name with directory
    imwrite(img_gray, fullname);                           % write the image
end                                                       % finish loop

end

```

A.3.7 Function: makeVideoRemoveBackground

```

% -----
% This function loads images from "removeBackground_images" folder.
% Makes a video from those Background removed images.
% And saves into "videos" folder with the name "Remove_Background_Video.avi".
% -----

function makeVideoRemoveBackground(workingDir)

    disp('*** Making Video from background removed images...!!!');    % display on command
    window
    imageNames = dir(fullfile(workingDir,'removeBackground_images','*.tif'));% define full path to
    background removed image
    imageNames = {imageNames.name};    % define the names of images to
    be read
    outputVideo = VideoWriter(fullfile(workingDir,'videos','Remove_Background_Video.avi'));%
    video object to make a video from frames
    outputVideo.FrameRate = 30;    % define the frame rate of video
    open(outputVideo);    % open video object
    for ii = 1:length(imageNames)    % run the loop for total number of frames
        img = imread(fullfile(workingDir,'removeBackground_images',imageNames{ii}));% read the
        frame
        img = im2uint8(img);    % Change the data type of the image to
        unit8
        writeVideo(outputVideo,img)    % add frame to the video
    end    % finish loop
    close(outputVideo);    % close video object

end

```

A.3.8 Function: threshold

```

% -----
% This function loads original images from "raw_images" folder. Performs threshold operation.
% Saves threshold images into "threshold_images" folder.
% And then finds droplet centre point and area into threshold image.
% -----

function [cellCentres, cellArea] = threshold(workingDir, tiffFiles, number)

    disp('*** Thresholding original images...!');    % display on command window
    for k=11:number    % start loop from 11th frame
        img_name_current = tiffFiles(k).name;    % copy the name of image
        img_fullpath_current = fullfile(workingDir, 'raw_images', img_name_current);% define
        complete path of current frame
        img_Read = imread(img_fullpath_current);    % read current frame
    end

```

```

    img_name_background = tifFiles(k-10).name;           % copy the name of image for
background
    img_fullpath_background = fullfile(workingDir,      'raw_images',
img_name_background);%define complete path of background image
    img_Background = imread(img_fullpath_background);   % read the background image

    img_Sub = imsubtract(img_Background, img_Read);    % subtract current frame
from background image
    img_Edge = edge(img_Sub,'canny',[0.5 0.9],5);      % find edges in the subtracted
image
    img_Fill = imfill(img_Edge,'holes');              % fill the image after finding edges

    filename = [sprintf('%s%04d','img',k) '.tif'];    % make a name of image to save
threshold image
    fullname = fullfile(workingDir,'threshold_images',filename); % define complete path of
image
    imwrite(img_Fill, fullname);                      % write processed frame (filled image)

    s = regionprops(img_Fill,'centroid', 'Area');      % find regions in the image and get
their centres and area
    centres = cat(1,s.Centroid);                      % concatenate centres one after another
in a frame
    areas = cat(1,s.Area);                            % concatenate areas one after another in a
frame
%   fprintf('Frame No: %d\n', k);                    % display frame number on the command
window
%   disp('-----');% display on command window
%   disp('Centre Point : ');                        % display centre points on the command
window
%   disp(centres);                                  % display centre points on the command
window
%   disp('Area : ');                                % display areas of detected regions on
command window
%   disp(areas);                                    % display areas of detected regions on
command window
%   disp('No. of points detected : ');              % display number of detected regions on
command window
%   disp(size(centres,1));                          % display number of detected regions on
command window

    cellArea{k} = areas;                             % save areas in a cell
    cellCentres{k} = centres;                        % save centre points in a cell
end
% finish loop
end
end

```

A.3.9 Function: makeThresholdVideo

```

% -----
% This function loads images from "threshold_images" folder.
% Make a video from those threshold images.
% And then saves into "videos" folder with the name "Threshold_Video.avi".
% -----

function makeThresholdVideo(workingDir)

    disp('*** Making Video from threshold images...!!!');           % display on command window
    imageNames = dir(fullfile(workingDir,'threshold_images','*.tif')); % define full path to load
threshold image
    imageNames = {imageNames.name};                                % define the names of images
to be read
    outputVideo = VideoWriter(fullfile(workingDir,'videos','Threshold_Video.avi')); % object to make
a video from frames
    outputVideo.FrameRate = 30;                                   % define the frame rate of video
    open(outputVideo);                                           % open video object
    for ii = 1:length(imageNames)                                 % run the loop for total number of
frames
        img = imread(fullfile(workingDir,'threshold_images',imageNames{ii})); % read the frame
        img = im2uint8(img);                                     % Change the data type of the image to
unit8
        writeVideo(outputVideo,img)                               % add frame to the video
    end                                                           % finish loop
    close(outputVideo);                                          % close video object

end

```

A.3.10 Function: refineThresholdResults

```

% -----
% This function performs operation on "cellCentres" and "cellArea" cell arrays.
% "regionprops" function has been used in "threshold" file.
% which finds the connected region in threshold image and gives their centre points and areas.
% This function ignores the noise and detects the true droplets.
% finally it saves x and y values of droplet into "row" and "column" arrays.
% -----

function [cellCentres, cellArea, row, column] = refineThresholdResults(cellCentres, cellArea, row,
column)

    disp('*** Refining Threshold Results...!!!');                 % display on command window
    cellsLength = cellfun('length',cellArea);                    % find the length of each cell containing
Areas
    for j=1:length(cellsLength)                                   % start loop(a loop iteration for each
frame)

```

```

    if cellsLength(j) > 1                                % if there are more than one regions in an
image
    cellArea{j} = 0;                                    % make that cell element equal to zero
    end                                                % finish if-condition
    ar = cellArea{j}();                                  % get the value of area in a cell element
index
    if ar < 150                                          % if area is less than 150
    cellArea{j}=0;                                      % make that cell index equal to zero
    end                                                % finish if-condition
    if isempty(cellArea{1,j})                          % if a particular area cell array index is
empty
    cellArea{j}=0;                                      % make that equal to zero
    end                                                % finish if-condition
    if cellArea{j}() == 0                              % if a cell element containing area is zero
    cellCentres{j} = 0;                                % make corresponding element of centres
cell equal to zero
    end                                                % finish if-condition
    if cellCentres{j}() ~= 0                          % if cell centre index is not zero
    column(j) = round(cellCentres{j}(1));              % get the column pixel
    row(j) = round(cellCentres{j}(2));                % get the row pixel
    end                                                % finish if-condition
    end                                                % finish for-loop

    row = row';                                        % take transpose matrix containing row pixel
of centre point of droplet
    column = column';                                  % take transpose matrix containing column
pixel of centre point of droplet

end

```

A.3.11 Function: captureRegion

```

% -----
% Based on centre points refined previously, this function captures a picture around the droplet.
% Size of this captured image changes automatically based on largest possible size.
% This image is then saved in the "final_images" folder.
% -----

function captureRegion(workingDir, tifFiles, number, row, column)

    disp('*** Finding surrounding windows around droplet and storing in the folder...!!!');% display
on command window
    windows = zeros(number,2);                        % initialize to store image numbers
and sizes of captured windows in those
    img_name_size = tifFiles(1).name;                % copy the name of first image in
the folder
    img_fullpath_size = fullfile(workingDir, 'raw_images', img_name_size); % define complete path
of first image
    img_Read_size = imread(img_fullpath_size);       % read first image

```

```

[size_img_rows, size_img_cols] = size(img_Read_size);           % Find dimensions of first
image (all images must have same dimensions)
for i=1:1:number                                               % start running the loop from first till last
frame
    rw = row(i);                                               % get the row value of detected particle in
current frame
    cl = column(i);                                           % get the column value of detected particle
in current frame
    if rw~=0 && cl~=0                                           % if particle is present
        left_margin = abs(cl-1);                               % calculate distance of left border of image
from centre point
        right_margin = abs(cl-size_img_cols);                 % calculate distance of right border
of image from centre point
        top_margin = abs(rw-1);                               % calculate distance of top border of
image from centre point
        bottom_margin = abs(rw-size_img_rows);                % calculate distance of bottom
border of image from centre point
%         disp(left_margin);
%         disp(right_margin);
%         disp(top_margin);
%         disp(bottom_margin);
        window_size = min([left_margin, right_margin, top_margin, bottom_margin]);% find which
border is closest, this is the window size
        windows(i,1) = i;                                     % copy the image number
        windows(i,2) = window_size;                          % copy the window size in that image
%         fprintf("Window Size for %d frame is %d\n", i, window_size);
        baseFileName = tifFiles(i).name;                      % read the name of current frame of
video
        fullFileName = fullfile(workingDir, 'removeBackground_images', baseFileName);% define
complete path of current frame
        currentFrame = imread(fullFileName);                  % read current frame
        surroundingWindow = currentFrame(rw-window_size:rw+window_size, cl-
window_size:cl+window_size);% select a surrounding window around centre point
        filename = [sprintf('%s%04d', 'img', i) '.tif'];      % make a name of image to save
        fullname = fullfile(workingDir, 'final_images', filename); % define complete path of image
        imwrite(surroundingWindow, fullname, 'Compression', 'none', 'Resolution', [1270,1270]); %
save the image (surrounding window)
    end                                                         % finish if-condition
end                                                         % finish for-loop
assignin('base', 'windowsSizes', windows);                    % write no. of images and their
windows into Workspace
imgSizes = windows(:,2);                                       % copy the window sizes
maxVals = max(imgSizes);                                       % finding the largest window sizes
idxMax = find(imgSizes == maxVals);                             % finding the images(indices) which
have largest windows
namesImgs = cell(length(idxMax), 1);                            % make a cell to store names if
images
for i=1:1:length(idxMax)                                       % start the loop
    tmp = idxMax(i);                                           % copy the value if index
    a = sprintf('%s%0%d%s', 'img', tmp, '.tif');                % make a name with it
    namesImgs{i} = a;                                          % store this name in the cell

```

```
end % finish loop
assignin('base', 'namesImgs', namesImgs); % write into workspace
end
```

A.4 Blur percentage calculation

The blurriness values of out-of-focus images are calculated using the algorithm to measure the blur percentage between a reference image (original image) and a blurred image, *i.g.*, determining the blur's percentage based on edges' sharpness with respect to the reference image [156]. The sharpness of the edges is the best criteria to indicate the amount of the existing blur in the blurred image compared to the original image [157]. The corresponding Matlab script, named Image Blur Measurement, could be found in the MATLAB Central File Exchange [158].

The detailed description of the algorithm is described in the cited literature [156], and thus here only a brief introduction is shown. Assuming one reference image and one blurred image as shown in **Figure A.3**. Both images have the same pixel size of 5X7, and each pixel has an intensity value as marked in the left column in **Figure A.3**. Except for the boundary pixels, the other pixels (center pixel) have 8 neighbor pixels. The intensity variations between the center pixel and the neighbor pixels are given in the middle column in **Figure A.3** (Purple values). The largest value of the intensity variations is typed in the location of the center pixel (Red values). Using the same way, the maximum values of the intensity variations for the rest pixels can be calculated, and all these values are averaged and then used in the blur percentage equation.

$$\begin{aligned} \text{Blur precentage} &= \frac{\text{abs}(\text{Ref} - \text{Blu})}{\text{Ref}} \times 100\% \\ &= \frac{\text{abs}(8-1)}{8} \times 100\% = 87.5\% \end{aligned}$$

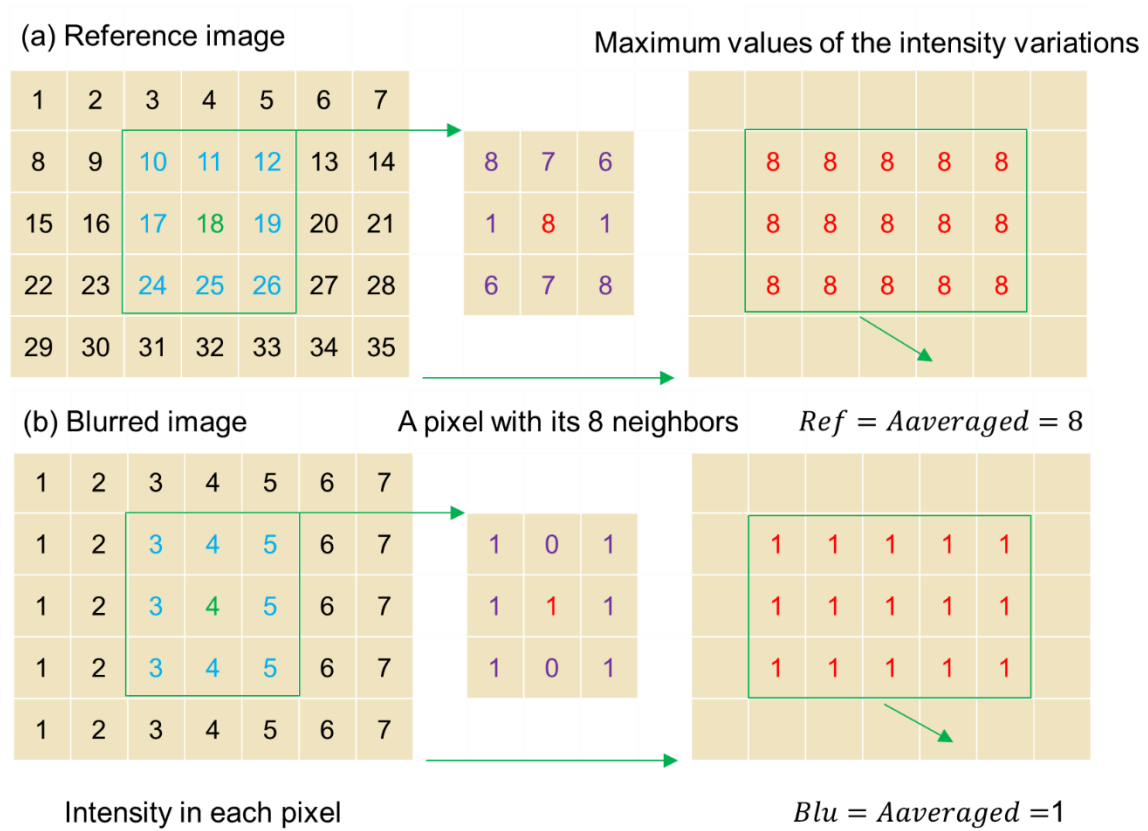


Figure A.3: Diagram of the algorithm to calculate blur percentage. The detailed description of the algorithm is described in the cited literature [156]

References

- [1] G. Ulrich, "Flame synthesis of fine particles," *Chemical & Engineering News* vol. 62, pp. 22-29, 1984.
- [2] K. Wegner, and S. E. Pratsinis, "Scale-up of nanoparticle synthesis in diffusion flame reactors," *Chemical Engineering Science*, vol. 58, no. 20, pp. 4581-4589, 2003.
- [3] S. Li, Y. Ren, P. Biswas, and S. D. Tse, "Flame aerosol synthesis of nanostructured materials and functional devices: Processing, modeling, and diagnostics," *Progress in Energy and Combustion Science*, vol. 55, pp. 1-59, 2016.
- [4] R. Strobel, and S. E. Pratsinis, "Flame aerosol synthesis of smart nanostructured materials," *Journal of Materials Chemistry*, vol. 17, no. 45, pp. 4743-4756, 2007.
- [5] W. Y. Teoh, R. Amal, and L. Mädler, "Flame spray pyrolysis: An enabling technology for nanoparticles design and fabrication," *Nanoscale*, vol. 2, no. 8, pp. 1324-47, Aug, 2010.
- [6] F. Meierhofer, H. Li, M. Gockeln, R. Kun, T. Grieb, A. Rosenauer, U. Fritsching, J. Kiefer, J. Birkenstock, L. Mädler, and S. Pokhrel, "Screening precursor–solvent combinations for $\text{Li}_4\text{Ti}_5\text{O}_{12}$ energy storage material using flame spray pyrolysis," *ACS Applied Materials & Interfaces*, vol. 9, no. 43, pp. 37760-37777, 2017.
- [7] W. J. Stark, L. Mädler, M. Maciejewski, S. E. Pratsinis, and A. Baiker, "Flame synthesis of nanocrystalline ceria–zirconia: effect of carrier liquid," *Chemical Communications*, no. 5, pp. 588-589, 2003.
- [8] R. Strobel, and S. E. Pratsinis, "Effect of solvent composition on oxide morphology during flame spray pyrolysis of metal nitrates," *Physical Chemistry Chemical Physics*, vol. 13, no. 20, pp. 9246-52, May 28, 2011.
- [9] C. Schulz, T. Dreier, M. Fikri, and H. Wiggers, "Gas-phase synthesis of functional nanomaterials: Challenges to kinetics, diagnostics, and process development," *Proceedings of the Combustion Institute*, vol. 37, no. 1, pp. 83-108, 2019.
- [10] S. Pokhrel, and L. Mädler, "Flame Made Particles for Sensors, Catalysis and Energy Storage Applications," *Energy & Fuels*, 2020.
- [11] L. Madler, H. K. Kammler, R. Mueller, and S. E. Pratsinis, "Controlled synthesis of nanostructured particles by flame spray pyrolysis," *Journal of Aerosol Science*, vol. 33, no. 2, pp. 369-389, Feb, 2002.
- [12] L. Mädler, W. J. Stark, and S. E. Pratsinis, "Flame-made Ceria Nanoparticles," *Journal of Materials Research*, vol. 17, no. 6, pp. 1356-1362, 2011.

- [13] P. Merkl, M.-S. Aschtgen, B. Henriques-Normark, and G. A. Sotiriou, "Biofilm interfacial acidity evaluation by pH-Responsive luminescent nanoparticle films," *Biosensors and Bioelectronics*, vol. 171, pp. 112732, 2020.
- [14] F. Meierhofer, L. Mädler, and U. Fritsching, "Nanoparticle evolution in flame spray pyrolysis—Process design via experimental and computational analysis," *AIChE Journal*, vol. 66, no. 2, pp. e16885, 2020.
- [15] H. K. Grossmann, T. Grieb, F. Meierhofer, M. J. Hodapp, D. Noriler, A. Grohn, H. F. Meier, U. Fritsching, K. Wegner, and L. Mädler, "Nanoscale mixing during double-flame spray synthesis of heterostructured nanoparticles," *Journal of Nanoparticle Research*, vol. 17, no. 4, pp. 174, Apr 8, 2015.
- [16] K. Wegner, B. Schimmoeller, B. Thiebaut, C. Fernandez, and T. N. Rao, "Pilot plants for industrial nanoparticle production by flame spray pyrolysis," *KONA Powder and Particle Journal*, vol. 29, pp. 251-265, 2011.
- [17] F. Schneider, S. Suleiman, J. Menser, E. Borukhovich, I. Wlokas, A. Kempf, H. Wiggers, and C. Schulz, "SpraySyn—A standardized burner configuration for nanoparticle synthesis in spray flames," *Review of Scientific Instruments*, vol. 90, no. 8, pp. 085108, 2019.
- [18] M. M. Prenting, M. I. B. Dzulfida, T. Dreier, and C. Schulz, "Characterization of tracers for two-color laser-induced fluorescence liquid-phase temperature imaging in sprays," *Experiments in Fluids*, vol. 61, no. 3, pp. 1-15, 2020.
- [19] J. Harra, S. Kujanpää, J. Haapanen, P. Juuti, J. M. Mäkelä, L. Hyvärinen, and M. Honkanen, "Aerosol analysis of residual and nanoparticle fractions from spray pyrolysis of poorly volatile precursors," *AIChE Journal*, vol. 63, no. 3, pp. 881-892, 2017.
- [20] K. Okuyama, and I. W. Lenggoro, "Preparation of nanoparticles via spray route," *Chemical Engineering Science*, vol. 58, no. 3-6, pp. 537-547, 2003.
- [21] R. Yihua, C. Jinzhi, and H. Pitsch, "Theoretical Single-Droplet Model for Particle Formation in Flame Spray Pyrolysis," *Energy & Fuels*, vol. 35, no. 2, pp. 1750-1759, 2021.
- [22] G. L. Messing, S. C. Zhang, and G. V. Jayanthi, "Ceramic powder synthesis by spray pyrolysis," *Journal of the American Ceramic Society*, vol. 76, no. 11, pp. 2707-2726, Nov, 1993.
- [23] T. Dreier, and C. Schulz, "Laser-based diagnostics in the gas-phase synthesis of inorganic nanoparticles," *Powder Technology*, vol. 287, pp. 226-238, 2016.

- [24] M. F. Stodt, J. Kiefer, and U. Fritsching, "Ethanol droplet formation, dynamics and combustion mode in the flame of the SpraySyn-nozzle," *Experiments in Fluids*, vol. 60, no. 8, pp. 125, 2019.
- [25] H. Schulz, L. Mädler, R. Strobel, R. Jossen, S. E. Pratsinis, and T. Johannessen, "Independent control of metal cluster and ceramic particle characteristics during one-step synthesis of Pt/TiO₂," *Journal of Materials Research*, vol. 20, no. 9, pp. 2568-2577, 2005.
- [26] F. J. Martins, J. Kirchmann, A. Kronenburg, and F. Beyrau, "Experimental investigation of axisymmetric, turbulent, annular jets discharged through the nozzle of the SPP1980 SpraySyn burner under isothermal and reacting conditions," *Experimental Thermal and Fluid Science*, vol. 114, pp. 110052, 2020.
- [27] A. J. Gröhn, S. E. Pratsinis, A. Sánchez-Ferrer, R. Mezzenga, and K. Wegner, "Scale-up of Nanoparticle Synthesis by Flame Spray Pyrolysis: The High-Temperature Particle Residence Time," *Industrial & Engineering Chemistry Research*, vol. 53, no. 26, pp. 10734-10742, 2014.
- [28] H. Li, C. Rosebrock, N. Riefler, T. Wriedt, and L. Mädler, "Experimental investigation on microexplosion of single isolated burning droplets containing titanium tetraisopropoxide for nanoparticle production," *Proceedings of the Combustion Institute*, vol. 36, no. 1, pp. 1011-1018, 2017.
- [29] H. Li, C. D. Rosebrock, T. Wriedt, and L. Mädler, "The effect of initial diameter on rainbow positions and temperature distributions of burning single-component n-Alkane droplets," *Journal of Quantitative Spectroscopy & Radiative Transfer*, vol. 195, pp. 164-175, 2017.
- [30] H. Li, C. D. Rosebrock, Y. Wu, T. Wriedt, and L. Mädler, "Single droplet combustion of precursor/solvent solutions for nanoparticle production: Optical diagnostics on single isolated burning droplets with micro-explosions," *Proceedings of the Combustion Institute*, vol. 37, no. 1, pp. 1203-1211, 2019.
- [31] C. D. Rosebrock, N. Riefler, T. Wriedt, L. Mädler, and D. T. Stephen, "Disruptive burning of precursor/solvent droplets in flame - spray synthesis of nanoparticles," *AIChE Journal*, vol. 59, no. 12, pp. 4553-4566, 2013.
- [32] C. D. Rosebrock, S. Shirinzadeh, M. Soeken, N. Riefler, T. Wriedt, R. Drechsler, and L. Mädler, "Time-resolved detection of diffusion limited temperature gradients inside single isolated burning droplets using Rainbow Refractometry," *Combustion and Flame*, vol. 168, pp. 255-269, 2016.

- [33] C. D. Rosebrock, T. Wriedt, L. Mädler, and K. Wegner, "The role of microexplosions in flame spray synthesis for homogeneous nanopowders from low - cost metal precursors," *AIChE Journal*, vol. 62, no. 2, pp. 381-391, 2016.
- [34] I. Skenderovic, G. Kotalczyk, and F. E. Kruis, "Dual population balance Monte Carlo simulation of particle synthesis by flame spray pyrolysis," *Processes*, vol. 6, no. 12, pp. 253, Dec, 2018.
- [35] D. Sharma, S. Stephen, and R. Natarajan, "Structure of burning n-hexane droplet by moiré deflectometry," *Combustion Science and Technology*, vol. 131, no. 1-6, pp. 305-321, 1998.
- [36] S. S. Hou, F. M. Rizal, T. H. Lin, T. Y. Yang, and H. P. Wan, "Microexplosion and ignition of droplets of fuel oil/bio-oil (derived from lauan wood) blends," *Fuel*, vol. 113, pp. 31-42, 2013.
- [37] H. Li, C. D. Rosebrock, N. Riefler, T. Wriedt, and L. Mädler, "Experimental investigations on the effects of water vapor and oxygen concentrations in the ambience on the burning constant, lifetime and residuals of single isolated xylene, isobutanol and ethanol droplets," *Experimental Thermal and Fluid Science*, pp. 109920, 2019.
- [38] H. Li, S. Pokhrel, M. Schowalter, A. Rosenauer, J. Kiefer, and L. Mädler, "The gas-phase formation of tin dioxide nanoparticles in single droplet combustion and flame spray pyrolysis," *Combustion and Flame*, vol. 215, pp. 389-400, 2020.
- [39] H. Li, N. Riefler, T. Wriedt, and L. Mädler, "Reference data set for three-dimensional measurements of double droplet combustion of p-xylene," *Proceedings of the Combustion Institute*, 2020.
- [40] W. Wu, Q. He, and C. Jiang, "Magnetic iron oxide nanoparticles: synthesis and surface functionalization strategies," *Nanoscale Research Letters*, vol. 3, no. 11, pp. 397-415, 2008.
- [41] A. Ali, M. Z. Hira Zafar, I. Ul Haq, A. R. Phull, J. S. Ali, and A. Hussain, "Synthesis, characterization, applications, and challenges of iron oxide nanoparticles," *Nanotechnology, Science and Applications*, vol. 9, pp. 49-67, 2016.
- [42] A. S. Teja, and P.-Y. Koh, "Synthesis, properties, and applications of magnetic iron oxide nanoparticles," *Progress in Crystal Growth and Characterization of Materials*, vol. 55, no. 1-2, pp. 22-45, 2009.
- [43] L. Machala, R. Zboril, and A. Gedanken, "Amorphous iron (III) oxide a review," *The Journal of Physical Chemistry B*, vol. 111, no. 16, pp. 4003-4018, 2007.
- [44] B. Sundman, "An assessment of the Fe-O system," *Journal of Phase Equilibria*, vol. 12, no. 2, pp. 127-140, 1991.

- [45] M. Sorvali, M. Nikka, P. Juuti, M. Honkanen, T. Salminen, L. Hyvärinen, and J. M. Mäkelä, "Controlling the phase of iron oxide nanoparticles fabricated from iron (III) nitrate by liquid flame spray," *International Journal of Ceramic Engineering & Science*, vol. 1, no. 4, pp. 194-205, 2019.
- [46] C. C. Berry, and A. S. Curtis, "Functionalisation of magnetic nanoparticles for applications in biomedicine," *Journal of physics D: Applied physics*, vol. 36, no. 13, pp. 198-206, 2003.
- [47] D. Li, W. Y. Teoh, C. Selomulya, R. C. Woodward, P. Munroe, and R. Amal, "Insight into microstructural and magnetic properties of flame-made γ -Fe₂O₃ nanoparticles," *Journal of Materials Chemistry*, vol. 17, no. 46, pp. 4876-4884, 2007.
- [48] D. Li, W. Y. Teoh, C. Selomulya, R. C. Woodward, R. Amal, and B. Rosche, "Flame-sprayed superparamagnetic bare and silica-coated maghemite nanoparticles: Synthesis, characterization, and protein adsorption desorption," *Chemistry of Materials*, vol. 18, no. 26, pp. 6403-6413, 2006.
- [49] R. Strobel, and S. E. Pratsinis, "Direct synthesis of maghemite, magnetite and wustite nanoparticles by flame spray pyrolysis," *Advanced Powder Technology*, vol. 20, no. 2, pp. 190-194, 2009.
- [50] Y. Li, Y. Hu, G. Huang, and C. Li, "Metallic iron nanoparticles: Flame synthesis, characterization and magnetic properties," *Particuology*, vol. 11, no. 4, pp. 460-467, 2013.
- [51] J. Harra, J. P. Nikkanen, M. Aromaa, H. Suhonen, M. Honkanen, T. Salminen, S. Heinonen, E. Levänen, and J. M. Mäkelä, "Gas phase synthesis of encapsulated iron oxide–titanium dioxide composite nanoparticles by spray pyrolysis," *Powder Technology*, vol. 243, pp. 46-52, 2013.
- [52] M. Tepluchin, D. K. Pham, M. Casapu, L. Mädler, S. Kureti, and J.-D. Grunwaldt, "Influence of single- and double-flame spray pyrolysis on the structure of MnOx/ γ -Al₂O₃ and FeOx/ γ -Al₂O₃ catalysts and their behaviour in CO removal under lean exhaust gas conditions," *Catalysis Science & Technology*, vol. 5, no. 1, pp. 455-464, 2015.
- [53] S. Rajput, L. P. Singh, C. U. Pittman, Jr., and D. Mohan, "Lead (Pb(2+)) and copper (Cu(2+)) remediation from water using superparamagnetic maghemite (γ -Fe₂O₃) nanoparticles synthesized by Flame Spray Pyrolysis (FSP)," *Journal of Colloid and Interface Science*, vol. 492, pp. 176-190, Apr 15, 2017.
- [54] T. Rudin, K. Wegner, and S. E. Pratsinis, "Uniform nanoparticles by flame-assisted spray pyrolysis (FASP) of low cost precursors," *Journal of Nanoparticle Research*, vol. 13, no. 7, pp. 2715-2725, 2011.

- [55] J. Wei, S. Li, Y. Ren, Y. Zhang, and S. D. Tse, "Investigating the role of solvent formulations in temperature-controlled liquid-fed aerosol flame synthesis of YAG-based nanoparticles," *Proceedings of the Combustion Institute*, vol. 37, no. 1, pp. 1193-1201, 2019.
- [56] S. Angel, J. Neises, M. Dreyer, K. F. Ortega, M. Behrens, Y. Wang, H. Arandiyán, C. Schulz, and H. Wiggers, "Spray - flame synthesis of La(Fe, Co)O₃ nano - perovskites from metal nitrates," *AIChE Journal*, 2019.
- [57] C. Abram, M. Mezhericher, F. Beyrau, H. A. Stone, and Y. Ju, "Flame synthesis of nanophosphors using sub-micron aerosols," *Proceedings of the Combustion Institute*, vol. 37, no. 1, pp. 1231-1239, 2019.
- [58] Z. Zhang, H. Tian, S. Li, and Q. Wang, "Synthesis of ultra-fine iron powder by combining the flame aerosol synthesis and postreduction," *Journal of Materials Research*, vol. 34, no. 23, pp. 3964-3974, 2019.
- [59] L. Carvajal, R. Buitrago-Sierra, A. Santamaría, S. Angel, H. Wiggers, and J. Gallego, "Effect of spray parameters in a spray flame reactor during Fe_xO_y nanoparticles synthesis," *Journal of Thermal Spray Technology*, vol. 29, no. 3, pp. 368-383, 2020.
- [60] S. Gordon, and B. J. McBride, "Computer program for calculation of complex chemical equilibrium compositions and applications. Part 1: Analysis," 1994.
- [61] D. R. Lide, *CRC handbook of chemistry and physics*, 84th ed., p.^pp. 107-122: CRC Press, 2004.
- [62] W. V. Steele, R. D. Chirico, S. E. Knipmeyer, and A. Nguyen, "Vapor pressure, heat capacity, and density along the saturation line, measurements for cyclohexanol, 2-cyclohexen-1-one, 1,2-dichloropropane, 1,4-di-tert-butylbenzene, (+/-)-2-ethylhexanoic acid, 2-(methylamino)ethanol, perfluoro-n-heptane, and sulfolane," *Journal of Chemical and Engineering Data*, vol. 42, no. 6, pp. 1021-1036, Nov-Dec, 1997.
- [63] H. Perry Robert, W. Green Don, and O. Maloney James, *Perry's Chemical Engineers' Handbook*, 7th ed., p.^pp. 89-90: Mc Graw-Hills New York, 1997.
- [64] G. L. Chiarello, I. Rossetti, L. Forni, P. Lopinto, and G. Migliavacca, "Solvent nature effect in preparation of perovskites by flame pyrolysis," *Applied Catalysis B: Environmental*, vol. 72, no. 3-4, pp. 227-232, 2007.
- [65] C. K. Law, and F. A. Williams, "Kinetics and convection in the combustion of alkane droplets," *Combustion and Flame*, vol. 19, no. 3, pp. 393-405, 1972.
- [66] A. Williams, "Combustion of droplets of liquid fuels: a review," *Combustion and Flame*, vol. 21, no. 1, pp. 1-31, 1973.

- [67] N. Kawahara, S. Hashimoto, and E. Tomita, "Plasma temperature of spark discharge in a spark-ignition engine using a time series of spectra measurements."
- [68] M. Mikami, and N. Kojima, "An experimental and modeling study on stochastic aspects of microexplosion of binary-fuel droplets," *Proceedings of the Combustion Institute*, vol. 29, no. 1, pp. 551-559, 2002.
- [69] C. K. Law, *Combustion Physics*, p.^pp. 595-622: Cambridge University Press, 2006.
- [70] S. Xue, W. Ousi-Benomar, and R. Lessard, " α -Fe₂O₃ thin films prepared by metalorganic deposition (MOD) from Fe(III) 2-ethylhexanoate," *Thin Solid Films*, vol. 250, no. 1-2, pp. 194-201, 1994.
- [71] M. F. Stodt, M. Gonchikzhapov, T. Kasper, U. Fritsching, and J. Kiefer, "Chemistry of iron nitrate-based precursor solutions for spray-flame synthesis," *Physical Chemistry Chemical Physics*, vol. 21, no. 44, pp. 24793-24801, 2019.
- [72] T. A. Scott Jr, "Refractive index of ethanol–water mixtures and density and refractive index of ethanol–water–ethyl ether mixtures," *The Journal of Physical Chemistry*, vol. 50, no. 5, pp. 406-412, 1946.
- [73] A. Kazakov, J. Conley, and F. L. Dryer, "Detailed modeling of an isolated, ethanol droplet combustion under microgravity conditions," *Combustion and Flame*, vol. 134, no. 4, pp. 301-314, 2003.
- [74] W. C. Hinds, *Aerosol technology: properties, behavior, and measurement of airborne particles*, p.^pp. p260-265: John Wiley & Sons, 1999.
- [75] L. Buss, F. Meierhofer, P. Bianchi Neto, H. França Meier, U. Fritsching, and D. Noriler, "Impact of co-flow on the spray flame behaviour applied to nanoparticle synthesis," *The Canadian Journal of Chemical Engineering*, vol. 97, no. 2, pp. 604-615, 2019.
- [76] D. Kilian, S. Engel, B. Borsdorf, Y. Gao, A. Kögler, S. Kobler, T. Seeger, S. Will, A. Leipertz, and W. Peukert, "Spatially resolved flame zone classification of a flame spray nanoparticle synthesis process by combining different optical techniques," *Journal of Aerosol Science*, vol. 69, pp. 82-97, 2014.
- [77] M. C. Heine, and S. E. Pratsinis, "Droplet and particle dynamics during flame spray synthesis of nanoparticles," *Industrial & Engineering Chemistry Research*, vol. 44, no. 16, pp. 6222-6232, 2005.
- [78] A. J. Gröhn, S. E. Pratsinis, and K. Wegner, "Fluid-particle dynamics during combustion spray aerosol synthesis of ZrO₂," *Chemical Engineering Journal*, vol. 191, pp. 491-502, 2012.

- [79] S. Aßmann, B. Münsterjohann, F. J. Huber, and S. Will, "Droplet sizing in spray flame synthesis using wideangle light scattering (WALS)," *Applied Physics B*, vol. 126, pp. 92, 2020.
- [80] W. A. Sirignano, "Fuel droplet vaporization and spray combustion theory," *Progress in Energy and Combustion Science*, vol. 9, no. 4, pp. 291-322, 1983.
- [81] H. Chiu, H. Kim, and E. Croke, "Internal group combustion of liquid droplets." pp. 971-980.
- [82] H. H. Chiu, and T. M. Liu, "Group combustion of liquid droplets," *Combustion Science and Technology*, vol. 17, no. 3-4, pp. 127-142, 1977.
- [83] W. A. Sirignano, "Advances in droplet array combustion theory and modeling," *Progress in Energy and Combustion Science*, vol. 42, pp. 54-86, 2014.
- [84] G. Castanet, L. Perrin, O. Caballina, and F. Lemoine, "Evaporation of closely-spaced interacting droplets arranged in a single row," *International Journal of Heat and Mass Transfer*, vol. 93, pp. 788-802, 2016.
- [85] C. K. Chen, and T. H. Lin, "Streamwise interaction of burning drops," *Combustion and Flame*, vol. 159, no. 5, pp. 1971-1979, 2012.
- [86] K. Miyasaka, and C. K. Law, "Combustion of strongly-interacting linear droplet arrays." pp. 283-292.
- [87] S. Kato, H. Mizuno, H. Kobayashi, and T. Niioka, "Experiments on flame spread of a fuel droplet array in a high-pressure ambience," *JSME International Journal Series B Fluids and Thermal Engineering*, vol. 41, no. 2, pp. 322-330, 1998.
- [88] B. D. Shaw, H. A. Dwyer, and J. B. Wei, "Studies on combustion of single and double streams of methanol and methanol/dodecanol droplets," *Combustion Science and Technology*, vol. 174, no. 3, pp. 29-50, 2002.
- [89] Y. Yoshida, K. Iwai, K. Nagata, T. Seo, M. Mikami, O. Moriue, T. Sakashita, M. Kikuchi, T. Suzuki, and M. Nokura, "Flame-spread limit from interactive burning droplets in microgravity," *Proceedings of the Combustion Institute*, vol. 37, no. 3, pp. 3409-3416, 2019.
- [90] J. Wang, X. Huang, X. Qiao, D. Ju, and C. Sun, "Experimental study on evaporation characteristics of single and multiple fuel droplets," *Journal of the Energy Institute*, 2020.
- [91] G. Xiong, R. Gandhi, X. Zhong, L. Mädler, and S. D. Tse, "Binary collision of a burning droplet and a non-burning droplet of xylene: Outcome regimes and flame dynamics," *Proceedings of the Combustion Institute*, vol. 37, no. 3, pp. 3345-3352, 2019.
- [92] N. Riefler, T. Wriedt, and U. Fritsching, "Impedance characterization of a coupled piezo-tube-fluid system for micro droplet generation," *Journal of Fluids and Structures*, vol. 88, pp. 185-197, 2019.

- [93] N. Riefler, T. Wriedt, and U. Fritsching, "Flexible Piezoelectric Drop-On-Demand Droplet Generation," in *Ilass Europe. 28th European Conference on Liquid Atomization and Spray Systems*, 2017, pp. 621-627.
- [94] N. Riefler, and T. Wriedt, "Generation of monodisperse micron - sized droplets using free adjustable signals," *Particle & Particle Systems Characterization*, vol. 25, no. 2, pp. 176-182, 2008.
- [95] H. Ulmke, T. Wriedt, and K. Bauckhage, "Piezoelectric droplet generator for the calibration of particle sizing instruments," *Chemical Engineering & Technology*, vol. 24, no. 3, pp. 265-268, 2001.
- [96] C. Tien, and S. Lee, "Flame radiation," *Progress in Energy and Combustion Science*, vol. 8, no. 1, pp. 41-59, 1982.
- [97] H. H. T. Kadota, "Soot concentration measurement in a fuel droplet flame via laser light scattering," *Combustion and Flame*, vol. 55, pp. 195-201, 1984.
- [98] M. Frenklach, "Reaction mechanism of soot formation in flames," *Physical Chemistry Chemical Physics*, vol. 4, no. 11, pp. 2028-2037, 2002.
- [99] K. Sivasankaran, K. Seetharamu, and R. Natarajan, "Numerical investigation of the interference effects between two burning fuel spheres," *International Journal of Heat and Mass Transfer*, vol. 39, no. 18, pp. 3949-3957, 1996.
- [100] C. P. Cho, H. Y. Kim, and S. S. Yoon, "Interaction of the burning spherical droplets in oxygen-enriched turbulent environment," *Combustion and Flame*, vol. 156, no. 1, pp. 14-24, 2009.
- [101] A. Umemura, "A theoretical study on the unsteady, interactive combustion of a linear fuel droplet stream," in *Symposium (International) on Combustion*, 1991, pp. 1445-1453.
- [102] J. Sangiovanni, and D. Liscinsky, "Soot formation characteristics of well-defined spray flames," in *Symposium (International) on Combustion*, 1985, pp. 1063-1073.
- [103] J. J. Sangiovanni, and M. Labowsky, "Burning Times of Linear Fuel Droplet Arrays - a Comparison of Experiment and Theory," *Combustion and Flame*, vol. 47, no. 1, pp. 15-30, 1982.
- [104] K. C. Chang, and J. S. Shieh, "Theoretical Investigation of Transient Droplet Combustion by Considering Flame Radiation," *International Journal of Heat and Mass Transfer*, vol. 38, no. 14, pp. 2611-2621, Sep, 1995.
- [105] A. Randolph, and C. K. Law, "Influence of physical mechanisms on soot formation and destruction in droplet burning," *Combustion and Flame*, vol. 64, no. 3, pp. 267-284, 1986.

- [106] T.-C. Poon, and J.-P. Liu, *Introduction to modern digital holography: with MATLAB*: Cambridge University Press, 2014.
- [107] M. Schürmann, "Digital in-line holographic microscopy with various wavelengths and point sources applied to static and fluidic specimens," Doctoral dissertation, Doctoral dissertation, Ruperto-Carola University of Heidelberg, 2007.
- [108] A. Berdeu, O. Flasseur, L. Mees, L. Denis, F. Momey, T. Olivier, N. Grosjean, and C. Fournier, "Reconstruction of in-line holograms: combining model-based and regularized inversion," *Optics Express*, vol. 27, no. 10, pp. 14951-14968, May 13, 2019.
- [109] D. Gabor, "A new microscopic principle," Nature Publishing Group, 1948.
- [110] D. Gabor, "Holography, 1948-1971," *Science*, vol. 177, no. 4046, pp. 299-313, 1972.
- [111] J. Garcia-Sucerquia, W. Xu, S. K. Jericho, P. Klages, M. H. Jericho, and H. J. Kreuzer, "Digital in-line holographic microscopy," *Applied Optics*, vol. 45, no. 5, pp. 836-850, 2006.
- [112] V. Palero, M. P. Arroyo, and J. Soria, "Digital holography for micro-droplet diagnostics," *Experiments in Fluids*, vol. 43, no. 2-3, pp. 185-195, 2007.
- [113] U. Schnars, and W. P. Jüptner, "Digital recording and numerical reconstruction of holograms," *Measurement Science and Technology*, vol. 13, no. 9, pp. R85, 2002.
- [114] U. Schnars, and W. Jüptner, "Direct recording of holograms by a CCD target and numerical reconstruction," *Applied Optics*, vol. 33, no. 2, pp. 179-181, 1994.
- [115] C. Tropea, "Optical Particle Characterization in Flows," *Annual Review of Fluid Mechanics*, vol. 43, no. 1, pp. 399-426, 2011.
- [116] J. Katz, and J. Sheng, "Applications of holography in fluid mechanics and particle dynamics," *Annual Review of Fluid Mechanics*, vol. 42, pp. 531-555, 2010.
- [117] W. Xu, M. Jericho, I. Meinertzhagen, and H. Kreuzer, "Digital in-line holography for biological applications," *Proceedings of the National Academy of Sciences*, vol. 98, no. 20, pp. 11301-11305, 2001.
- [118] J. Webster, R. Weight, and E. Archenhold, "Holographic size analysis of burning sprays," *Combustion and Flame*, vol. 27, no. 3, 1976.
- [119] D. R. Guildenbecher, M. A. Cooper, W. Gill, H. L. Stauffacher, M. S. Oliver, and T. W. Grasser, "Quantitative, three-dimensional imaging of aluminum drop combustion in solid propellant plumes via digital in-line holography," *Optics Letters*, vol. 39, no. 17, pp. 5126-9, Sep 1, 2014.
- [120] Y. Chen, D. R. Guildenbecher, K. N. G. Hoffmeister, M. A. Cooper, H. L. Stauffacher, M. S. Oliver, and E. B. Washburn, "Study of aluminum particle combustion in solid propellant

- plumes using digital in-line holography and imaging pyrometry," *Combustion and Flame*, vol. 182, pp. 225-237, 2017.
- [121] X. Wu, L. Yao, Y. Wu, X. Lin, L. Chen, J. Chen, X. Gao, and K. Cen, "In-Situ Characterization of Coal Particle Combustion via Long Working Distance Digital In-Line Holography," *Energy & Fuels*, vol. 32, no. 8, pp. 8277-8286, 2018.
- [122] L. Yao, C. Wu, Y. Wu, L. Chen, J. Chen, X. Wu, and K. Cen, "Investigating particle and volatile evolution during pulverized coal combustion using high-speed digital in-line holography," *Proceedings of the Combustion Institute*, vol. 37, no. 3, pp. 2911-2918, 2019.
- [123] S. R. Turns, *Introduction to combustion*: McGraw-Hill Companies, 1996.
- [124] I. Glassman, R. A. Yetter, and N. G. Glumac, *Combustion*: Academic press, 2014.
- [125] U. Schnars, C. Falldorf, J. Watson, and W. Jüptner, *Digital Holography and Wavefront Sensing*: Springer, 2016.
- [126] H. Kirchauer, "Photolithography Simulation," Institute for Microelectronics, TU Vienna, 1998.
- [127] Z. K., L. D., C. K., Z. K., and L. D., "Scalar Diffraction Theory," *Electromagnetic Theory for Microwaves and Optoelectronics*, pp. 621-672, Berlin, Heidelberg: Springer Berlin Heidelberg, 2008.
- [128] M. K. Kim, "Principles and techniques of digital holographic microscopy," *SPIE reviews*, vol. 1, no. 1, pp. 018005, 2010.
- [129] T. Kozacki, and K. Falaggis, "Angular spectrum-based wave-propagation method with compact space bandwidth for large propagation distances," *Optics Letters*, vol. 40, no. 14, pp. 3420-3423, 2015.
- [130] W. Zhang, H. Zhang, and G. Jin, "Band-extended angular spectrum method for accurate diffraction calculation in a wide propagation range," *Optics Letters*, vol. 45, no. 6, pp. 1543-1546, 2020.
- [131] J. Ratcliffe, "Some aspects of diffraction theory and their application to the ionosphere," *Reports on Progress in Physics*, vol. 19, no. 1, pp. 188, 1956.
- [132] T. Latychevskaia, and H. W. Fink, "Practical algorithms for simulation and reconstruction of digital in-line holograms," *Applied Optics*, vol. 54, no. 9, pp. 2424-34, Mar 20, 2015.
- [133] Y.-S. Choi, K.-W. Seo, M.-H. Sohn, and S.-J. Lee, "Advances in digital holographic micro-PTV for analyzing microscale flows," *Optics and Lasers in Engineering*, vol. 50, no. 1, pp. 39-45, 2012.
- [134] M. K. Kim, L. Yu, and C. J. Mann, "Interference techniques in digital holography," *Journal of Optics A: Pure and Applied Optics*, vol. 8, no. 7, pp. S518, 2006.

- [135] L. Yu, and M. K. Kim, "Wavelength-scanning digital interference holography for tomographic three-dimensional imaging by use of the angular spectrum method," *Optics Letters*, vol. 30, no. 16, pp. 2092-2094, 2005.
- [136] J. Sheng, E. Malkiel, and J. Katz, "Digital holographic microscope for measuring three-dimensional particle distributions and motions," *Applied Optics*, vol. 45, no. 16, pp. 3893-901, Jun 1, 2006.
- [137] Y. Wu, X. Wu, Z. Wang, L. Chen, and K. Cen, "Coal powder measurement by digital holography with expanded measurement area," *Applied Optics*, vol. 50, no. 34, pp. H22-9, Dec 1, 2011.
- [138] S. L. Pu, D. Allano, B. Patte-Rouland, M. Malek, D. Lebrun, and K. F. Cen, "Particle field characterization by digital in-line holography: 3D location and sizing," *Experiments in Fluids*, vol. 39, no. 1, pp. 1-9, Jul, 2005.
- [139] G. A. Tyler, and B. J. Thompson, "Fraunhofer Holography Applied to Particle Size Analysis a Reassessment," *Optica Acta: International Journal of Optics*, vol. 23, no. 9, pp. 685-700, 1976.
- [140] Y. Wu, X. Wu, Z. Wang, L. Chen, and K. Cen, "Coal powder measurement by digital holography with expanded measurement area," *Applied optics*, vol. 50, no. 34, pp. H22-H29, 2011.
- [141] J. Canny, "A computational approach to edge detection," *IEEE Transactions on pattern analysis and machine intelligence*, no. 6, pp. 679-698, 1986.
- [142] R. Maini, and H. Aggarwal, "Study and comparison of various image edge detection techniques," *International journal of image processing (IJIP)*, vol. 3, no. 1, pp. 1-11, 2009.
- [143] C. Wang, X. Liu, and C. K. Law, "Combustion and microexplosion of freely falling multicomponent droplets," *Combustion and Flame*, vol. 56, no. 2, pp. 175-197, 1984.
- [144] L. Méès, N. Grosjean, D. Chareyron, J. L. Marié, M. Seifi, and C. Fournier, "Evaporating droplet hologram simulation for digital in-line holography setup with divergent beam," *J Opt Soc Am A Opt Image Sci Vis*, vol. 30, no. 10, pp. 2021-8, Oct 1, 2013.
- [145] J.-L. Marié, N. Grosjean, L. Méès, M. Seifi, C. Fournier, B. Barbier, and M. Lance, "Lagrangian measurements of the fast evaporation of falling diethyl ether droplets using in-line digital holography and a high-speed camera," *Experiments in fluids*, vol. 55, no. 4, pp. 1708, 2014.
- [146] J. L. Marié, T. Tronchin, N. Grosjean, L. Méès, O. C. Öztürk, C. Fournier, B. Barbier, and M. Lance, "Digital holographic measurement of the Lagrangian evaporation rate of

- droplets dispersing in a homogeneous isotropic turbulence,” *Experiments in Fluids*, vol. 58, no. 2, 2017.
- [147] W. Yang, “Improved recursive algorithm for light scattering by a multilayered sphere,” *Applied Optics*, vol. 42, no. 9, pp. 1710-1720, 2003.
- [148] A. L. Aden, and M. Kerker, “Scattering of Electromagnetic Waves from Two Concentric Spheres,” *Journal of Applied Physics*, vol. 22, no. 10, pp. 1242-1246, 1951.
- [149] J. R. Wait, “Electromagnetic scattering from a radially inhomogeneous sphere,” *Applied Scientific Research, Section B*, vol. 10, no. 5-6, pp. 441-450, 1962.
- [150] R. Bhandari, “Scattering coefficients for a multilayered sphere: analytic expressions and algorithms,” *Applied Optics*, vol. 24, no. 13, pp. 1960, Jul 1, 1985.
- [151] Z. S. Wu, and Y. P. Wang, “Electromagnetic scattering for multilayered sphere: Recursive algorithms,” *Radio Science*, vol. 26, no. 6, pp. 1393-1401, 1991.
- [152] Z. S. Wu, L. X. Guo, K. F. Ren, G. Gouesbet, and G. Gréhan, “Improved algorithm for electromagnetic scattering of plane waves and shaped beams by multilayered spheres,” *Applied Optics*, vol. 36, no. 21, pp. 5188-5198, 1997.
- [153] L. Kai, and P. Massoli, “Scattering of electromagnetic-plane waves by radially inhomogeneous spheres: a finely stratified sphere model,” *Applied Optics*, vol. 33, no. 3, pp. 501-11, Jan 20, 1994.
- [154] R. Li, X. Han, L. Shi, K. F. Ren, and H. Jiang, “Debye series for Gaussian beam scattering by a multilayered sphere,” *Applied Optics*, vol. 46, no. 21, pp. 4804-12, Jul 20, 2007.
- [155] R. Li, X. Han, H. Jiang, and K. F. Ren, “Debye series for light scattering by a multilayered sphere,” *Applied Optics*, vol. 45, no. 6, pp. 1260-70, Feb 20, 2006.
- [156] M. Elsayed, F. Sammani, A. Hamdi, A. Albaser, and H. Babalghoom, “A new method for full reference image blur measure,” *International Journal of Simulation: Systems, Science Technology*, vol. 19, pp. 4, 2018.
- [157] R. Ferzli, and L. J. Karam, “A no-reference objective image sharpness metric based on the notion of just noticeable blur (JNB),” *IEEE transactions on image processing*, vol. 18, no. 4, pp. 717-728, 2009.
- [158] F. Sammani. "Image Blur Measurement," MATLAB Central File Exchange, 2021; <https://de.mathworks.com/matlabcentral/fileexchange/68350-image-blur-measurement>.

List of Publications by Haipeng Li

Peer-reviewed journal papers

[1] H. Li, C. Erinmwingbovo, J. Birkenstock, T. Obumneme, F. Kamosa, M. Schowalter, A. Rosenauer, F. LaMantia L. Mädler, S. Pokhrel. Double Flame Fabricated High-Performance AlPO₄/LiMn₂O₄ Nanoparticles for Li-Ion Battery. ACS Applied Energy Materials. 2021, 4, 4428-4443. DOI: <https://doi.org/10.1021/acsaem.1c00024>.

[2] H. Li, N. Riefler, T. Wriedt, L. Mädler. Reference data set for three-dimensional measurements of double droplet combustion of p-xylene. Proceedings of the Combustion Institute. 2020. DOI: <https://doi.org/10.1016/j.proci.2020.06.297>.

[3] H. Li, S. Pokhrel, M. Schowalter, A. Rosenauer, J. Kiefer, L. Mädler. The gas-phase formation of tin dioxide nanoparticles in single droplet combustion and flame spray pyrolysis. Combustion and Flame. 2020, 215, 389-400. DOI: <https://doi.org/10.1016/j.combustflame.2020.02.004>.

[4] C. Liu, S. Pokhrel, C. Tessarek, H. Li, M. Schowalter, A. Rosenauer, M. Eickhoff, S. Li, L. Mädler. Rare earth-doped Y₄Al₂O₉ nanoparticles for stable light-converting phosphors. ACS Applied Nano Materials. 2020, 3, 699-710. DOI: <https://doi.org/10.1021/acsanm.9b02231>.

[5] H. Li, C.D. Rosebrock, N. Riefler, T. Wriedt, L. Mädler. Experimental investigations on the effects of water vapor and oxygen concentrations in the ambience on the burning constant, lifetime and residuals of single isolated xylene, isobutanol and ethanol droplets. Experimental Thermal and Fluid Science. 2019, 109, 1-9.

DOI: <https://doi.org/10.1016/j.expthermflusci.2019.109920>.

[6] Y. Wu, H. Li, X. Wu, G. Grehan, L. Mädler, C. Crua, Change of evaporation rate of single monocomponent droplet with temperature using time-resolved phase rainbow refractometry. Proceedings of the Combustion Institute. 2019, 37, 3211-3218.

DOI: <https://doi.org/10.1016/j.proci.2018.09.026>.

[7] H. Li, C.D. Rosebrock, Y. Wu, T. Wriedt, L. Mädler. Single droplet combustion of precursor/solvent solutions for nanoparticle production: Optical diagnostics on single isolated burning droplets with microexplosions. Proceedings of the Combustion Institute. 2019, 37, 1203-1211. DOI: <https://doi.org/10.1016/j.proci.2018.06.133>.

[8] Y. Wu, C. Crua, H. Li, S. Saengkaew, L. Mädler, X. Wu, G. Gréhan. Simultaneous measurement of monocomponent droplet temperature/refractive index, size and evaporation rate with phase rainbow refractometry. Journal of Quantitative Spectroscopy and Radiative Transfer. 2018, 214, 146-157. DOI: <https://doi.org/10.1016/j.jqsrt.2018.04.034>.

[9] Y. Wu, H. Li, M. Brunel, J. Chen, G. Gréhan, L. Mädler. Phase interferometric particle imaging for simultaneous measurements of evaporating micron-sized droplet and nanoscale size changes. Applied Physics Letters. 2017, 111, 4: 041905. DOI: <https://doi.org/10.1063/1.4996363>.

[10] F. Meierhofer, H. Li, M. Gockeln, R. Kun, T. Grieb, A. Rosenauer, U. Fritsching, J. Kiefer, L. Mädler, S. Pokhrel. Screening Precursor-Solvent Combinations for $\text{Li}_4\text{Ti}_5\text{O}_{12}$ Energy Storage Material Using Flame Spray Pyrolysis. ACS Applied Materials & Interfaces. 2017, 9, 43: 37760-37777. DOI: <https://doi.org/10.1021/acsami.7b11435>

[11] H. Li, C.D. Rosebrock, T. Wriedt, L. Mädler. The effect of initial diameter on rainbow positions and temperature distributions of burning single-component n-Alkane droplets. Journal of Quantitative Spectroscopy and Radiative Transfer. 2017, 195: 164-175.

DOI: <https://doi.org/10.1016/j.jqsrt.2017.01.004>.

[12] H. Li, C.D. Rosebrock, N. Riefler, T. Wriedt, L. Mädler. Experimental investigation on microexplosion of single isolated burning droplets containing titanium tetraisopropoxide for nanoparticle production. Proceedings of the Combustion Institute. 2017, 36, 1: 1011-1018.

DOI: <https://doi.org/10.1016/j.proci.2016.09.017>.

International conferences attended:

[1] H. Li, Y. Wu, N. Riefler, T. Wriedt, X. Wu, L. Mädler, Preliminary investigation on single isolated burning droplet using digital in-line holography. The 18th Electromagnetic and Light Scattering Conference (10-14 June 2019, HangZhou, China) (Oral presentation).

[2] H. Li, L. Mädler, Nanoparticle synthesis in spray flames: Single droplet combustion of the flame spray pyrolysis precursor-solvent solutions. Photon Tools for Physical Chemistry 2019. (8-11 January 2019, Beatenberg, Switzerland) (Oral presentation).

[3] H. Li, S. Pokhrel, L. Mädler. The comparison of Tin dioxide nanoparticles synthesized from single droplet combustion and from flame spray pyrolysis. Gas-Phase Synthesis of Functional Nanomaterials: Fundamental Understanding, Modeling and Simulation, Scale-up and Application. (25–26 September 2018, Duisburg, Germany) (Poster).

[4] Y. Wu, H. Li, X. Wu, G. Grehan, L. Mädler, C. Crua. Single droplet combustion of precursor/solvent solutions for nanoparticle production: Optical diagnostics on single isolated burning droplets with microexplosions. 37th International Symposium on Combustion. (29 July-3 August 2018, Dublin, Ireland) (Oral presentation).

[5] H. Li, C.D. Rosebrock, Y. Wu, T. Wriedt, L. Mädler, Single droplet combustion of precursor/solvent solutions for nanoparticle production: Optical diagnostics on single isolated burning droplets with microexplosions. 37th International Symposium on Combustion. (29 July-3 August 2018, Dublin, Ireland) (Oral presentation).

[6] H. Li, C.D. Rosebrock, T. Wriedt, L. Mädler. Experimental investigations on single burning droplets with micro-explosions using shadowgraphy, interferometric particle imaging, and

standard rainbow refractometry. Sixteenth Conference on Electromagnetic & Light Scattering (19-25 March 2017, Maryland, USA) (Oral presentation).

[7] H. Li, C.D. Rosebrock, T. Wriedt, L. Mädler. New experimental findings of single burning droplets with micro-explosions by using standard rainbow refractometry. Bremen workshop on light scattering 2017 (20-21 February 2017, Bremen, Germany) (Oral presentation).

[8] H. Li, C.D. Rosebrock, T. Wriedt, L. Mädler. Assessing interior temperatures of burning nonane droplets of different sizes by rainbow refractometry. Laser-light and interactions with particles (LIP2016, 22-26 April 2016, Xi'an, China) (Oral presentation).

Co-supervised student work

[1] Daniel Phleps, Experimental investigations of double-droplet combustion (Experimentelle Untersuchgen zur gekoppelten Verbrennung von Tropfen). University of Bremen, 2019 March. (Bachelor thesis).

In the dissertation, the results from the supervision of the following students' works are included:

[2] MSc. Muhammad Shoaib Sikander, Counting nanoparticle size in TEM images and Programming for imaging processing. From 01.06.2018 to 30.06.2020 Mr. Sikander worked as a student assistant in Leibniz Institute for Materials Engineering IWT, and Faculty of Production Engineering at University of Bremen.

Statement by the doctoral candidate

Thesis

“Flame spray pyrolysis for synthesizing functional nanoparticles: Fundamental investigations on single and double droplet combustion”

From Haipeng Li

Hereby, I declare on oath that I completed this work on my own and that information which has been directly or indirectly taken from other sources has been noted as such. Neither this, nor a similar work, has been published or presented to an examination committee.

I also declare:

- the work was carried out without any unauthorized third-party assistance,
- no other sources or aids than the ones specified have been used,
- those works/text passages which have been included word by word or by content accordingly from other sources have been indicated,
- the electronic version of the doctoral thesis enclosed for examination purposes is identical to the submitted printed version.

Signature: _____

Date: _____

